Università degli Studi di Napoli *Federico II*

DOTTORATO di RICERCA in FISICA

Ciclo XXXVIII

Coordinatore: prof. Vincenzo Canale

Planetary Boundary Layer Height (PBLH) retrieval and analysis over two ACTRIS Stations by Active Remote Sensing Techniques

Settore Scientifico Disciplinare PHYS-06/A

Dottorando

Zeeshan Ali

Tutor

Prof. Salvatore Amoruso

Dott. Alessia Sannino

Anni 2023/2026

Acknowledgment

My PhD grant was funded in the framework of the ITINERIS project, the Italian Integrated Environmental Research Infrastructures System, funded by the EU - Next Generation EU PNRR- Mission 4 "Education and Research" - Component 2: "From research to business" - Investment 3.1: "Fund for the realization of an integrated system of research and innovation infrastructures".

I would also like to express my deepest gratitude to my supervisors, **Prof. Salvatore Amoruso**, **Dr. Alessia Sannino, and Dr. Antonella Boselli,** for their invaluable support, continuous encouragement, and insightful guidance throughout the course of my doctoral research. Their expertise, patience, and dedication have been a constant source of inspiration, and their constructive advice has greatly enriched both my scientific knowledge and personal growth. I am equally grateful to **Prof. Vincenzo Canale**, the coordinator of the PhD program, for providing me with the opportunity to pursue my research at the **Dipartimento Di Fisica "Ettore Pancini"**, **Università degli Studi di Napoli Federico II**, and for his continuous support throughout this academic journey.

I would like to express my heartfelt gratitude to **Guido Celentano** and **Valerio Kevin Cortese,** the PhD Secretary of the Department of Physics 'Ettore Pancini,' for their invaluable suggestions, kind guidance, and constant encouragement throughout my PhD journey.

I extend my heartfelt appreciation to my colleagues and fellow researchers, in particular **Matteo Manzo, Salvatore Spinosa, Riccardo Damiano, and Michele Viscardi** at the Department of Physics. Your collaborative spirit, thoughtful discussions, and friendship have made the research environment both productive and enjoyable.

My sincere gratitude also goes to my **wife**, friends, and fellow PhD candidates particularly **Fida Hussain**, **Umar Farooq, Jalal Ahmed, Ali Abbasi,** whose companionship, advice, and shared experiences have been invaluable. Your presence made this challenging journey much lighter and more enjoyable.

I am deeply indebted to my **beloved parents**, whose unwavering love, prayers, and sacrifices have been the foundation of all my achievements. Their constant belief in me has been my greatest strength. I also extend my love and gratitude to my **siblings** and my entire family, who stood by my side with encouragement and understanding during both the difficult and joyful moments of this journey.

This PhD journey has been a blend of scientific curiosity, personal perseverance, and the collective support of those around me. To everyone who contributed to this work, whether directly or indirectly, I offer my sincerest thanks.

Table of Contents

List of Figures

List of Acronym

Acronym	Full form
ABL	Atmospheric Boundary Layer
ABLH	Atmospheric Boundary Layer Height
ACTRIS	Aerosol, Clouds, and Trace Gases Research Infrastructure
ACTRIS-IMP	ACTRIS Implementation Project
ALICENET	Automated Lidar-Ceilometer Network
CAIS	Centre for Aerosol In-Situ Measurements
CARS	Centre for Aerosol Remote Sensing
CBL	Convective Boundary Layer
CNR	Consiglio Nazionale delle Ricerche (Italy)
CNR-IMAA	Vaisala CL51 ceilometer installed at the ACTRIS Potenza station
CO2	Carbon Dioxide
CRGM	Cubic Root Gradient Method
CW	Continuous Wave
DBS	Doppler Beam Swinging
DIAL	Differential Absorption Lidar
DWL	Doppler Wind Lidar
EARLINET	European Aerosol Research Lidar Network
ENEA	Italian National Agency for New Technologies, Energy and Sustainable Economic Development
ERF-FIT	Error Function fit
ERIC	European Research Infrastructure Consortium
EZ	Entrainment Zone
FA	Free Atmosphere
FFT	Fast Fourier Transform
FT	Free Troposphere
GM	Gradient Method
HSRL	High Spectral Resolution Lidar
ICOS	Integrated Carbon Observation System
IPM	Inflection Point Method
ISA	International Standard Atmosphere
KF	Klett-Fernald
LGM	Logarithmic Gradient Method
Lidar	Light Detection and Ranging
ML	Mixed Layer
MUSA	Multi-wavelength Aerosol Lidar System
Nd:YAG	Neodymium-doped Yttrium Aluminum Garnet
NeBL	Neutral Boundary Layer
O3	Ozone
OI	Optimal Interpolation
PBL	Planetary Boundary Layer
PBLH	Planetary Boundary Layer Height

PPI	Plan Position Indicator
RCS	Range Corrected Signal
RHI	Range Height Indicator
RL	Residual Layer
RMSD	Root Mean Square Deviation
SBL	Stable Boundary Layer
SCC	Single Calculus Chain
SNR	Signal-to-Noise Ratio
UTC	Coordinated Universal Time
UV	Ultraviolet
VAD	Velocity Azimuth Display
VR	Radial Velocity
WCT	Wavelet Covariance Transform

Abstract

Planetary boundary-layer height (PBLH) is a key parameter for characterising the depth of turbulent vertical mixing in the lower atmosphere and for interpreting near-surface aerosol variability. The objective of this study is to investigate the diurnal and seasonal variability of PBLH using active remote sensing observations within the ACTRIS framework, with the main multi-instrument analysis carried out at the Potenza station, where aerosol lidar, ceilometer, and wind Doppler lidar measurements are simultaneously available. A complementary land-sea comparison is then performed using ceilometer observations at Potenza and at the marine site of Lampedusa to examine how boundary-layer development differs between continental and marine environments under different seasonal conditions.

At Potenza, multi-wavelength aerosol lidar range-corrected signal (RCS) profiles are analysed using a consistent set of lidar-based retrieval techniques, including gradient-based approaches (GM, IPM, LGM, CRGM) and the wavelet covariance transform (WCT), applied at wavelengths of 355, 532, and 1064 nm. Ceilometer backscatter profiles are processed using the error-function fitting method (ERF-fit). Wind Doppler lidar observations are used to estimate PBLH using the vertical-velocity variance method applied to vertical-stare measurements and the wind-shear method applied to DBS (Doppler beam swinging) scans, supported by wind-speed and wind-direction estimates.

The aerosol-lidar results at Potenza show that method-to-method differences occur under stratified conditions and in multi-layer situations, where the retrieved PBLH can vary between algorithms. A small wavelength dependence is also observed, with 1064 nm generally yielding slightly higher PBLH peaks than 532 and 355 nm, while the 355 nm estimates tend to be slightly lower. Overall, a coherent seasonal cycle is observed across wavelengths, with the deepest daytime development in summer, intermediate growth in spring, reduced amplitude in autumn, and the shallowest and most stable conditions in winter. For the wind Doppler lidar, variance and shear-based estimates agree well during peak convective hours, while differences occur during the late-afternoon transition, when turbulence weakens but shear aloft can remain pronounced. The ceilometer-based land-sea comparison highlights a clearer seasonal amplitude and stronger daytime growth at Potenza, whereas Lampedusa shows a weaker seasonal amplitude and a different annual pattern, consistent with the distinct controls acting over marine environments.

Introduction

Understanding how the atmosphere behaves close to the Earth's surface is essential for interpreting many processes that affect air quality, weather, and climate, because this is the region where surface emissions, radiative forcing, and turbulent transport act directly. The lowest part of the troposphere, known as the *planetary boundary layer* (PBL), is therefore of particular interest, since it is directly influenced by surface heating and cooling, frictional effects, and the associated turbulent mixing. As the intensity of mixing changes during the day and from season to season, the depth of the PBL is not constant in time. The PBLH is thus commonly used as a key parameter to describe the vertical extent of near-surface mixing. Despite its importance, retrieval of the PBLH is not straightforward, because the transition between the boundary layer and the free troposphere can be sharp in some situations but gradual or complex in others, and may be affected by clouds, residual layers, or elevated aerosol layers. For this reason, the development and application of observational approaches and retrieval techniques that can provide reliable and continuous estimates of the PBLH are of strong interest.

Reliable monitoring of the PBLH requires observing the vertical structure of the lower troposphere with adequate temporal continuity and vertical resolution. In this respect, active remote sensing techniques, such as lidar (Light Detection and Ranging), are particularly useful because they provide height-resolved measurements that can be used to track the formation and growth of the mixing layer. A lidar system is normally composed of two main components, a transmitter and a receiver. The transmitter emits a laser beam into the atmosphere, and the receiver collects the backscattered radiation returned from atmospheric aerosols and molecules, which is further processed in order to obtain the output signal. In this thesis, the focus is on active remote sensing systems that are widely used for boundary-layer studies, namely aerosol lidar, ceilometers, and Doppler wind lidar. The physical processes required to interpret their signals, including scattering and absorption, as well as the main equations used for data analysis, are also addressed.

This thesis is based on datasets acquired at ACTRIS (Aerosol, Clouds, and Trace Gases Research Infrastructure Network) sites by active remote sensing instruments integrated into established monitoring networks. These networks provide standardised measurements and quality-controlled products that support long-term studies of boundary-layer variability. The main analyses use measurements from the ACTRIS Potenza station, where a complete set of active remote sensing instruments (aerosol lidar, ceilometer, and Doppler wind lidar) allows the retrieval of PBLH from complementary observables. In addition, datasets from the ACTRIS Lampedusa site are also analysed. In this context, the present work focuses on the retrieval of PBLH from aerosol lidar, ceilometer, and Doppler wind lidar datasets, with the aim of implementing widely used retrieval approaches and assessing how the retrieved PBLH behaves under different atmospheric conditions.

The thesis is organised to move from the physical background to the methods and, finally, to the analysis of observations. Chapter 1 establishes the atmospheric context needed for the work, starting from the vertical structure of the atmosphere and introducing the reference model adopted to describe how pressure and temperature vary with altitude. It then turns to the PBL, outlining its main regimes and their diurnal evolution, and define the PBLH. The chapter also illustrates the relevance of PBLH for a range of atmospheric applications and reviews the main observational techniques used to estimate it, with particular emphasis on techniques that use aerosol particles as a tracer in lidar-based retrievals.

Chapter 2 provides the theoretical background and the operating principles of the active remote sensing instruments used in this work for PBL studies. The chapter introduces the main atmospheric monitoring networks considered in the study and, then, reviews the key physical processes that control the interaction between laser radiation and atmospheric constituents, starting from Rayleigh and Mie scattering. Raman scattering is also discussed as inelastic contribution relevant to lidar measurements, as well as absorption by atmospheric gases and aerosols is also outlined because it affects signal propagation. On this basis, the chapter describes aerosol lidar, Doppler wind lidar, and ceilometer systems, including the relevant equations and the framework required to interpret and process their measurements for boundary-layer applications.

Chapter 3 connects the theoretical foundation to the operational analysis. It describes the ACTRIS observation sites of concern to the present work and the main specifications of the instruments used; then, it details the implementation of several PBLH retrieval methods applied to the different datasets. For aerosol lidar, gradient-based methods (GM, IPM, LGM, CRGM) and the wavelet covariance transform (WCT) are applied. For ceilometer profiles, an error-function fit (ERF-fit) approach is used, and for Doppler wind lidar, the vertical velocity variance method and wind-shear-based methods are implemented, with wind speed and direction used to support the interpretation. Finally, the results are presented in the form of comparative plots and observational analysis highlighting the strengths and limitations of each retrieval approach.

Chapter 4 discuss the comparison of the behaviour of PBL over Mediterranean continental and marine environments by using ceilometer observations from two ACTRIS stations, Potenza and Lampedusa. By analysing a full-year (2024) dataset with a consistent retrieval strategy, the chapter examines the annual and seasonal trend of PBLH also investigating how cloud cover and Saharan dust intrusions influence the retrieved boundary-layer height over land and sea during specific months, with the aim of highlighting similarities and differences between the two environments.

Chapter.1

Planetary Boundary Layer Fundamentals

The main purpose of this chapter is to underline the importance of studying the PBLH, which represents the upper limit of the lowest part of the atmosphere, i.e. the PBL, most directly influenced by human activities at the Earth's surface. Since changes within PBL have a clear impact on climate and other atmospheric processes, the chapter begins with a basic introduction to the structure and composition of the Earth's atmosphere, and the atmospheric model is also discussed here. It then focuses on the lower part of atmosphere (troposphere), the region that contains the PBL, and describes the main classifications of the PBL, together with its diurnal behaviour and how it evolves throughout the day. After this, the chapter discusses why the study of the PBL is important and highlights how its characteristics vary across different regions, with particular attention to the Mediterranean area, and in this context the differences between land and marine boundary layers are introduced.

Furthermore, in this chapter the role of aerosol particles in the study of the PBL is also illustrated, since many of the modern techniques used to detect the PBLH rely on aerosol backscattering. Finally, a short overview of the different observational techniques used to study the PBL is provided, including both in situ and remote-sensing approaches. Among these, we are mainly concerned with active remote sensing techniques in this thesis, and they are described in detail in Chapter 2.

1.1 Vertical Structure of Atmosphere

The Earth's atmosphere is a multi-layered system that is essential for supporting life and regulating the climate. In general terms, it can be divided into a lower and an upper region. The lower atmosphere is usually considered to extend up to the top of the stratosphere, at an altitude of about 50 km. The Earth's atmosphere is characterized by temperature and pressure that vary with height. In fact, the variation of the average temperature profile with altitude is the basis for distinguishing the different atmospheric layers. These layers of the atmosphere are summarised below in Figure 1.1 and illustrated hereafter.

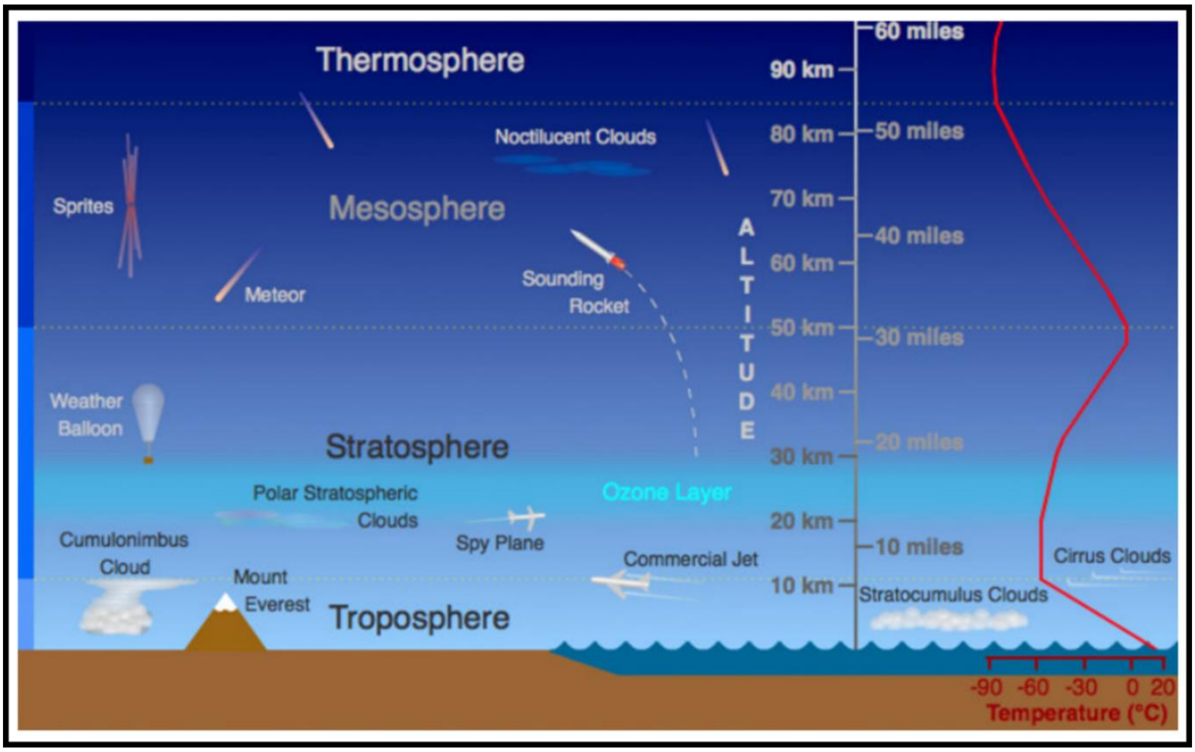

Figure 1.1. Components of Earth Atmosphere. Adapted from **(UCAR Centre for Science Education, n.d.)**.

Troposphere. The lowest layer of the atmosphere, extending from the Earth's surface up to around 11 km (depending on the latitude and time of year), characterized by decreasing temperature with height and rapid vertical mixing. This layer holds about 80% of the atmosphere by mass and almost all the water content, making the troposphere an origin of weather phenomenon such as clouds, storm, and precipitation formation. The tropopause is located at the top of the troposphere, and it is defined as the lowest level at which the rate of decrease in temperature with height is sustained at ≤ 2 K km^{-1} **(Seinfeld & Pandis, 1998)**.

Stratosphere. The region extending from tropopause up to around 50 km altitude belongs to the stratosphere. In contrast to the troposphere, this atmospheric layer has a temperature inversion, where temperatures increase from -60°C at the tropopause to close to 0°C at the stratopause, due to ozone (O_3) absorption of ultraviolet (UV) radiation. The stratopause is located at the top of the stratosphere and it is the region where a maximum in the temperature occurs.

Mesosphere. The region extending from the stratopause up to around 85 km altitude belongs to mesosphere. This atmospheric layer is characterized by declining temperatures with altitude, reaching (-90°C) at the mesopause, which is the top of this layer and the coldest region in the atmosphere.

Thermosphere. The region above the mesopause is called the thermosphere. It is characterized by high temperatures because short-wavelength solar radiation is absorbed mainly by N_2 and O_2, producing strong heating and rapid vertical mixing; under strong solar input, temperatures can exceed 1,500 °C. The ionosphere is a region of the upper mesosphere and lower thermosphere where ions are produced by photoionization **(Seinfeld & Pandis, 1998)**.

Among all the atmospheric layers, the lowest one, the troposphere, is of particular interest and its lowest part, the PBL, is the main focus of this study.

1.2 Atmospheric Model

After describing the vertical subdivision of the atmosphere into layers, it is useful to introduce a physical model that describes how pressure and temperature vary with altitude. A commonly used reference is the International Standard Atmosphere (ISA) **("ISO 2533-1975")**, which provides profiles of pressure, temperature, density and other thermodynamic quantities as a function of height. Such a model is mainly used to describe the behaviour of the troposphere, within which the PBL develops, and to provide a background for the interpretation of the lidar measurements that are discussed in Chapter 2.

The ideal gas law

$$PV = Nk_bT = nRT \tag{1.1}$$

is used to find the relationship between temperature and pressure at local scale **(Wallace & Hobbs, 2006, pp. 63-102)**. In Eq. (1.1), P is the atmospheric pressure, V the volume, T the absolute temperature of the gas, N the number of molecules in the volume, $k_b = 1.38 \times 10^{-23}$ J K^{-1} the Boltzmann constant, n the number of moles, equal to the ratio between the total mass m and the molar mass M, and R the universal gas constant. Introducing the density $\rho = m/V$, the ideal gas law can be written as

$$P = \frac{mRT}{VM} = \rho\, \frac{RT}{M} \tag{1.2}$$

A second fundamental relation describes the vertical distribution of air in hydrostatic equilibrium, where the vertical pressure gradient balances the weight of the overlying air column. Neglecting small-scale perturbations, the large-scale atmosphere can be regarded as being in hydrostatic balance, which implies

$$\frac{dP}{dz} = -\rho g \tag{1.3}$$

where z is the geometric height and g is the acceleration due to gravity. Combining Eq. (1.2) and Eq. (1.3), and assuming that within a given layer the temperature decreases (or increases) linearly with height, it is possible to derive an analytic expression for the vertical profile of pressure P :

$$P = P_i \left(\frac{T}{T_i}\right)^{-\frac{g}{Rk}} \tag{1.4}$$

where P_i is the pressure at height h_i. The parameter k changes from one layer to another according to the sign and magnitude of the temperature gradient, and T_i is the temperature at a reference height h_i in the considered layer. According to this law, temperature varies linearly with altitude h as

$$T = T_i + k(h - h_i) \tag{1.5}$$

These relations provide a simple description of the vertical structure of the atmosphere and are particularly relevant for the troposphere, where the PBL is located. In the PBL, turbulent mixing, radiative heating and cooling at the surface, and entrainment at the top of the layer modify the local temperature profile with respect to the idealised standard atmosphere.

1.3 Planetary Boundary Layer (PBL)

As said earlier, the PBL identifies the lowest part of the troposphere , that is "the part of the troposphere that is directly influenced by the presence of the Earth's surface and responds to surface forcings with a time scale of about an hour or less" **(Stull, 1988, pp. 1-28)**. This layer plays an important role in the behaviour of the atmosphere as a whole and is central to many areas of atmospheric research, including air quality monitoring, climate modelling and numerical weather prediction. Its thickness is highly variable in space and time, typically ranging from a few tens of metres to several kilometres. A variable height and the presence of turbulence are fundamental characteristics of the PBL. Its evolution follows a daily cycle driven by changes in surface variables such as air temperature, relative humidity, net radiative flux and atmospheric stability.

During the day (Figure 1.2a), when the net radiative flux (R_n) at the surface is positive, the ground warms and heats the air close to it. The air near the surface becomes warmer, convection is favoured, and the upper part of the layer is heated by the sensible heat flux (F_{Hs}). At night (Figure 1.2b), in the absence of solar radiation, the surface loses more thermal infrared radiation than it receives from the atmosphere, the net radiative flux (R_n) becomes negative, and the surface cools. This reduces convective activity and reverses the sign of the sensible heat flux (F_{Hs}), the latent heat flux (F_{Es}) and the conductive heat flux (F_{Gs}) into the ground **(Wallace & Hobbs, 2006, pp. 375-417).**

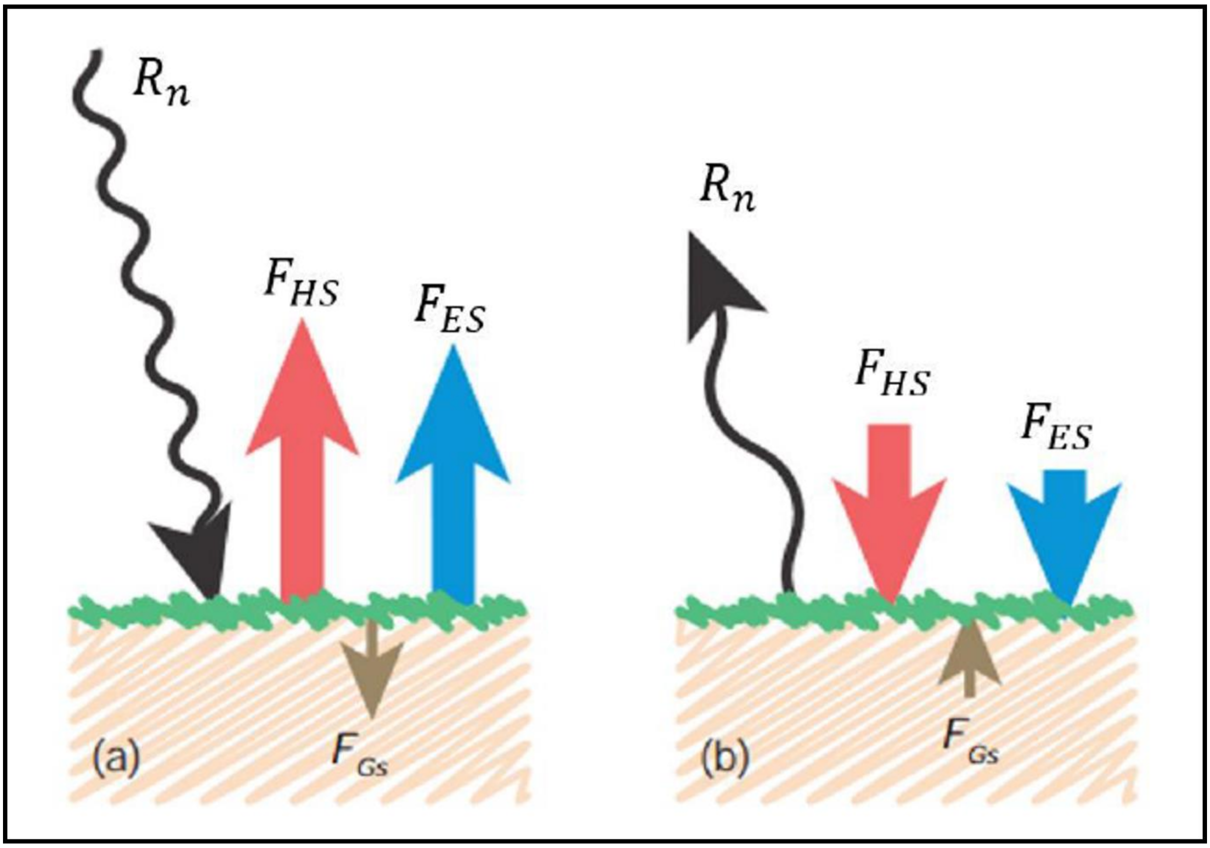

Figure 1.2. Radiative flux at surface - (a) day and (b) night. $\boldsymbol{R_n}$ (Net radiative flux), $\boldsymbol{F_{Hs}}$ (Sensible heat flux), $\boldsymbol{F_{Es}}$ (Latent heat flux), $\boldsymbol{F_{Gs}}$ (Conduction of heat down into the ground). Adopted from **(Wallace & Hobbs, 2006, pp. 375-417)**.

Because the PBL is in direct contact with the Earth's surface, it is strongly controlled by these energy exchanges and by friction, which make the flow turbulent in this layer. The turbulence in the inner part of the PBL is directly linked to the behaviour of the surface sensible heat flux (F_{Hs}), and for this reason the PBL is usually classified into three main types that include: stable or nocturnal boundary layer (SBL), convective boundary layer (CBL) and neutral boundary layer (NeBL) .

1.3.1 Stable or Nocturnal Boundary Layer (SBL)

At night, radiative cooling due to longwave emission reduces the Earth's surface temperature, so that the surface becomes colder than the adjacent air layer. As a result, the air close to the ground cools by transferring heat to the surface, and a stable potential temperature (θ) profile develops in the atmosphere $\left(\frac{\partial\theta}{\partial z} > 0\right)$, as shown in Figure 1.3, with colder air masses near the surface and warmer layers above. The potential temperature θ is the temperature that an air parcel would have when moved adiabatically (i.e. without heat exchange) to a standard reference pressure of 1 bar. In this scenario, vertically displaced air parcels experience a buoyancy force opposite to their motion. The mechanically generated turbulence is therefore weakened, and the turbulent exchanges between the surface and the atmosphere are less intense than those observed during the daytime. Consequently, the SBL develops a lower height compared to the CBL **(Stull, 1988, pp. 499-543)**. In these conditions, the turbulence produces a negative sensible heat flux (F_{Hs}) due to positive temperature fluctuations, correlated with negative fluctuations of vertical velocity and vice versa. The negative sign of F_{Hs} thus indicates a transfer of heat from the atmosphere to the Earth's surface (Figure 1.2b).

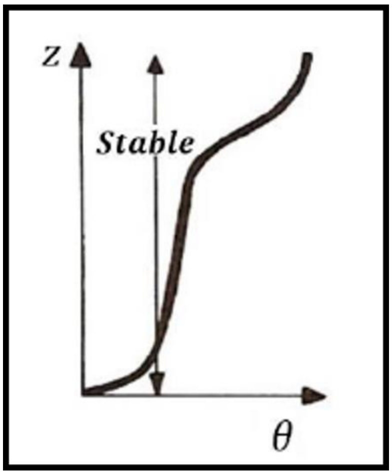

Figure 1.3. Idealized $\boldsymbol{\theta}$ profile of SBL. Adopted from **(Stull, 1988, pp. 151-195)**.

1.3.2 Convective Boundary Layer (CBL)

After sunrise, the net radiative flux (R_n) becomes positive and the ground surface temperature increases. By conduction, the air close to the surface is heated and a convective process begins: the warmer air near the ground becomes less dense and rises, while the relatively colder air aloft moves downward, leading to vertical mixing. In this way, an unstable potential temperature (θ) profile $\left(\frac{\partial\theta}{\partial z} < 0\right)$ develops in the region near the surface, as shown in Figure 1.4. Because of buoyancy, air parcels are accelerated in the vertical direction, which intensifies thermal convection, strengthens turbulence in the layer close to the surface, and enhances the transfer of energy from the ground to the atmosphere by the sensible heat flux (F_{Hs}) and the latent heat flux (F_{Es}), as shown in Figure 1.2a. This increase in turbulence causes the CBL to grow in height (Stull, 1988, pp. 441-497). The CBL is also called the mixing layer (ML), because of the strong mixing generated by this turbulent rising layer.

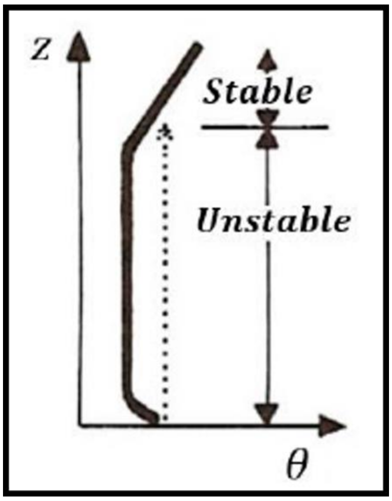

Figure 1.4. Idealized $\boldsymbol{\theta}$ profile of CBL. Adopted from **(Stull, 1988, pp. 151-195).**

1.3.3 Neutral Boundary Layer (NeBL)

As mentioned before, the value of the surface sensible heat flux varies between positive and negative during the day. During the transition periods between daytime and nighttime there are moments when this heat flux is zero or very close to zero. In these cases, the PBL is classified as a neutral boundary layer (NeBL) (Stull, 1988, pp. 151-195). In this layer, the potential temperature (θ) does not change with height and the ground surface does not act as a source of thermal energy $\left(\frac{\partial\theta}{\partial z} = 0 \text{ or } \frac{\partial\theta}{\partial z} \simeq 0\right)$, as shown in Figure 1.5.

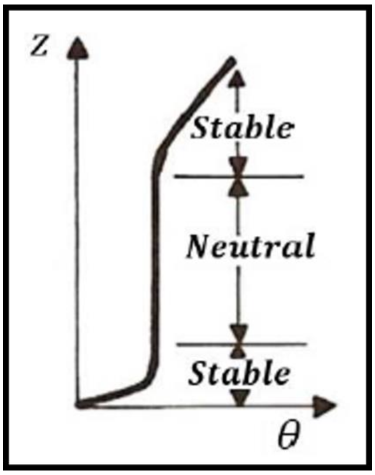

Figure 1.5. Idealized $\boldsymbol{\theta}$ profile of NeBL. Adopted from **(Stull, 1988, pp. 151-195).**

1.3.4 PBL daily Cycle

The three types of PBL described in the previous subsections form a daily cycle that varies according to the interactions between the surface and the atmosphere. Figure 1.6 depicts this cycle and indicates other sublayers that act as divisions and transition regions between the three stages mentioned above.

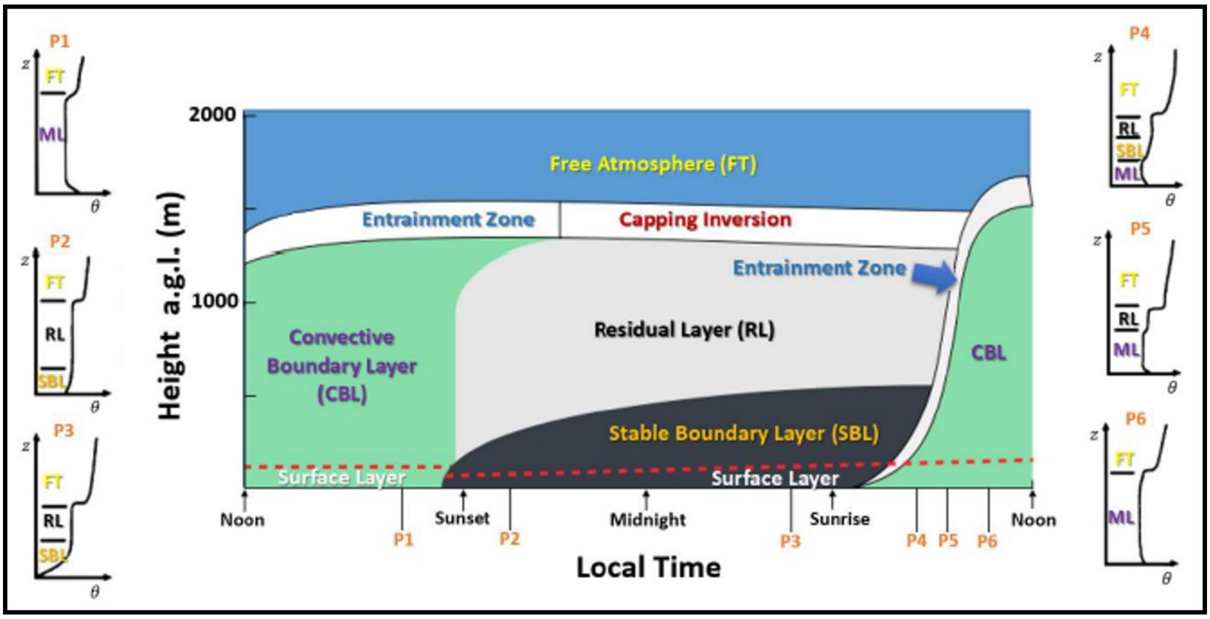

Figure 1.6. Idealized PBL daily cycle. Adopted from **(Stull, 1988, pp. 1-28)**.

In the lower part of Figure 1.6, there is a continuous layer (red dotted line) called the surface layer. This layer is characterized by strong vertical gradients of moisture, wind speed and temperature, especially during the daytime. The CBL (or ML), appears shortly after sunrise and grows in height as the ground is heated by solar radiation, as described in section 1.3.2. Figure 1.6 illustrates this growth and the evolution of the potential temperature profile (P4 → P5 → P6 → P1) **(Stull, 1988, pp. 1-28)**.

In the early hours of the day, there is a layer above the ML known as the residual layer (RL), which preserves characteristics of the previous day's ML and retains the pollutants that remained confined there during the night. As convection develops during the day, the ML deepens and eventually erodes the RL (P5 → P6).

At the top of the CBL there is a stable layer called the entrainment zone (EZ), which forms the interface between the free atmosphere (FA) and the PBL. In this region there is no strong mixing, and the intensity of turbulence decreases with height because of the high stability of this layer. The EZ therefore acts as a barrier for pollutants, keeping them inside the ML.

Near sunset, the net radiative flux (R_n) decreases and approaches zero, which weakens convection. About half an hour before sunset, a new RL forms, and in the following hours, when the (R_n) decreases, the SBL develops and expands during the night (P2 → P3). During the night, the top of the PBL is limited by a capping inversion, which is the EZ, that acts as an interface between the FA and the PBL. This region is highly stable and prevents pollutants from leaving the PBL. As time goes on, sunrise occurs again and this cycle repeats.

1.4 Importance of PBLH in atmospheric studies

The PBL plays a central role in regulating the exchange of momentum, heat, and moisture between the surface and the free troposphere, through processes acting on timescales of minutes to hours. Because it is directly driven by surface forcings such as friction, sensible and latent heat fluxes, and surface moisture exchange, the depth of the PBL is a key parameter for air-quality management, wind and solar energy assessment, and climate modelling **(Li et al., 2017)**. For this reason, the PBLH is an important parameter whose accurate determination is essential for a wide range of studies, including pollutant dispersion, weather forecasting, meteorological modelling and air quality. However, this height cannot be measured directly. Because of the turbulent vertical processes that characterise the PBL, some atmospheric variables such as, aerosol concentration and vertical wind speed show characteristic vertical profiles that allow the identification of the PBLH **(Stull, 1988, pp. 1-28)**. The following paragraphs briefly outline the PBLH specific relevance in various application areas.

1.4.1 Air quality

For air quality management, PBLH is a critical controlling factor, as it regulates the vertical dispersion of pollutants such as $PM_{2.5}$, ozone, and NO_x. It is reported that shallow PBLs at night trap pollutant emissions along the surface, which eventually increases the pollution problem in megacities like Delhi, where wintertime $PM_{2.5}$ levels regularly peak above 300 μg/m³ **(Chowdhury, S., et al., 2019)**. It is also reported that low PBLH in the Indo-Gangetic Plain is linked to heavy smog during the post-monsoon when the stubble-burning process occurs, which makes necessary emergency measures **(Singh, A., et al., 2023)**. Moreover, it is also reported that the Saharan atmospheric boundary layer (ABL) controls the vertical redistribution and transport of dust that eventually makes an impact over other regions of the globe **(Cuesta et** al., 2009). Advanced networks, for example EARLINET (European Aerosol Research Lidar Network), provide harmonised aerosol lidar profiles across Europe through the Single Calculus Chain (SCC), developed within EARLINET and extended within ACTRIS, enabling the provision of standardised aerosol optical products in (near-)real time. Aerosol backscatter profiles are widely used as a proxy to retrieve the atmospheric boundary layer height and can support model evaluation and related regional analyses (D'Amico et al., 2015; Vivone et al., 2021). Hence, because the depth of the PBL influences the dispersion of pollutants, regulatory dispersion models use boundary-layer parameters to characterise the vertical structure controlling transport and dilution (Cimorelli et al., 2005).

1.4.2 Wind and solar energy

Atmospheric turbulence and aerosol distribution that occur inside the PBL are important for the efficiency of wind and solar energy (Stull, 1988, pp. 1-28). Wind turbines operate most efficiently within the well-mixed layer of the CBL, whereas SBL with weak turbulence and lower wind shear reduce the efficiency of wind turbines. Solar energy systems efficiency is also affected by the boundary layer, as a higher depth of PBL spreads aerosols more evenly, which increases irradiance, while shallow polluted PBLs block sunlight and reduce the efficiency of solar energy systems. So, overall PBLH climatology is important for future wind and solar energy projects.

1.4.3 Climate modelling

For climate modelling to work effectively, a reliable estimate of PBLH is required to represent the exchange of heat, moisture, and greenhouse gases between the surface and the atmosphere. Absorbing aerosols, such as black carbon, can heat the lower atmosphere, enhance vertical mixing, and influence large-scale circulation systems such as the monsoon (Lau et al., 2006). Furthermore, Saharan dust intrusions over the Mediterranean and Europe often appear either within the PBL or in elevated layers above it. Observational studies indicate that these dust plumes generate surface radiative cooling and warming inside the dust layer, modifying the vertical temperature profile and atmospheric stability (Peris-Ferrús et al., 2017). These radiative impacts may alter boundary-layer development and influence climate processes at local to regional scales.

1.5 PBL dynamics across Mediterranean continental and marine environments

In this study, we focus on the different ways that can be exploited to identify the PBLH by considering the cases of Mediterranean continental and marine environments, with particular attention mainly given to data relative to the sites of Potenza and Lampedusa. To interpret the behaviour of PBLH at these locations, it is necessary to understand how the boundary layer differs between land and marine regions and which processes mainly control its height.

Over the central Mediterranean, the evolution of the PBL is strongly conditioned by the type of surface and by local circulations, so Potenza and Lampedusa behave quite differently even though they are in the same regional climate. At Potenza, the CNR-IMAA/CIAO and ICOS POT stations are located in a basin of the southern Apennines, about 760 m a.s.l., surrounded by low mountains and at some distance from the coasts. Here the boundary layer is shaped by complex orography, mountain-valley breezes and Mediterranean synoptic patterns, with shallow, often stable layers in winter and deeper convective layers in summer. In addition, long-range transport of Saharan dust frequently introduces elevated aerosol layers above the local mixed layer, altering the radiative balance and stability profile **(Lapenna et al., 2025)**. Lampedusa, in contrast, is a small remote island surrounded by open sea and far from major continental sources. The observations at Lampedusa are used as a reference for the marine boundary layer and for long-range transport studies. The local lower troposphere is typically dominated by a marine boundary layer whose depth is controlled mainly by sea-surface temperature, large-scale subsidence and cloud-topped mixing, while Saharan dust from North Africa is often carried in separate layers, which can affect the marine boundary layer **(ENEA, 2025)**. Cloud cover, aerosol-radiation interactions, and changes in the sea-air temperature contrast become primary drivers of PBL height around Lampedusa. Taken together, these two sites make clear that, within the Mediterranean basin, differences in surface type (mountainous continental vs open sea), orography, local circulations, and the frequency of dust and cloud intrusions jointly control the dynamics and typical depth of the PBL.

1.6 Aerosols and their interaction with the Planetary boundary layer

An aerosol is a population of solid or liquid particles suspended in a gas **(Boucher, 2015)**. Atmospheric aerosols play an important role in a number of key processes related to atmospheric chemistry and physics **(Boucher, 2015)**. Atmospheric aerosols are central to the way the PBL is observed and understood in this thesis work. In practice, most of the techniques used to retrieve PBLH, which will be considered in detail in the second chapter, rely on the fact that aerosol particles are mixed by turbulence and, therefore, act as tracers of the evolving boundary layer. Sharp decreases in aerosol concentration, which usually mark the transition between the well-mixed layer and the more stratified free troposphere, are used to identify PBLH.

At the same time, aerosols do not only help to trace the PBL, but they also affect and modify how the PBL behaves (turbulence, thermodynamics, mixing, height). By scattering and absorbing solar radiation, aerosol layers modify the surface energy balance and the vertical profile of heating, which can increase static stability, weaken turbulent mixing, and lead to a lower daytime PBLH under polluted or dust-loaded conditions. These aerosol-PBL interactions, and their dependence on aerosol type and vertical distribution, have been documented in several observational studies **(Li et al., 2017)**.

The importance and sources of aerosols are not uniform across Potenza and Lampedusa. At Potenza, the CNR-IMAA observatory samples a more regional continental background, where aerosols are largely controlled by transported pollution, seasonal biomass burning, and frequent Saharan dust intrusions over the Apennines. Measurements at this site have been used to characterize aerosol optical properties within the PBL and to derive PBLH from aerosol layering.

Lampedusa, in contrast, is a remote marine station where the lower troposphere is dominated by natural sources of aerosol such as sea salt, forest fires, and mineral dust. In addition, the burning of fossil fuels, including shipping pollution in southern Europe and in large Mediterranean cities, provides a highly complex and dynamic mixture of organic and inorganic aerosol and aerosol precursors in this region **(Mallet et al., 2019)**. Aerosol composition and radiative forcing help identifying how these particles shape the thermodynamic structure of the marine boundary layer and contribute to evaluating dust and pollution episodes over the open Mediterranean. In both cases, therefore, aerosols are used as tracers to retrieve PBLH, and as active drivers of boundary-layer dynamics via their radiative and microphysical effects.

1.7 Measurements techniques used for the estimation of PBLH

Although in this thesis work the main focus is on lidar technology, an active remote sensing technique that can be used to estimate the PBLH and will be illustrated in detail in the second chapter, for the sake of completeness, here other techniques used for the study of the PBL, including both in situ and remote sensing approaches, are briefly described, highlighting the basic information about them.

1.7.1 In Situ Techniques for the PBLH Estimation

In situ techniques have played a central role in how the PBLH has been defined and quantified, well before the widespread use of ground-based remote sensing, because they provide direct vertical profiles of temperature, humidity, wind, and turbulence that can be used to identify the boundary-layer top **(Seibert et al., 2000)**. In situ procedures include direct measurements of atmospheric variables inside the PBL with devices mounted on balloons, aeroplanes, or tethered platforms. These techniques provide comprehensive vertical profiles of temperature, humidity, wind, and turbulence, that are used for determining the PBLH.

Radiosondes are still the most common in situ tool, and provide vertical profiles of temperature, humidity, wind speed and direction, and PBLH is typically inferred from features such as a capping inversion in potential temperature, sharp gradients in moisture, and changes in wind shear **(Li et al., 2021)**. Because of their global observing network and long historical record, radiosonde data support many climatological studies of mixing height and have been widely used to test and calibrate PBL models.

Tethered balloons are flying platforms equipped with sensors, and they are used to complement radiosonde soundings by providing detailed observations of the PBL through high-resolution vertical profiles or time series within roughly the lowest kilometres. Sounding balloons measure wind, temperature and humidity at different heights during their flight, and provide vertical profiles that describe the atmospheric structure and reveal features such as inversion layers and sharp gradients near the boundary-layer top **(Seibert et al., 2000)**.

Aircraft measurements help us see how the PBL behaves over a wider area. In early work such as **(Lenschow, 1970)**, research aircraft were used to study the PBL by flying back and forth at different fixed heights and analysing the three-dimensional wind and temperature fields and their turbulent fluctuations. From these data, the top of the boundary layer can be identified as the height up to which turbulence is continuous and above which temperature and other variables stop being nearly uniform and start to change more strongly with height. In more recent studies, aircraft have often provided a direct way to diagnose the boundary-layer top using turbulence measurements, while coincident profiles of temperature and wind are analysed to locate the transition from the well-mixed boundary layer to the more stable air aloft **(Dai et al., 2014)**.

Each of these methods has some strengths and limitations. Radiosondes provide vertical profiles through the depth of the atmosphere and long-time series, but they are usually launched only once or twice per day at standard global observation times, not continuously through the day, so they cannot fully resolve the rapid diurnal evolution of PBLH. Tethered balloons can sample the lower PBL with fine vertical and temporal resolution and are useful for studying small-scale processes in detail, but they are logistically demanding, restricted to relatively low heights and fair-weather or low-wind conditions, and cannot operate continuously over long periods. In a similar way, aircraft campaigns provide a three-dimensional picture of the boundary layer and allow direct measurements of turbulence; however, they are expensive, usually run for short intensive periods, and are tied to specific field experiments rather than routine long-term monitoring.

For these reasons, direct in situ measurements are still important to define PBLH in a way that is consistent with the actual temperature and turbulence profiles, and to check how well models perform. At the same time, in the modern observing system they are more and more often combined with ground-based remote sensing (for example aerosol lidar, ceilometers, wind profilers), which can follow PBLH continuously with high time resolution and over many years.

1.7.2 Remote Sensing Techniques for the PBLH Estimation

Remote sensing techniques provide continuous and automated monitoring of the PBL using ground-based sensors or instruments carried by satellites and, therefore, overcome the temporal and spatial constraints of in situ methods. These include sodar (sound detection and ranging), microwave radiometers, and lidar technologies **(Dang et al., 2019)**.

Ground-based sodar uses acoustic pulses, where information on both the intensity of turbulence and the gradient of temperature and wind can be reflected from the backscatter intensity profile measurements. Mixing height is then estimated from the depth of the turbulent layer and from characteristic changes in the backscatter profile. Ground-based microwave radiometers measure the natural microwave emission of the atmosphere at several frequencies. They are used to retrieve continuous vertical profiles of temperature and humidity in the lower troposphere. In boundary-layer studies, these temperature and humidity profiles are used to estimate PBLH by identifying temperature inversions and strong changes in humidity or stability that separate the well-mixed boundary layer from the more stratified air above. Additionally, in order to estimate PBLH, lidar systems use laser pulses to measure backscatter from the atmospheric particles. Aerosol lidar identifies abrupt changes in particle concentration at the boundary layer top, while Doppler lidar measures turbulence and wind shear to estimate the PBLH. Both approaches are explained in detail in the second chapter.

Each technique offers specific advantages and drawbacks. Sodar offers a relatively simple and low-cost remote-sensing option that can operate continuously and provide high temporal and vertical resolution, and it can identify elevated temperature inversion layers. However, its usable range is limited to a few hundred metres up to about 1 km, and its data availability decreases under specific weather situations. Microwave radiometers deliver good estimates of temperature and humidity in the lower troposphere with high temporal resolution, but their vertical resolution decreases with height, and the retrieved profiles become unreliable in cloudy or rainy conditions **(Dang et al., 2019)**. Lidar provides continuous measurements with high temporal resolution and broad vertical coverage, and extensive lidar networks now offer a large volume of observations. However, lidar systems are expensive, the data quality near the surface is limited by the blind zone, and the technique is easily affected by multiple aerosol layers or clouds, which can complicate boundary-layer detection **(Dang et al., 2019)**.

Although lidar technology has some shortcomings, it is still one of the most widely used techniques for boundary-layer studies. For this reason, in this thesis work lidar is chosen as the primary tool for PBLH estimation, because it combines high temporal and vertical resolution with direct sensitivity to aerosol structures that are central to this study. The aerosol lidar, wind Doppler lidar and ceilometer used to estimate the PBLH in this thesis work are outlined in detail in Chapter 2.

Chapter.2

Active Remote Sensing of the Atmosphere

As discussed in the previous chapter, our primary focus is on the PBL, which is the lowest region of the troposphere. This layer is particularly important for weather forecasting, climate modelling and atmospheric processes. Various techniques have been developed to study the structure and the dynamics of the PBL. These techniques can be broadly grouped into in situ and remote sensing techniques as discussed in detail in chapter 1. This chapter mainly focuses on the active remote sensing techniques, which can provide data with high temporal and spatial resolution that is necessary for understanding the vertical structure and temporal evolution of the PBL. Some of the well-known active remote sensing techniques are aerosol lidar, wind Doppler lidar, and ceilometers. These techniques allow detecting aerosol backscatter profiles, figuring out how high mixing layers are, and looking at wind velocity profiles that make them essential for boundary layer meteorology. The next sections illustrate each active remote sensing technique, including how they work, the equations that apply to them, and how to get the data back.

This chapter not only goes into detail about active remote sensing techniques, but it also discusses the basic physical processes involved in laser radiation interaction with the atmospheric constituents. For this purpose, the processes like Rayleigh scattering, Mie scattering, and Raman scattering, which play a crucial role in interpreting the active remote sensing signals, are also reviewed. Along with that, the absorption of laser energy by gases and aerosols in the atmosphere is also illustrated, since it is important to understand the mechanics underlying these interactions in order to accurately characterise and interpret remote sensing observations in the PBL.

2.1 Networks for the Monitoring of Atmosphere

Over the past few decades, several international networks have been established to coordinate standardised atmospheric measurements. As a result, long-term, high-resolution datasets for operational and research purposes can now be produced. EARLINET, Cloudnet, and ALICENET (Automated Lidar-Ceilometer network) are some of the major observational networks. Most of them are now part of ACTRIS, a large pan-European project that brings together remote sensing and in-situ monitoring platforms in different climate zones.

ACTRIS has been established as a European Research Infrastructure Consortium (ERIC) that covers a wide range of climate zones from the Mediterranean to the Arctic, allowing long-term studies of aerosol-cloud interactions and boundary-layer processes under diverse meteorological conditions **(ACTRIS ERIC, n.d.)**. At present ACTRIS involves more than one hundred measurement platforms distributed across over twenty-two countries around the world, which makes it the largest ground-based atmospheric research infrastructure in Europe. The remote sensing observatories can have high-power multi-wavelength Raman and polarisation lidars, automatic low-power ceilometers, radar wind profilers, and microwave radiometers. The observational facilities are complemented by central facilities such as the Centre for Aerosol Remote Sensing (CARS) and the Centre for Aerosol In-Situ Measurements (CAIS), that provide quality assurance, reference calibration, and data harmonisation services, ensuring that data collected at different stations are fully comparable. Additionally, ACTRIS also provides access to its facilities and data through open services, in order to support both scientific research and policy relevant applications such as climate assessment and air quality monitoring. Figure 2.1 represents the geographical distribution of countries that are included in the ACTRIS implementation project (ACTRIS-IMP). This map demonstrates the level of official commitment and participation across Europe, which includes both EU and non-EU member states. It highlights the countries that are officially committed to ACTRIS ERIC along with those in the process of joining, and those participating at the level of research performing organizations.

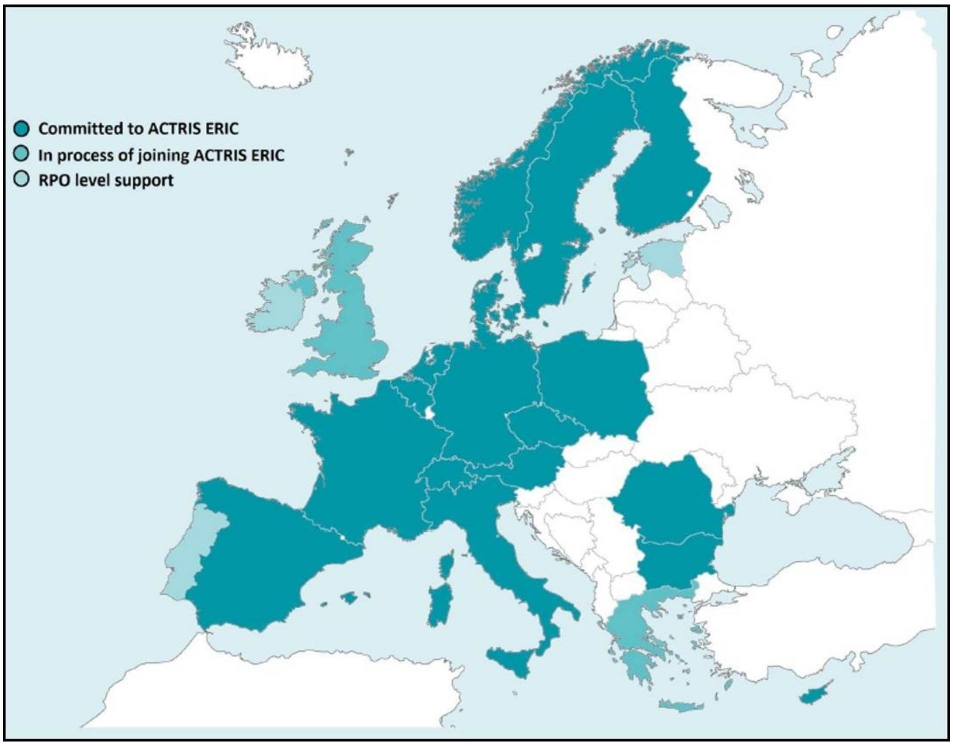

Figure 2.1. Level of official commitment of Countries participating in the ACTRIS implementation project (ACTRIS-IMP) (Häme et al., 2023).

EARLINET, which started in 2000, is the European Lidar Network for aerosol profiling that covers the whole continent (EARLINET, n.d.). It has 27 stations, most of which have multi-wavelength Raman lidars that operate at 355 nm, 532 nm, and 1064 nm. The network regularly provides vertical profiles of aerosol backscatter and extinction coefficients, as well as the respective uncertainties. Many EARLINET sites operate both high-power Raman lidars and low-power automatic ceilometers. Where these instruments are co-located, ceilometer backscatter observations are calibrated and validated through intercomparison with the reference lidar measurements, which supports more reliable retrieval of boundary-layer structure (e.g., mixing-layer height) from the ceilometer signal.

Over the years EARLINET has developed strict quality assurance protocols to ensure the comparability of measurements across different stations, and its database now provides a comprehensive collection of ground-based aerosol lidar profiles in Europe. The network covers a broad range of environments, from polluted urban regions to remote background sites, which allows the investigation of aerosol transport, volcanic eruptions, dust outbreaks, and long-range pollution episodes.

Cloudnet is a European network of ground-based remote sensing stations with about 20 active stations **(Cloudnet, n.d.)**. The stations are located in different climatic regions of Europe, and each site has vertically pointed cloud radars, lidars, or ceilometers, as well as microwave radiometers, which enable long-term monitoring of cloud occurrence, microphysical properties, and their variability. The Cloudnet data portal provides a data processing and curation service for ground-based cloud remote sensing measurements, including centralised processing, quality control, data harmonisation and archiving. The Cloudnet database has data products like attenuated backscatter profiles, cloud classification, and the amount of water in liquid or ice form. The Cloudnet products are commonly used for evaluating the representation of clouds in weather forecast and climate models, for monitoring boundary layer dynamics, and they are also applied for satellite products validation and aviation meteorology.

ALICENET, operated by CNR-ISAC, is an Italian national network of automated lidar-ceilometers that operates h24 **(ALICENET, n.d.)**. There are about 20 to 30 observatories that are distributed across Italy in urban, coastal, mountain, and volcanic sites which makes it possible to study aerosol dynamics in a wide variety of atmospheric conditions as shown in Figure 2.2. The network provides near real time information on the vertical distribution of aerosols and boundary layer evolution, supporting both scientific research and operational air quality monitoring. ALICENET measurements are also integrated into the European E-PROFILE programme, which enhances the use of ceilometer data in weather services and contributes to the continental coverage of aerosol and boundary-layer observations.

Figure 2.2. Location and naming of the ALICENET stations. Adopted from (Bellini et al., 2024).

2.2 Role of Lidar in Atmospheric remote sensing and monitoring networks

Lidar is an active remote sensing technique that plays a significant role for studying the atmosphere because of its ability to provide high resolution vertical profiles of aerosols and molecules that help scientists to learn more about the aerosol properties, boundary layer dynamics, and long-term climate patterns. In contrast with passive remote sensing systems based on the natural light sources, a lidar system use laser pulses as a source that are transmitted in the atmosphere and interact with the atmospheric constituents. The backscattered signal is collected and analysed to get the desired information. The lidar systems allows for continuous, unattended, and autonomous operation in ambient conditions, making it possible to understand atmospheric processes from near surface levels to the lower thermosphere.

Lidar technology has evolved significantly since it was first used in atmospheric studies in the 1960s (McCormick, 2005). The invention of tuneable laser sources, narrowband filters, and sensitive detectors has made it possible to build advanced systems that are now used on the ground, in planes, and on satellites. These advancements in lidar technology have improved the system and made it more useful for both operational monitoring and research, which enables a variety of atmospheric investigations. These includes characterization of clouds and aerosols and researching stratospheric ozone and climate-related processes.

Scattering and absorption processes have the strongest influence on the lidar signal, since scattering controls how much of the transmitted radiation is redirected back to the receiver, while absorption reduces the fraction of transmitted radiation along the path, thereby weakening the backscattered return.

The accuracy and reliability of lidar measurements depend on the strength of the backscattered signal from atmospheric constituents, since this directly affects the signal-to-noise ratio of the return. A strong and clear returned signal makes it easier to get correct information on aerosol characteristics and the height of the boundary layer. A weak and noisy returned signal, on the other hand, leads to higher uncertainties and unreliable outcomes.

To understand lidar return signals, it is important to know about elastic and inelastic scattering, or molecular and aerosol scattering, and their processes in the atmosphere. The theoretical basis for all retrieval algorithms, that are used to extract optical and microphysical properties from the atmospheric components and boundary layer height relies on these scattering mechanisms and on the analysis of the range corrected signal (RCS).

In the next section these physical processes with a focus on atmospheric scattering and characterization of the atmospheric constituents, will be discussed.

2.3 Scattering and absorption in the atmosphere

The phenomenon of atmospheric scattering occurs when electromagnetic radiation interacts with the atmospheric constituents. When light interacts with atmospheric aerosols or molecules, it generates oscillations in their dipole moments, which then re-radiate energy in multiple directions. The re-emission of light results in the redistribution of radiation intensity in various directions along with a portion of the energy potentially being absorbed. The complexity of the physical mechanism behind the process of scattering depends upon different factors that includes the nature, composition and size of the atmospheric particles as well as the wavelength of the radiation that interact with the particles. An important factor that determines the scattering regime is the size parameter, which is defined as $x = 2\pi R/\lambda$, where R is the radius of the particle and λ the light wavelength. Rayleigh theory, which applies to molecules, governs scattering when x is much less than 1 and it is therefore mostly considered as molecular scattering. Mie theory is used when x is much greater than 1, in order to take into account, the complicated interactions that happen with bigger aerosols like dust, smoke, or water droplets, and is therefore generally associated with aerosol scattering because of their size.

The scattering process is divided into two main types that includes elastic and inelastic scattering. Elastic scattering is further categorized into two types that are Rayleigh and Mie scattering. In the process of elastic scattering, the wavelengths of the incoming and scattered photons do not change its energy. Elastic scattering is an important process in the atmosphere of Earth, and it is crucial for understanding lidar backscatter signals. On the other hand, inelastic, Raman scattering, changes the energy of photons after interacting with the atmospheric particles and thus changes their wavelength, because during this process the exchange of energy with molecular vibrational or rotational states occurs. Raman scattering gives us useful information about the optical characteristics of the molecular part of the atmosphere.

Besides scattering in the atmosphere, also the process of attenuation (or absorption) happens when light interacts with the atmospheric constituents. Attenuation denotes the total loss of radiation intensity along the propagation path, and it includes both scattering and absorption effects from molecules and aerosols. As a part of this process, molecules absorb some of the energy from the electromagnetic wave and turn it into internal energy, such as electronic, rotational and vibrational excitations. As these energy levels are quantized, so the absorption process only happens at certain wavelengths, and that is the reason why gases like CO_2, O_3, and water vapour have distinct spectral lines or bands. Along with that, aerosols particles attenuate the transmitted and backscattered radiation by both scattering and absorbion, which depends on their size and composition. These processes are jointly crucial for the atmospheric radiative transfer along with its direct impact on the lidar signals, as the backscattered and transmitted radiations get attenuated during their propagation. In Raman lidar applications, this process of attenuation is mainly important, as it affects both the outgoing laser beam and the inelastic return at the Raman wavelength, therefore influencing the accuracy of retrieved backscatter and extinction profiles. A schematic representation of the main processes occurring when incident light interacts with atmospheric particles and molecules is shown in Figure 2.3.

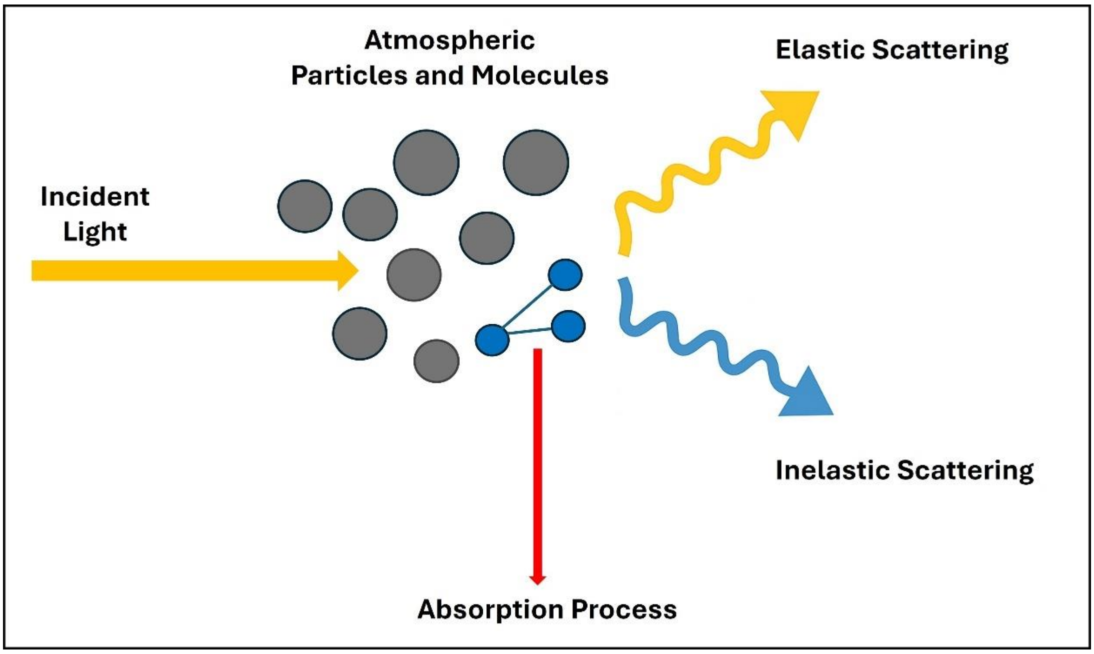

Figure 2.3. A schematic representation of elastic and inelastic scattering processes, along with absorption, that occur when incident light interacts with the atmospheric constituents.

2.3.1 Rayleigh Scattering

Rayleigh scattering, as mentioned before, is an elastic scattering process that explains how electromagnetic radiation interacts with particles that are much smaller in comparison with the wavelength of the radiation, like N_2 and O_2 molecules in the air. This process is important in atmospheric optics and is a part of figuring out lidar measurements, especially in the upper troposphere and stratosphere where the aerosols are very less in amount and the backscattered signal is dominated by molecules. This molecular return acts as a reliable reference, because it can be accurately calculated from known pressure and temperature profiles. Lidar systems use this molecular signal to define the reference height for inversion methods, allowing the separation of aerosol and molecular contributions. Consequently, Rayleigh scattering not only describes the fundamental molecular interaction with light, but it also provides the reference signal for the interpretation of lidar measurements.

In lidar studies, the scattering cross section is a fundamental quantity because it links the microscopic interaction of light with individual molecules to the macroscopic signal received by the instrument. At the molecular level the scattering cross section denotes the effective area of an individual molecule that participates in the scattering process. When multiplied by the molecular number density, it gives the volume scattering or backscatter coefficient, that determines how much light is redirected toward the lidar receiver per unit volume.

Consequently, the cross section determines how the observable atmospheric return signal is produced by the combined scattering of all air molecules. It is convenient to express the total Rayleigh scattering cross section in terms of the air's refractive index n and the number density of scatterers n_{sc} **(Adam, 2012):**

$$\sigma_{sc} = \frac{24\pi^3\left(n^2-1\right)^2}{\lambda^4 n_{sc}^2 (n^2+2)^2} F_k \tag{2.1}$$

where λ is the wavelength, n is the refractive index of air, n_{sc} is the number density of scatterers, and F_k is the King correction factor that takes into account the effects of depolarization.

As shown in (2.1), Rayleigh scattering depends on the inverse fourth power of the wavelength. This explains why the sky looks blue at sunrise and reddish during the sunset time. In fact, this wavelength dependency affects the intensity of the molecular return signal, which is much stronger at shorter wavelengths as compared to longer wavelengths. The molecular backscatter coefficient, which quantifies the amount of light directly backscattered toward the lidar receiver at 180°, is represented by:

$$\beta(\lambda) = \sum_j n_j \frac{d\sigma_{j,sc}}{d\Omega}(\pi, \lambda) \tag{2.2}$$

that takes into account the total differential scattering cross sections (in the direction of backscatter) for all molecular species j and their number densities n_j. The resulting molecular return constitutes a well-defined reference signal, because it can be precisely calculated from known atmospheric parameters such as pressure and temperature. In practical lidar measurements, this molecular contribution is essential for distinguishing the portion of the signal produced by air molecules from that produced by aerosols **(Wandinger, 2005, pp. 1-18)**. In this way, the Rayleigh-scattered signal provides the baseline needed to interpret atmospheric backscatter profiles correctly.

Rayleigh scattering gives the molecular baseline profile above the aerosol filled boundary layer, when using lidar to estimate PBLH. In a clear sky condition, the top of the boundary layer is identified as the height where a transition from enhanced aerosol backscatter to the molecular profile happens. Thus, understanding the Rayleigh scattering cross section and the associated molecular backscatter coefficient is essential for accurately estimating the PBL height as well as for calibrating instruments.

2.3.2 Mie Scattering

Mie scattering theory applies when electromagnetic radiation interacts with particles whose size is comparable to or larger than the wavelength of the incident radiation. This regime is particularly important for aerosols, especially within the PBL, because their typical sizes are comparable or larger than the lidar operating wavelengths, such as 355 nm and 532 nm, leading to high scattering efficiency. As compared to Rayleigh scattering that works for molecules and the smallest aerosol nuclei, Mie scattering describes the interactions of radiation with larger aerosol particles, for which the scattering strongly depends on particle size and refractive index.

The total Mie scattering cross section is given by this equation **(Zangwill, 2012, pp.775-821)**:

$$\sigma_{Mie} = \frac{2\pi}{k^2} \sum_{l=1}^{\infty} (2l + 1)(|a_l|^2 + |b_l|^2) \qquad (2.3)$$

where $k = 2\pi/\lambda$ is the wavenumber in the surrounding medium, and $a_l$and b_l are the Mie (expansion) coefficients of the external field for a homogeneous sphere, obtained from the electromagnetic boundary conditions at the particle surface. They depend on the size parameter $x = kR$ and on the particle refractive index relative to the surrounding medium. Since the scattered field is expressed as a series of vector spherical harmonics, the index l identifies the multipole (partial wave) order, and the summation in Eq. (2.3) includes the contribution of all multipole orders to the total scattering cross section. In Mie theory, efficiency factors are defined as the ratio between a cross section and the particle geometrical cross-sectional area, and they are widely used because they allow scattering behaviour to be compared for particles of different sizes and at different incident wavelengths. The scattering efficiency is given by:

$$Q_{sca} = \frac{\sigma_{sca}}{\pi r^2} \qquad (2.4)$$

This parameter shows how well a particle scatters light compared to the area of its geometric cross-section. Because of diffraction and interference, Q_{sca} can be greater than one. In addition to scattering efficiency, absorption efficiency (Q_{abs}) and extinction efficiency (Q_{ext}) are important for lidar applications because they quantify how much of the incident radiation is removed from the propagation beam by particles. In particular, extinction ($Q_{ext} = Q_{sca} + Q_{abs}$) represents the total attenuation of light by both scattering and absorption processes.

Mie scattering often dominates within the PBL because aerosol particles are typically much more abundant there than in the free troposphere. In elastic lidar observations, the received signal is the sum of a particulate contribution (described by Mie theory) and a molecular contribution (described by Rayleigh theory). The transition from a strong aerosol backscatter layer below the PBL top to a comparatively weaker, molecule-dominated return above it is therefore one of the key signatures used to identify the PBL height. While Rayleigh theory accounts for the molecular component, Mie theory is used to relate aerosol optical coefficients such as backscatter and extinction to particle microphysical properties (size distribution and refractive index), which are essential for quantifying aerosol-radiation interactions and for retrieving aerosol profiles from lidar measurements.

2.3.3 Raman Scattering

As defined in section 2.3, Raman scattering is an inelastic process in which photons exchange energy with atmospheric molecules. When a photon interacts with a molecule, scattering can be elastic (Rayleigh) or inelastic (Raman). In the inelastic case, energy is exchanged between the radiation field and the molecule's internal degrees of freedom, so the scattered photon has a different energy and is shifted to the Stokes or anti-Stokes frequency. In the Stokes case, the photon transfers part of its energy to the molecule, while in the Anti-Stokes case, the photon gains energy from a molecule that is already in an excited state. These two types of Raman shifts are key for atmospheric lidar, since they allow probing the vibrational and rotational structure of different molecules **(Wandinger, 2005)**.

To connect measurable Raman signals to molecular properties, Placzek's polarizability theory is used to derive differential backscatter cross sections under non-resonant conditions that are well satisfied for typical lidar laser wavelengths and for the main atmospheric molecules of interest. The relevant molecular parameters include the mean polarizability, the anisotropy of polarizability, and their derivatives with respect to the vibrational normal coordinate, denoted as α, γ, α' and γ' **(Wandinger, 2005)**.

For vibration-rotation Raman scattering, the differential cross section in the Stokes branch is:

$$\left(\frac{d\sigma}{d\Omega}\right)_{VRR}^{Stokes} = k_{\bar{\nu}}(\widetilde{\nu_1} - \widetilde{\nu_{vib}})^4 \frac{b_{\bar{\nu}}^2}{1-exp(-hc_0\widetilde{\nu_{vib}}/k_BT)}\left(a^2 + \frac{7}{45}\gamma^2\right) \tag{2.5}$$

and similarly, for anti-stokes vibration-rotation Raman backscattering the differential cross section is written as:

$$\left(\frac{d\sigma}{d\Omega}\right)_{VRR}^{anti\text{-}Stokes} = k_{\bar{\nu}}(\widetilde{\nu_1} + \widetilde{\nu_{vib}})^4 \frac{b_{\bar{\nu}}^2}{exp(hc_0\widetilde{\nu_{vib}}/k_BT)-1}\left(a^2 + \frac{7}{45}\gamma^2\right) \tag{2.6}$$

where $\frac{d\sigma}{d\Omega}$ is the differential scattering cross section, $k_{\bar{\nu}}$ is the scattering constant factor, $\widetilde{\nu_1}$ is the incident laser wavenumber, $\widetilde{\nu_{vib}}$ is the vibrational wavenumber of the molecule, $b_{\bar{\nu}}^2$ is the square of the zero point amplitude of the vibrational mode , h is the Planck's constant , c_0 is the speed of light in vacuum, k_B is the Boltzmann's constant, and $T$is the absolute temperature of the medium.

These cross sections are of central importance for Raman lidar, since they provide the quantitative link between the measured inelastic backscatter and the molecular number densities. In practice, they form the theoretical basis for retrieving atmospheric parameters such as water vapor mixing ratio, temperature (via rotational Raman), and aerosol extinction profiles.

2.3.4 Absorption Process

In addition to scattering processes, electromagnetic radiation is also attenuated in the atmosphere through molecular absorption. In lidar applications, absorption is significant because it contributes to the extinction that attenuates the radiation on both the outgoing and return paths. To describe absorption in a quantitative way, it is necessary to introduce the concept of the absorption cross section, which provides the link between the interaction of photons with individual particles and the overall signal attenuation detected by the lidar system. In practice, the absorption cross section specifies the probability that a photon of wavelength λ is absorbed by a single particle, and when it is multiplied by the number density n� of a species, it yields the absorption coefficient:

$$\alpha_{abs}(\lambda) = n_j \sigma_{j,abs}(\lambda) \quad (2.7)$$

In lidar studies, scattering and absorption are treated together in terms of the extinction cross section:

$$\sigma_{ext}(\lambda) = \sigma_{sc}(\lambda) + \sigma_{abs}(\lambda) \quad (2.8)$$

with the corresponding extinction coefficient:

$$\alpha(r, \lambda) = \sum_j n_j(r)\ \sigma_{j,ext}(\lambda) \quad (2.9)$$

with $n_j(r)$ the number density of the j-th species. The extinction coefficient is often written as the sum of molecular and particulate contributions, both of which include scattering and absorption. In this way, aerosol absorption can contribute alongside molecular absorption.

For lidar studies, absorption is fundamental because it determines how strongly radiation is attenuated along the propagation path and is explicitly represented in the lidar equation through the extinction term. Accordingly, accurate absorption cross sections are required whenever gas absorption contributes significantly to the lidar transmission, because they determine the absorption component of the extinction coefficient and, therefore, the two-way attenuation of the measured signal.

2.4 Lidar System Architecture and signal acquisition

In many atmospheric lidar systems, a solid-state Nd:YAG laser is used because it is a robust, high-power source whose fundamental emission at 1064 nm can be efficiently frequency-doubled and tripled to provide the commonly used lidar wavelengths at 532 nm and 355 nm. The transmitter and the receiver are the two main parts of a lidar system. A beam of monochromatic, collimated laser pulses of short duration in the range of nanoseconds (ns), depending on the system, and well-defined wavelengths is sent into the atmosphere by the transmitter. The transmitter is typically composed of the laser head and a wavelength-conversion stage (when harmonics are used), together with beam-conditioning optics (e.g., mirrors and a beam expander/collimator) that shape and direct the outgoing beam. As the laser beam propagates through the atmosphere, molecules and particles scatter and absorb part of the radiation.

A receiver records the backscatter signal. The receiver is the part of the lidar that collects the backscattered radiation and converts it into an electrical signal for acquisition. It is typically composed of a telescope, wavelength-selection optics (e.g., beam splitters and interference filters), one or more photodetectors (PMTs/APDs depending on wavelength), and acquisition electronics. The telescope in the receiver collects the backscattered signal and directs it towards the photodetector. After measuring the quantity of backscattered light, the photodetector converts it into an electrical signal. Figure 2.4 schematically depicts the major components of a lidar system. Additional components include a computer for data collection, a power supply, and a cooling system for the laser, as well as a digitiser for converting the signal from analogue to digital and record it as a function of time, i.e. the distance from the lidar **(Kovalev & Eichinger, 2004)**.

A lidar system can be set up in either coaxial or biaxial geometry, depending on how the optical axes of the transmitter and receiver line up with each other. In the case of a coaxial (monostatic) configuration, the transmitted beam is aligned with the receiver optical axis; in this configuration, the geometrical overlap between the laser beam and the receiver field of view increases rapidly with distance, and full overlap is typically achieved at relatively short ranges. In a biaxial configuration, the transmit and receive axes are laterally separated, so the geometrical overlap builds up more gradually and full overlap is achieved only at larger ranges. As a result, the blind region in a biaxial system is generally larger than in a coaxial system.

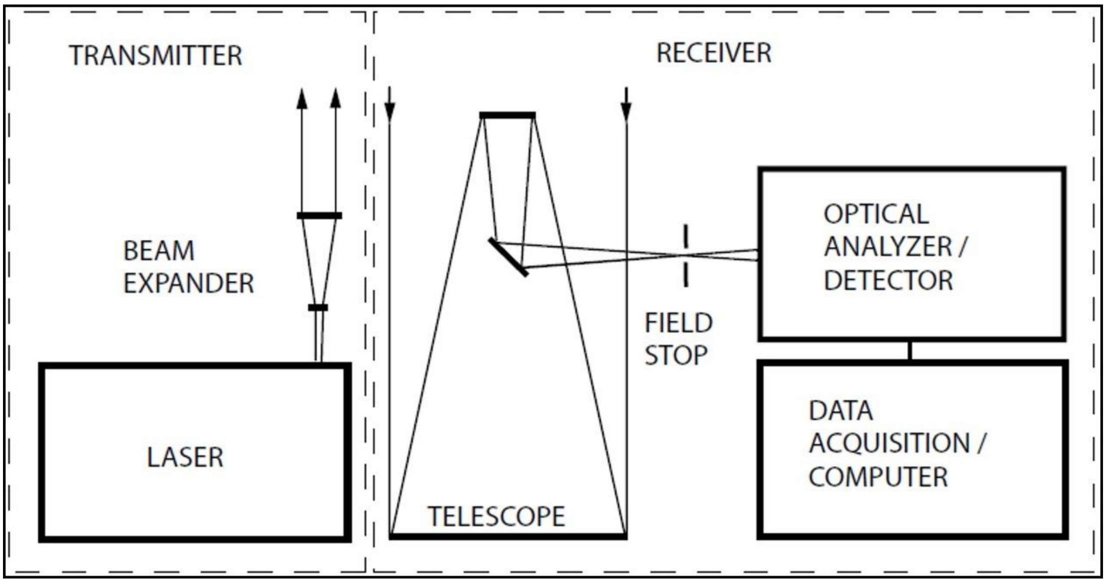

Figure 2.4. Simplified illustration of the lidar system (Sassen, 2005).

A lidar records the return signal in one or more detection channels, including the elastic channel and, when implemented, Raman-shifted channels defined by the receiver optics and filters. The backscattered signal may be recorded using one of two methods that includes photocounting (photon counting mode) or analogue (current mode). In analogue mode, the signal from the photodetector is directly digitised using acquisition electronics. The signal to noise ratio (SNR) decreases proportionally to the square of the range. Therefore, analogue (current) mode is typically preferred at short ranges where signals are strong, whereas photon counting mode is preferred at longer ranges where the return becomes weak. In this approach, individual photon arrivals are recorded and accumulated over longer integration times that allows the detection of low intensity returns. Typical lidar receivers use photodetectors such as avalanche photodiodes (APDs) and photomultiplier tubes (PMTs), based on the choice of operating wavelength.

Understanding these instrumental characteristics such as the choice of acquisition mode, and the system geometry is crucial because they directly influence the signal to noise ratio, the minimum range of reliable measurements, and ultimately the accuracy of the received backscattered and extinction profiles (D'Amico et al., 2016). The subsequent sections discuss the mathematical representation of the lidar return signal for both elastic and inelastic scattering processes, along with the methods employed to get backscatter and extinction profiles.

2.4.1 The Elastic Lidar Equation

In eq. (2.10) the fundamental form of the elastic lidar equation is presented, which indicates the signal power received at the emission wavelength λ_0 from a distance R **(Wandinger, 2005)**:

$$P_{\lambda_0}(R) = KG(R)T_{\lambda_0}(R)\beta_{\lambda_0}(R) \tag{2.10}$$

Here K is a constant that includes all the parameters that are specific to the instrument, such as the pulse energy emitted by the laser source, the aperture area of the receiving telescope, and the effectiveness of the optical components. In this formulation, K also includes the transmitted pulse term P_0, which represents the laser emission and can be expressed in terms of the pulse energy E_0 (with $E_0 = P_0\tau$, where τ is the pulse duration).

The factor $G(R)$ denotes the range-dependent measurement geometry and can be expressed as**:**

$$G(R) = \frac{O(R)}{R^2} \tag{2.11}$$

where $O(R)$ is the overlap function. It quantifies the geometrical overlap between the laser beam and the receiver field of view at range R. This overlap is not complete at short distances because of the instrument geometric limitations, which reduces the fraction of backscattered photons collected by the receiver.

The lidar system design and setup are completely determined by the K and $G(R)$. At last, the transmission term $T_{\lambda_0}(R)$ and the total backscatter coefficient $\beta_{\lambda_0}(R)$ are the variables that describe the atmospheric contributions.

The amount of light that passes through the atmosphere, $T_{\lambda_0}(R)$, shows how much the laser beam attenuated as it travels to and from the scattering volume. This includes losses from both aerosol and molecular scattering and absorption. This term describes the two-way atmospheric transmission, and it can be expressed as:

$$T_{\lambda_0}(R) = \frac{I_{\lambda_0}(R)}{I_{\lambda_0}(0)} = exp\left[-2\int_0^R \alpha_{\lambda_0}(r)\ dr\right] \tag{2.12}$$

where $I_{\lambda_0}(R)$ is the received signal intensity at range R and $\alpha_{\lambda_0}(r)$ is the total extinction coefficient, which indicates how much the signal is attenuated by aerosol and molecular scattering and absorption at the emitted wavelength λ_0. Consequently, the sum of these four components defines the overall extinction coefficient:

$$\alpha_{\lambda_0}(R) = \alpha_{\lambda_0}^{aer}(R) + \alpha_{\lambda_0}^{mol}(R)$$

$$= \alpha_{\lambda_0}^{aer,sca}(R) + \alpha_{\lambda_0}^{aer,abs}(R) + \alpha_{\lambda_0}^{mol,sca}(R) + \alpha_{\lambda_0}^{mol,abs}(R) \qquad (2.13)$$

where "aer" and "mol" stand for "aerosols" and "molecules", and "abs" and "sca" stand for " absorption " and "scattering".

The last term in (Eq. 2.10), the backscatter coefficient $\beta_{\lambda_0}(R)$, indicates how much of the fraction of radiation is scattered back towards the lidar receiver. In a similar way to extinction, both aerosol and molecular contributions need to be taken into account, which results in:

$$\beta_{\lambda_0}(R) = \beta_{\lambda_0}^{aer}(R) + \beta_{\lambda_0}^{mol}(R) \qquad (2.14)$$

where $\beta_{\lambda_0}^{aer}(R)$ is the aerosol backscattered coefficient and $\beta_{\lambda_0}^{mol}(R)$ is the backscattered coefficient belonging to molecules.

By replacing all the parts, elastic lidar equation in its full form is written as:

$$P_{\lambda_0}(R) = K\,\frac{O(R)}{R^2}\left[\beta_{\lambda_0}^{aer}(R) + \beta_{\lambda_0}^{mol}(R)\right] exp\left[-2\int_0^R \left(\alpha_{\lambda_0}^{aer}(r) + \alpha_{\lambda_0}^{mol}(r)\right) dr\right] \qquad (2.15)$$

The term $P_{\lambda 0}(R)$ denotes the received power of backscattered signal at the wavelength λ_0 from range R. The elastic backscattered single-scattering lidar equation describes a system that transmits at a single wavelength and detects the portion of the return signal scattered at the same wavelength, corresponding to the process in which no energy exchange occurs between photons and the atmospheric constituents. Such type of system is commonly referred to as an elastic lidar.

The molecular (Rayleigh) components, β_{m} and α_{m}, can be estimated reliably from pressure and temperature profiles because molecular scattering is well characterised and is mainly governed by the number density of air molecules and known cross sections. The aerosol (particle) components, however, depend on particle concentration, size distribution, shape, and complex refractive index, all of which can vary in space and time. These microphysical properties are not measured directly by an elastic lidar; instead, they are expressed through their optical effects on the received signal, i.e. the aerosol backscatter and extinction terms. Consequently, in Eq. (2.15), both the aerosol extinction and the backscatter coefficients represent the unknown quantities that must be retrieved through specific inversion methods.

In the case of elastic lidar, the equation cannot be solved directly, and it requires inversion methods, which are discussed in the next section. On the other hand, Raman lidar provides an independent measurement channel at the inelastically scattered wavelength, yielding two equations with two unknowns. This allows a direct and lidar ratio assumption free retrieval of aerosol backscatter and extinction profiles.

2.4.2 The Klett Inversion Method

At a given wavelength λ_0, the elastic lidar equation provides one measured signal $P_{\lambda_0}(Z)$ but involves two unknown aerosol (particle) quantities: the aerosol extinction coefficient $\alpha_p(Z)$and the aerosol backscatter coefficient $\beta_p(Z)$ which is an undetermined problem in elastic lidar system. The Klett-Fernald (KF) algorithm addresses this by introducing two constraints (**Klett, 1981**; **Fernald, 1984**):

- A boundary condition at a reference height Z_{ref} (typically chosen in a region assumed to be aerosol-free or with negligible aerosol load), where the backscatter coefficient is known or assumed.
- The ratio of aerosol extinction to backscatter (typically called lidar ratio) $LR(Z) = \alpha_p(Z)/\beta_p(Z)$ must be known and constant.

In practice, the measured signal is first corrected for the geometric decrease with range by forming the RCS,

$$RCS(Z) = Z^2 P_{\lambda_0}(Z) \tag{2.16}$$

The KF inversion is applied in the height interval where the system overlap is complete (i.e., above the overlap region), so that the overlap function can be approximated as $O(Z) \approx 1$. The inversion is then performed from the reference height Z_{ref} downward to retrieve the particle backscatter profile $\beta_p(Z)$, and the corresponding particle extinction profile is obtained using

$$\alpha_p(Z) = LR(Z)\,\beta_p(Z) \tag{2.17}$$

The molecular extinction $\alpha_m(Z)$and molecular backscatter $\beta_m(Z)$ required in the inversion are estimated from pressure and temperature profiles (e.g., from radiosonde or model data) using Rayleigh theory. The reliability of the retrieved profiles mainly depends on the assumed lidar ratio and the choice of the reference height, because uncertainties in these inputs propagate through the inversion. This sensitivity is particularly important under strong atmospheric attenuation and when the selected reference region is not fully aerosol-free. Below the overlap height, the approximation $O(Z) \approx 1$ is no longer valid and an overlap correction must be applied before performing the inversion. Despite these limitations, the Klett-Fernald algorithm remains one of the most widely used approaches for elastic single-wavelength retrievals (including ceilometers) when independent extinction information from additional channels (e.g., Raman) is not available.

2.4.3 Raman Method

The Raman lidar technique is based on the simultaneous detection of the elastic backscatter at the emitted laser wavelength and the inelastic Raman shifted signal from the atmospheric molecules. The Raman shifted return provides an independent measurement of the atmospheric extinction, allowing aerosol backscatter and extinction profiles to be retrieved without assuming lidar ratio. In one commonly used approach, described by **(Ansmann et al. (1992b))**, the aerosol backscatter coefficient at the laser wavelength is derived by combining the elastic return with the corresponding nitrogen Raman signal. Other Raman lidar configurations may employ different molecular species or wavelength combinations depending on the instrument design and measurement objectives.

The Raman backscattered power signal $P(Z, \lambda_{Ra})$, is quantified at the Raman-shifted wavelength λ_{Ra}. The Raman lidar equation controls the strength of this signal, which comes from a scattering volume at altitude Z **(Ansmann & Müller, 2005)**:

$$P\,(Z,\,\lambda_{Ra}) = \frac{P_0 \eta_{\lambda_{Ra}}}{Z^2}\,O\,(Z,\,\lambda_{Ra})\,\beta_{Ra}\,(Z,\,\lambda_0)\;exp\left(-\int_0^Z [\alpha(z,\,\lambda_0) + \alpha(z,\,\lambda_{Ra})]dz\right) \tag{2.18}$$

where $\alpha(z,\ \lambda_0)$ is the range-dependent extinction coefficient at the emission wavelength λ_0, and it describes the one-way attenuation of the laser beam along the outgoing path from the lidar to the scattering volume. In Raman configuration, the detected photons are measured at the Raman-shifted wavelength λ_{Ra}, therefore $\alpha(z, \lambda_{Ra})$ is the extinction coefficient at λ_{Ra} , which represents the one-way attenuation of the Raman signal along its return path from the scattering volume towards the lidar. Under the single-scattering assumption, the detected photons at λ_{Ra} are those that were emitted at λ_0, Raman-shifted in the scattering volume, and then propagated back to the receiver at λ_{Ra}, so the exponential term in Eq. (2.18) represents the combined transmission losses along the outgoing path at $\lambda_0$and the return path at λ_{Ra}. In the case of rotational Raman scattering, the wavelength shift with respect to the laser wavelength is small, therefore λ_{Ra} can be approximated as equal to the λ_0.

To find the molecular Raman backscatter coefficient $\beta_{Ra}(Z, \lambda_0)$, both the molecular number density N_{Ra} and the differential Raman scattering cross section $\frac{d\sigma_{Ra}}{d\Omega}(\pi, \lambda_0)$ at the scattering angle π must be known, because β_{Ra} represents the amount of radiation scattered back toward the lidar per unit volume and solid angle, which depends on how many molecules are present and how efficiently they scatter light at the Raman shifted wavelength:

$$\beta_{Ra}(Z,\ \lambda_0) = N_{Ra}(Z)\ \frac{d\sigma_{Ra}}{d\Omega}(\pi,\ \lambda_0) \tag{2.19}$$

By substituting this expression (Eq. 2.19) into (Eq. 2.18), which represent the Raman lidar equation, and taking the natural logarithm of both sides, the derivative with respect to the range Z can be evaluated. The total extinction coefficient is, then, calculated by differentiating with respect to Z and rearranging the resulting expression. Now from this, the range corrected Raman signal is $S_{corr;\ Ra}(Z,\ \lambda_{Ra}) = Z^2 P(Z,\ \lambda_{Ra})$ **(Ansmann & Müller, 2005)**:

$$\alpha(Z,\ \lambda_0) + \alpha(Z,\ \lambda_{Ra}) = \frac{d}{dZ} ln \frac{N_{Ra}(Z)}{S_{corr,Ra}(Z,\lambda_{Ra})} + \frac{d}{dZ} ln\, O\,(Z,\ \lambda_{Ra}) \tag{2.20}$$

When the distance is large enough, the overlap function gets close to one. Consequently, the overlap term in (Eq. 2.20) can be disregarded, and the equation is expressed using the definition of the extinction coefficient $\alpha(Z) = \ \alpha_{par}(Z) + \alpha_{mol}(Z)$:

$$\alpha_{par}(Z,\ \lambda_0) + \alpha_{par}(Z,\ \lambda_{Ra}) = \frac{d}{dZ} ln \frac{N_{Ra}(Z)}{S_{corr,Ra}(Z,\lambda_{Ra})} - \alpha_{mol}(Z,\ \lambda_0) - \alpha_{mol}(Z,\ \lambda_{Ra}) \tag{2.21}$$

To describe how the particle extinction changes with wavelength, the Ångström exponent *Å(Z)* is defined:

$$\frac{\alpha_{par}(\lambda_0)}{\alpha_{par}(\lambda_{Ra})} = \left(\frac{\lambda_{Ra}}{\lambda_0}\right)^{\text{Å}} \tag{2.22}$$

Furthermore, at the emitted wavelength the extinction coefficient is obtained by taking into account *Å* **(Ansmann & Müller, 2005)**.

$$\alpha_{par}(Z,\ \lambda_0) = \frac{\frac{d}{dZ} ln\left(\frac{N_{Ra}(Z)}{S_{corr,Ra}(Z,\lambda_{Ra})}\right) - \alpha_{mol}(Z,\lambda_0) - \alpha_{mol}(Z,\lambda_{Ra})}{1+\left(\frac{\lambda_0}{\lambda_{Ra}}\right)^{\text{Å}}} \tag{2.23}$$

Therefore, from the measured elastic and Raman signals $P\,(Z, \lambda_0)$ and $P\,(Z, \lambda_{Ra})$, the particle backscatter coefficient $\beta_{par}\,(Z, \lambda_0)$ can be derived using the particle extinction coefficient $\alpha_{par}\,(Z, \lambda_0)$ **(Ansmann & Müller, 2005)**. For this purpose, the total (particle + molecular) elastic signals $P\,(Z, \lambda_0)$ and $P\,(Z_0, \lambda_0)$ are combined with the pure molecular Raman signals $P\,(Z, \lambda_{Ra})$ and $P\,(Z_0, \lambda_{Ra})$. By forming the ratio

$$\frac{P(R_0,\lambda_{Ra})\,P(R,\lambda_0)}{P(R_0,\lambda_0)\,P(R,\lambda_{Ra})} \tag{2.24}$$

and substituting the corresponding lidar equations for these four signals, the common instrumental and geometrical factors are cancelled. This procedure, together with the extinction term obtained from Eq. (2.23), directly leads to Eq. (2.25) for $\beta_{par}\,(Z, \lambda_0)$:

$$\beta_{par}(Z,\ \lambda_0) + \beta_{mol}(Z,\lambda_0) = [\beta_{par}(Z_0,\ \lambda_0) + \beta_{mol}(Z_0,\lambda_0)] \times \frac{P(Z_0,\ \lambda_{Ra})\,P(Z,\lambda_0)\,N_{Ra}(Z)}{P(Z_0,\lambda_0)\,P(Z,\lambda_{Ra})\,N_{Ra}(Z_0)}$$

$$\times \frac{exp\left(-\int_{Z_0}^{Z}[\alpha_{par}(z,\lambda_{Ra})+\alpha_{mol}(z,\lambda_{Ra})]\,dz\right)}{exp\left(-\int_{Z_0}^{Z}[\alpha_{par}(z,\lambda_0)+\alpha_{mol}(z,\lambda_0)]\,dz\right)} \tag{2.25}$$

However, it is important to note that detecting Raman signals during the daytime is hard because inelastic scattering is naturally weak and about three times (10^{-3}) less effective than elastic scattering. As a result, Raman lidar systems require detectors that are very sensitive, as high level of background solar radiation can make daytime measurements difficult. For this reason, Raman lidar observations are usually performed at night, when there is less background noise and the signal to noise ratio is better.

2.5 Doppler Wind Lidar for Atmospheric Studies

Besides aerosol lidars that are used for aerosol profiling, other lidar configurations are also available such as, Doppler Wind Lidar (DWL), High Spectral Resolution Lidar (HSRL), Differential Absorption Lidar (DIAL), and fluorescence lidar. Among them one important lidar is the (DWL), designed to study the speed and direction of the wind by monitoring changes in the backscattered signal frequency caused by the movement of air scatterers. This type of lidar is efficient for examining PBL dynamics, since they provide continuous vertical profiles of wind components inside and above the PBL. The upcoming sections provides a detailed discussion of the capabilities, operating principles, and data retrieval methodologies of DWL.

2.5.1 Physics of the Doppler Effect

Contrary to sound, light does not require a medium to propagate. As a result, the frequency shift that is detected in the optical Doppler effect is exclusively dependent on the relative motion that occurs along the line of sight. In case of light, it makes no difference which of them, either transmitter or the receiver is moving, the only thing that matters is their relative velocity along the line of sight. When a laser light is emitted with a frequency f_0 and a wavelength λ_0, and a particle moves with velocity v towards or away from the source, the shifted frequency observed by the particle is:

$$f = f_0\left(1 + \frac{v}{c}\right) \tag{2.26}$$

in which c represents the speed of light. Following that, the particle scatters the light backwards, and the frequency of the light that is received back at the lidar system is additionally doppler shifted as a result of the fact that it is moving while it is scattering:

$$f = f_0\left(1 + \frac{2v}{c}\right) \tag{2.27}$$

Motion towards the lidar, which is defined as a positive line-of-sight velocity, is indicated by a positive frequency shift, and motion away from the lidar is defined as a negative line-of-sight velocity.

In atmospheric measurements, the Doppler shift associated with the collective air motion (wind) is superimposed on the thermal, random motion of the scatterers. Air molecules normally move much faster than typical wind speeds, and their thermal speed increases with temperature. Consequently, the molecular backscatter is associated with a broad Doppler spectrum. Aerosol particles, because of their higher mass, move more slowly at the same temperature and, therefore, have a much narrower thermal velocity distribution. The wind shifts the aerosol and molecular components by the same amount, but relative to the much smaller aerosol spectral width, this shift is comparatively large and, therefore, more amenable to measurement **(Werner, 2005)**. In spectral terms, the situation can be viewed as a narrow aerosol peak superimposed on a broad molecular background, as schematically illustrated in Figure 2.5.

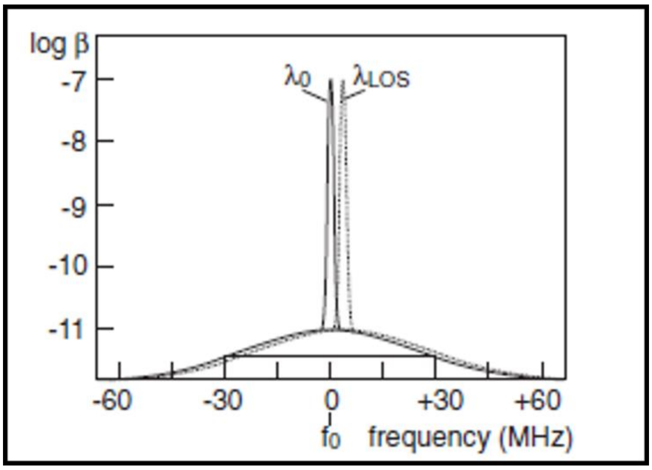

Figure 2.5. Schematic representation of the original (solid) and wind-shifted (dotted) frequency distributions. In the presence of aerosols, a narrow aerosol contribution is superimposed on the broad molecular spectrum; the shift toward higher frequencies corresponds to flow toward the lidar. Adopted from **(Werner, 2005)**.

2.5.2 Types of Doppler Lidar

Doppler wind lidar systems can be classified in different ways depending on the detection technique used to extract the Doppler frequency shift and on the laser emission mode used to obtain range information (pulsed or continuous wave). Based on how the Doppler frequency shift is extracted, Doppler lidar systems are commonly categorized into two types: coherent detection (also called heterodyne detection) and direct detection systems. In coherent lidar systems, the frequency shift is determined by comparing the return signal with a reference lidar signal, the working principle of which is explained in the next section, while in direct detection systems the signal is either filtered or resolved spectrally in order to extract the frequency shift.

In this thesis work, wind measurements that are used for the PBLH study were performed by a coherent Doppler wind lidar operating in pulsed mode. Coherent detection offers several advantages over direct detection for aerosol-assisted wind measurements in the PBL.

- It selectively collects only frequencies close to the reference making it extremely resistant to the background light (Liu et al., 2019).
- The uncertainty of its measurements is independent of temperature and the characteristics of the optical component in the system.
- A high receiver sensitivity enables wind measurements to be taken more quickly.

Independently of the detection scheme, Doppler wind lidars can also be classified as pulsed or continuous wave (CW) systems. Pulsed lidar, such as the system used in this work, are well suited for height-resolved wind profiling and long-range remote sensing (beyond 10 km), but they exhibit blind zones close to the transmitter, typically ranging from tens to hundreds of meters, depending on pulse duration and range-gate configuration.

Continuous wave (CW) lidar, on the other hand, do not have a blind region close to the source, but they suffer from poor range resolution at large distances. In CW systems, the range information is determined geometrically through the telescope focus rather than by pulse timing. As the detected distance increases, the depth of the sampled volume grows approximately with the square of the range, leading to increasing range uncertainty. For example, a CW lidar equipped with a 500 mm telescope has an uncertainty of about 2 m at a distance of 100 m, which increases to more than 200 m at a distance of 1000 m (Werner, 2005).

2.5.3 Working Principle and system architecture of Coherent Doppler Wind Lidar

Doppler Wind Lidar systems use the doppler frequency shift phenomenon in light backscattered by particles in the atmosphere to measure the part of wind speed that is projected along the direction of the laser beam. This is called the line-of-sight velocity or radial velocity (V_R). This shift in frequency happens due to the relative motion of particles and the laser light and is measured by the lidar system. Using the following relationship, the radial velocity can be calculated:

$$v_R = \frac{c}{2f_0} \Delta f \tag{2.28}$$

In this relation c is the speed of light, $f_0 = c/\lambda_0$ represents the emitted laser frequency and Δf is the Doppler shift observed in the backscattered signal.

To explain the general working principle of a coherent doppler lidar, a schematic diagram of the main optical and electronic components is shown in Figure 2.6. It depicts the processes of transmission, reception, and signal processing used to determine the radial wind velocity.

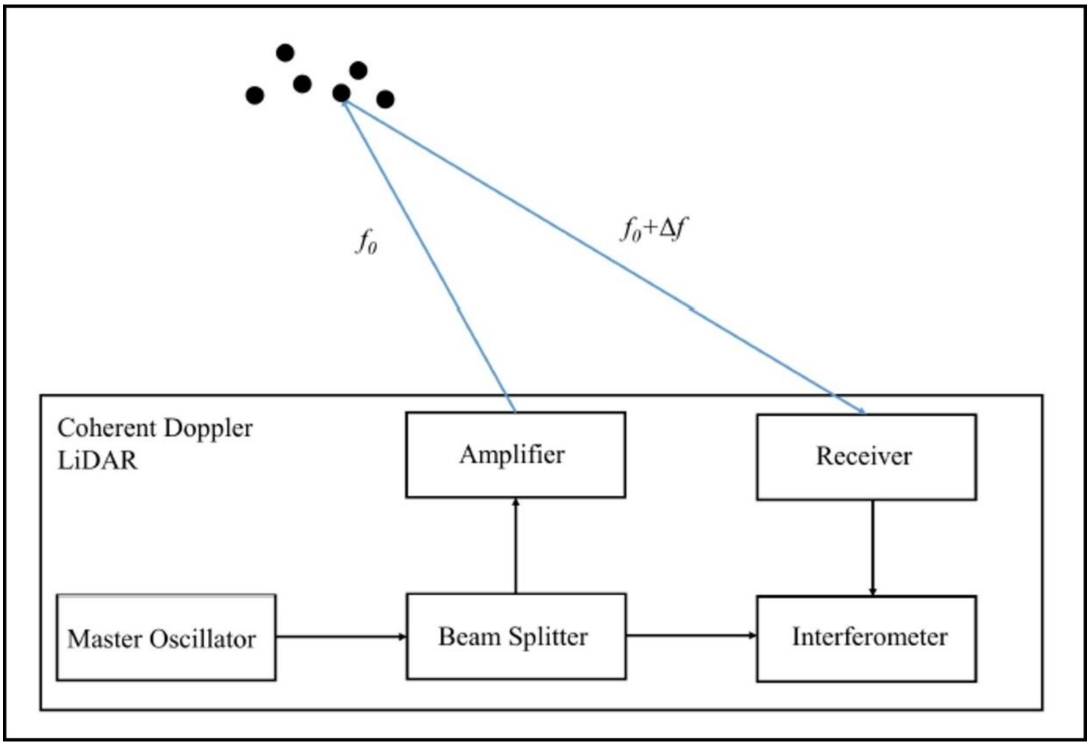

Figure 2.6. Schematic representation of a coherent lidar System **(Liu et al., 2019)**.

To understand this measurement, a coherent Doppler wind lidar system normally operates within the near-infrared spectral region, which is around (1.4-2.5 µm). This range guarantees a high level of atmospheric transmission and eye safety, as reported by **(Thobois et al., 2019)**. The lidar system has a master oscillator laser, which is responsible for emitting a pulse of light with a wavelength of λ_0. This output from the laser is separated into two different parts.

• The first component is introduced into an amplifier in order to accomplish the generation of the transmitted laser beam, which is then released into the atmosphere.

• The second component is the local oscillator, or reference beam, which in some systems may also come from a different laser.

A portion of the radiation that is transmitted is backscattered in the direction of the lidar receiver as a result of its interaction with moving particles in the atmosphere. Within an interferometer, this backscattered signal that undergoes a shift in frequency as a result of the Doppler effect ($f_0 + \Delta f$), is then coupled optically with the reference beam. This shifted frequency is then retrieved from the resulting combined optical field by using a detector. In the next step signal processing techniques, including the Fast Fourier Transform (FFT) and other spectrum methods, are then applied to accurately determine the value of Δf, which is then further utilised in the computation of the radial wind velocity **(Wang et al., 2018)**.

2.5.4 Measurement Uncertainty and Signal Quality in Doppler Wind Lidar

In Doppler Wind Lidar systems, the accuracy of radial velocity (v_R) estimates is affected by both instrument-related limitations and atmospheric conditions during the measurement. In coherent (heterodyne) systems, a dominant contribution to the measurement noise is often proportional to the local oscillator power (e.g., relative intensity noise), whereas noise sources independent of the local oscillator power are typically negligible **(Lindelöw, 2008)**. In addition, uncertainties can be introduced by errors in the sensing distance and in the elevation, angle used to project the measured Doppler shift onto v_R.

There are many environmental elements that contribute to the uncertainty of measurements. In flat terrain, turbulence causes random errors to be introduced, which are often quantified using the standard deviation. On the other hand, it has the potential to produce absolute as well as relative biases in complex terrain. The lidar system also captures backscatter from raindrops, which in turn contributes a significant negative bias into vertical velocity estimates **(Lindelöw-Marsden, 2009)**. The signal-to-noise ratio (SNR), which is defined as the ratio of mean signal power to noise power, is used to estimate the quality of measurements taken from the lidar. SNR is dependent not only on the design of the instrument but also on the atmospheric variability that exists inside the probe volume. It is observed that higher SNRs were frequently related with the higher wind speeds throughout long-term campaigns. When the signal-to-noise ratio (SNR) is low, the estimation of standard deviation (δ_e) of the Doppler velocity is possible by employing the formula reported by **(Pearson et al., 2009)**:

$$\delta_e = \left(\frac{4\sqrt{\pi}\Delta v_f^2}{\alpha N_p}(1 + 0.16\alpha)^2\right)^{1/2} \tag{2.29}$$

In this equation

. Δv_f belongs to spectral width of the signal

. The accumulated photon count is represented by $N_P = SNR\ M\ n$

. Number of points per range gate are represented by M

. Number of average pulses are expressed by n

. α is the ratio of photon to speckle count and is calculated by this equation,

$$\alpha = \frac{SNR}{(2\pi)^{1/2}(\Delta v_f / B)} \quad (2.30)$$

with B being the receiver bandwidth.

According to **(Pearson et al., 2009)** this approximation can be applied when the signal-to-noise ratio (SNR) is less than -5 decibels. On the other hand, **(O'Connor et al., 2010)** showed that when the SNR is greater than 0 decibels, the SNR impact on the standard deviation (δ_e) is trivial. The typical values for the spectral width Δv_f are 1.5 and 2.0 meters per second**.**

An SNR threshold is typically set in order to make sure of the data reliability. For example, Halo Photonics suggests a threshold of -18.2 dB for their Streamline system. However, experimental conditions that are under calm atmosphere allow thresholds as low as -20 dB, which results in a 40% increase in the amount of data that is available **(Päschke et al., 2015)**.

2.5.5 Scan Patterns

Doppler wind lidar measures radial velocity, and the vertical velocity component can be directly obtained by positioning the lidar at a 90° elevation angle. However, to reconstruct 2D or 3D wind fields, multiple radial velocity measurements from different beam orientations are required through various scan patterns, categorized by their degrees of freedom (DOF) **(Clifton et al., 2015)**.

Zero DOF (Vertical Staring Mode)

The laser beam is fixed in a single vertical direction in zero degrees of freedom scan mode. For measuring SNR, vertical wind, backscatter intensity, and mean wind variations, this mode is adequate. It's also used to identify regions of high turbulence in pre-tests.

One DOF

Plan Position Indicator (PPI), Arc Sector, and Range Height Indicator (RHI) scans are all examples of one degree of freedom scan mode. A concise description of these scan modes is explained in the subsequent sections.

PPI Scan

In PPI scan mode, the beam scans azimuthally (full 360° at constant elevation angle), and it is also known as velocity azimuth display (VAD). It is the most applied scan type in lidar experiments.

Arc Sector Scan

In Arc sector scan mode, the beam sweeps a partial azimuthal range at a constant elevation, offering a higher temporal resolution than PPI. This scan is particularly used in wind turbine wake studies in which only the downstream region is of interest.

RHI Scan

RHI Scan is a type of scan that is widely employed in dual or multi-lidar configurations. This scan involves the laser scanning vertically across a slice while keeping the azimuth angle constant throughout the process. This type of scan validates three-dimensional flow fields based on two-dimensional data that is an essential part of the process of analysing vertical flow structures, such as the wakes of aeroplanes or turbines.

Two DOF (Doppler Beam Swinging (DBS Mode))

The DBS Scan consist of a vertical scan in addition to a few radial measurements taken at various azimuth angles. DBS is fast and hardware-efficient but limited in its ability to assess measurement reliability. The minimum setup requires three orthogonal scans (vertical, north-tilted, and east-tilted), while a six-beam DBS scheme that includes (five tilted + one vertical) is proposed by **(Sathe et al., 2015)** to calculate the Reynolds stress tensor.

Composite Scans

There is also the possibility of forming two-degree-of-freedom patterns by the sequential combination of various scan types such as staring, PPI, DBS, and RHI.

For the PBL study, the most commonly employed scan modes are: the vertical staring mode, the PPI scan mode, and the DBS scan mode.

2.5.6 Wind field Retrieval Methods

Due to the fact that a single Doppler lidar can only measure the radial velocity V_R along the direction of the laser beam, extra processing is required in order to retrieve the full wind vector components. This includes either the horizontal components u(east-west) and v(north-south) or all three components u, v, and w (vertical). The VAD method is an extensively used approach for this purpose, and linear least-squares regression is the basis on which the method relies (Gao et al., 2004). In this thesis work, the focus is on the retrieval of wind components using the VAD method, which is further explained in the next section.

Along with the VAD method, other strategies are also used for wind field retrieval, including Volume Velocity Processing (VVP), Optimal Interpolation (OI), and variational methods. The VVP method utilises basis functions that are connected to wind velocities as well as their gradients (Koscielny et al., 1982). In practice, careful examination of the distribution and number of radial-velocity points is generally required to ensure the validity of the underlying linear assumptions.

Some alternative methods have been developed to address the peculiarities of nonlinear wind fields. Optimal interpolation is a statistical method that makes use of covariance functions in order to maintain the characteristics of the local wind field (Xu & Gong, 2003). Due to its horizontal-plane assumptions, it is often usable only for low elevation angles. Variational wind retrieval methods estimate the wind components by minimising a cost function (Cherukuru et al., 2017). However, physically based variational approaches are computationally expensive compared to other methods.

Among the approaches mentioned above, this work focuses on the VAD technique; therefore, the following section provides a detailed description of the VAD methodology and its theoretical framework.

2.5.7 Theoretical Framework of VAD Method

Assuming that the wind field is horizontally homogenous, the fundamental concept behind the VAD is to fit the measured wind velocity at a particular elevation angle to a sinusoidal curve (Gao et al., 2004). This is done in order to determine the wind speed at a given elevation angle. Given the assumption that the velocity vector changes linearly around the centre of the circle that is being scanned, the first order Taylor approximation of three velocity components (u, v, and w) may be expressed as follows,

$$u = u_0 + \frac{\partial u}{\partial x}x + \frac{\partial u}{\partial y}y + \frac{\partial u}{\partial z}z$$

$$v = v_0 + \frac{\partial v}{\partial x}x + \frac{\partial v}{\partial y}y + \frac{\partial v}{\partial z}z,$$

$$w = w_0 + \frac{\partial w}{\partial x}x + \frac{\partial w}{\partial y}y + \frac{\partial w}{\partial z}z \tag{2.31}$$

where the velocity components u_o, v_o, and w_o are located in the centre of the circle that is being scanned by lidar systems. The Cartesian coordinates *(x, y, z)* is converted to the spherical coordinates (r, θ, φ) by

$$x = r\cos\phi\sin\theta,$$

$$y = r\cos\phi\cos\theta,$$

$$z = r\sin\phi. \tag{2.32}$$

Here r denotes the radial distance from the LiDAR, ϕ is the elevation angle and θ is the azimuthal angle. The radial velocity V_R is expressed as:

$$v_R = u\sin\theta\cos\phi + v\cos\theta\cos\phi + w\sin\phi. \tag{2.33}$$

Substituting (Eq. 2.31) and (Eq. 2.32) into (Eq. 2.33), v_R is written as:

$$\mathrm{v_R} = \mathrm{u_0}\sin\theta\cos\phi + \mathrm{v_0}\cos\theta\cos\phi + \mathrm{r}\cos^2\phi\cos\theta\sin\theta\left(\frac{\partial \mathrm{u}}{\partial \mathrm{y}} + \frac{\partial \mathrm{v}}{\partial \mathrm{x}}\right)$$

$$+ \mathrm{r}\cos^2\phi\sin^2\theta\frac{\partial \mathrm{u}}{\partial \mathrm{x}} + \mathrm{r}\cos^2\phi\cos^2\theta\frac{\partial \mathrm{v}}{\partial \mathrm{y}} + \mathrm{r}\sin\phi\cos\phi\sin\theta\frac{\partial \mathrm{u}}{\partial \mathrm{z}} + \mathrm{r}\sin\phi\cos\phi\cos\theta\frac{\partial \mathrm{v}}{\partial \mathrm{z}}$$

$$+ \mathrm{w_0}\sin\phi + \mathrm{r}\cos\phi\sin\phi\sin\theta\frac{\partial \mathrm{w}}{\partial \mathrm{x}} + \mathrm{r}\cos\phi\sin\phi\cos\theta\frac{\partial \mathrm{w}}{\partial \mathrm{y}} + \mathrm{r}\sin^2\phi\frac{\partial \mathrm{w}}{\partial \mathrm{z}} \tag{2.34}$$

The Fourier series in θ is obtained by disregarding the vertical derivatives, which are denoted as $\partial u/\partial z$ and $\partial v/\partial z$, as well as the derivatives of w in (Eq. 2.34):

$$v_R = a_0 + \sum_{n=1}^{2}(a_n\sin n\,\theta + b_n\cos n\,\theta) \tag{2.35}$$

with coefficients:

$$a_0 = \frac{1}{2} r \cos^2 \phi \left(\frac{\partial u}{\partial x} + \frac{\partial v}{\partial y}\right) + w_0 \sin \phi,$$

$$a_1 = u_0 \cos \phi,$$

$$b_1 = v_0 \cos \phi,$$

$$a_2 = \frac{1}{2} r \cos^2 \phi \left(\frac{\partial u}{\partial y} + \frac{\partial v}{\partial x}\right),$$

$$b_2 = \frac{1}{2} r \cos^2 \phi \left(\frac{\partial v}{\partial y} - \frac{\partial u}{\partial x}\right). \tag{2.36}$$

(Eq. 2.34) is transformed into the following when n radial velocity measurements (v_R^i, $i = 1, 2, \dots, n$) are acquired.

$$v_R^i = PK + \epsilon^i \tag{2.37}$$

where $K^T = [a_0, a_1, b_1, a_2, b_2]$ is the combination of Fourier coefficients, e^i is the model error, and $P = [1, \sin\theta, \cos\theta, \sin 2\theta, \cos 2\theta]$ is the parameter vector made up of basis functions. Then, K, which is connected to the wind field's kinematic data and velocity components, may be estimated using a linear least squares regression. The first harmonics in (Eq. 2.35) may be used to compute V_R if the flow is considered to be uniform.

2.6 Ceilometer Lidar for atmospheric study

Ceilometers are a type of elastic lidar that normally operate at a single wavelength in the near infrared spectral range (typically between 900 and 1100 nm). This range is chosen to achieve the goal of minimizing the effects of Rayleigh scattering. A distinguishing feature of these systems is their high pulse repetition rates, typically on the order of a few kilohertz (Wiegner et al., 2014). Additionally, in order to maintain eye-safe conditions, these systems operate at low pulse energies. The design of the instrument often allows for a temporal resolution of more than one minute and a vertical resolution of about 15 meters, while the maximum usable detection range depends on the instrument model and atmospheric conditions and can reach values up to ~15 km

Ceilometer configurations mainly differ in the transmitter-receiver optical arrangement, which can be monoaxial (transmit and receive paths share the same optical axis) or biaxial (separate transmit and receive paths). In ceilometer observations, overlap effects at low altitudes can introduce significant uncertainties and, therefore, affect the capability to retrieve near-range aerosol and boundary-layer structures. The achievable measurement range and signal sensitivity depend on instrumental parameters such as emitted pulse energy, receiver field of view, and the overall optical design **(Wiegner et al., 2014)**.

Although ceilometers were originally developed for cloud-base height and visibility detection, they are increasingly used for scientific applications, especially for aerosol layering and PBL studies. In this context, the use of ceilometer observations for aerosol-related products requires careful instrumental characterisation and calibration, since quantitative backscatter retrievals are sensitive to instrument constants and to overlap effects and related corrections **(Wiegner et al., 2014)**.

2.6.1 Aerosol Properties from Ceilometers

The retrieval of aerosol properties from ceilometers follows the same fundamental principles as those described for elastic lidars in Section (2.4.1), being governed by the elastic lidar equation. The total backscatter and extinction coefficients are composed of molecular and particulate contributions:

$$\beta = \beta_p + \beta_m \tag{2.38}$$

$$\alpha = \alpha_p + \alpha_m \tag{2.39}$$

However, because ceilometers operate at a single wavelength and lack Raman or depolarization channels, only the particle backscatter coefficient $\beta_p(z)$ can be reliably retrieved. Extinction $\alpha_p(z)$ and optical depth τ_p cannot be obtained directly. Therefore, ceilometers are primarily used to determine the PBL height, derived from the vertical structure of $\beta_p(z)$.

2.6.2 Retrieval Methods and Calibration

To retrieve the particle backscatter coefficient $\beta_p(z)$ from ceilometer signals, inversion algorithms such as the **(Klett, 1981; Fernald, 1984)** methods are typically applied. In practice, these solutions require assumptions about the lidar ratio and a boundary condition at a reference altitude. Since Raman scattering cannot be detected at ceilometer wavelengths, the lidar ratio must be estimated through modelling or auxiliary observations.

The main limitation of ceilometers lies in their calibration accuracy, that strongly affects the reliability of $\beta_p(z)$ retrievals. Rayleigh calibration is often applied, assuming aerosol-free conditions at high altitudes, but this requires sufficient signal-to-noise ratio, which is not always available. Consequently, alternative strategies are used, such as comparisons with co-located Raman lidars, sun photometers, or exploiting attenuated backscatter profiles inside stratocumulus cloud **(O'Connor et al., 2004)**.

2.6.3 Operational Applications

Despite the limitations discussed in Section 2.6.2, mainly those affecting quantitative aerosol retrievals (calibration, overlap effects, and the need for assumptions such as lidar ratio), ceilometers play an important role in operational atmospheric monitoring networks because they provide continuous and fully automatic measurements. Their deployment in networks and their high temporal sampling make them particularly valuable for near-real-time products such as cloud-base height and for tracking aerosol layering and boundary-layer structure, including estimates of mixing-layer height.

In operational frameworks and networks (e.g., E-PROFILE and ACTRIS-related activities), ongoing efforts focus on harmonising processing and improving the consistency of derived products, including $\beta_p(z)$where calibration requirements can be met. Within the EARLINET context, these developments support the combined use of ceilometers together with advanced lidar observations (e.g., Raman/HSRL) for aerosol and boundary-layer monitoring **(Wiegner et al., 2014)**.

Chapter.3

Site, Instruments, PBLH Retrieval Methods, and Case Studies

As discussed in detail in the second chapter about the theoretical foundation and the instrumental characteristics of different lidars, which include aerosol lidar, ceilometer, and wind Doppler lidar, along with the integration of these instruments into atmospheric monitoring networks such as ACTRIS, Earlinet, Cloudnet, and Alicenet. These networks provide high-quality, standardized datasets that are used for boundary layer research. The initial part of the third chapter, instead, provides an overview of the ACTRIS Potenza station considered in this chapter, together with the main specifications of the active remote sensing instruments operated at this site. The following sections then focus on the practical implementation of various methods used to retrieve the (PBLH) from aerosol lidar, ceilometer, and wind Doppler lidar datasets. For the aerosol lidar dataset, the gradient-based methods, which include first-order gradient (GM), second-order gradient (IPM), logarithm gradient (LGM), and cubic root gradient (CRGM) methods, as well as the wavelet covariance transform (WCT) method, has been applied. In the case of ceilometer lidar data, the error function fit (ERF-FIT) method is applied. For the wind Doppler lidar data, the vertical velocity variance and wind shear methods are applied, additionally, wind speed and direction are calculated in order to support the results obtained from these methods. This chapter provides a detailed description of these methods and assesses their performance by applying them to the afore mentioned datasets. Consequently, it serves as a bridge between the theoretical concepts and operational application. The results are presented in the form of comparative plots and observational analysis highlighting the strengths and limitations of each retrieval algorithm.

3.1 Experimental Sites and Instruments

In this study, observational data from two ACTRIS stations were analysed to investigate the PBLH: the Potenza and the Lampedusa sites. The analysis focuses on the Potenza station, where an aerosol lidar, a ceilometer, and a wind doppler lidar are available. This suite of instruments enables a comprehensive study of the seasonal behaviour of PBL dynamics through complementary measurement approaches. In the following subsections, an overview of the specifications of the active remote sensing instruments used at both sites, the datasets of which are employed for the analysis of PBL dynamics, is presented.

3.1.1 Aerosol Lidar Systems

For this study, data acquired from the Multi-wavelength System for Aerosol (MUSA) and fixed Raymetrics lidar were used, as shown in the Figure 3.1A and Figure 3.1B. These two lidar systems are operated at the Potenza station (760 m a.s.l.), the historical CNR hotspot for atmospheric studies located in south Italy (40.60°N, 15.72°E) and recognized as a National Facility within the ACTRIS network. MUSA and fixed Raymetrics are both elastic-Raman lidar systems, operated in the 3β+2α configuration for MUSA and 3β+3α configuration for the fixed Raymetrics instrument, with the possibility of performing depolarization ratio measurements. This configuration enables state-of-art classification of atmospheric aerosol in terms of optical and microphysical properties. The temporal and vertical resolution of the raw profile from both MUSA and fixed Raymetrics lidar are 60 s and 3.75 m, respectively.

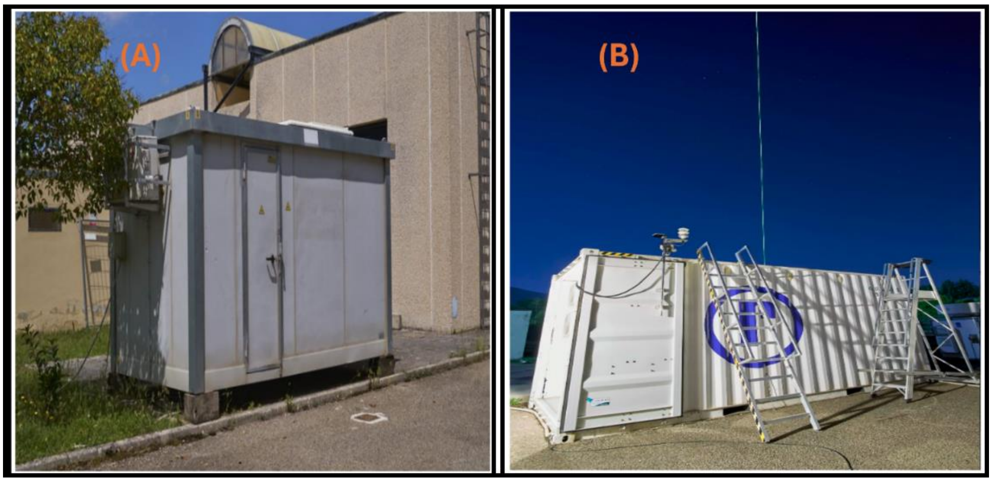

Figure 3.1. Aerosol lidar systems used in this study: (A) MUSA and (B) fixed Raymetrics operated at the CNR-IMAA Potenza station, and all systems are part of the ACTRIS/EARLINET networks and operate in multi-wavelength elastic-Raman configurations **(CIAO-CNR-IMAA Atmospheric Observatory, 2024).**

3.1.2 Ceilometer Lidar System

Along with the Aerosol lidar systems, the ACTRIS Potenza station is equipped with a Vaisala CL51 ceilometer, a single wavelength lidar designed for continuous and long-term monitoring of cloud base height and vertical aerosol backscatter profiles, as shown in Figure 3.2. The Vaisala CL51 operates at an eye safe wavelength of 905 nm and provides measurements with a temporal resolution of 10 s. The CL 51 produces hourly averaged backscatter profiles with a vertical resolution of 10 m, covering altitudes from the surface up to 15,000 m. This instrument offers reliable performance under a wide range atmospheric conditions, making it particularly suitable for continuous PBLH detection and long-term climatological analysis.

Figure 3.2. Vaisala CL51 ceilometer installed at the ACTRIS Potenza station (CNR-IMAA) **(CIAO - CNR-IMAA Atmospheric Observatory, 2024).**

3.1.3 Wind Doppler Lidar System

ACTRIS Potenza station is also equipped with wind doppler lidar (HALO photonics 120) as shown in Figure 3.3. This system operates at the wavelength of (1.5 µm) and provides high frequency wind measurements with a spatial resolution of 30 m and a temporal resolution of 1s. The (Halo 120) Doppler lidar can operates in various scanning modes, including vertical stare, PPI, and DBS mode, which enables the retrieval of the wind components (horizontal and vertical) with high accuracy. This configuration enables detailed investigation of the vertical structure of the atmosphere and the turbulent characteristics of the PBL.

Figure 3.3. HALO Photonics 120 Doppler wind lidar installed at the ACTRIS Potenza station (CNR-IMAA) (CIAO-CNR-IMAA Atmospheric Observatory, 2024).

3.2 Methodologies of PBLH retrieval From Aerosol Lidar Data

As discussed in the 2nd chapter, the lidar technique employs laser light pulses to probe the atmosphere with high temporal and vertical resolution by collecting and detecting the portion of light that is backscattered by atmospheric molecules and aerosols. However, raw lidar signals are not directly exploitable and require correction for a range of instrumental factors including background noise, detector dead time, after pulsing, incomplete overlap between the laser beam and receiver field of view, and fluctuations in pulse energy (Campbell et al., 2002). After these corrections, the analysis is performed on the RCS as defined in the chapter 2. In this chapter the RCS profiles are analysed using a set of retrieval methods, including gradient-based approaches and wavelet covariance transforms method, to estimate the PBLH.

These methods are mostly based on two key assumptions. First, the PBL is more polluted than the upper free atmosphere (FT) above it, the aerosol concentration difference between PBL and FT results in a strong negative gradient of lidar backscatter signal (Münkel et al., 2007). Second, at the top of well-mixed boundary layer, the entrainment process incorporates cleaner air masses from FT into boundary layer. This leads to localized and significant fluctuations in aerosol concentration which observed as significant temporal variations in the lidar signal (Hooper & Eloranta, 1986).

In the following sections, the retrieval approaches used in this study are described in detail. The gradient-based methods (GM, IPM, LGM, CRGM) and the wavelet covariance transform are illustrated, including the details of their implementation.

3.2.1 Gradient Methods

Gradient-based methods are applied to retrieve the PBLH from aerosol lidar data. These methods assume that the atmospheric particles are trapped within the PBL. Consequently, the lidar signal is strongly backscattered within the PBL, due to the high aerosol's concentration. As the signal moves from the PBL to the free troposphere, where the aerosol concentration quickly decreases, a clear drop in the backscattered intensity appears. In the gradient method, this rapid decrease in the backscattered intensity manifests as a pronounced negative gradient in the derivative of the RCS (Dang et al., 2019). The PBLH is thus identified as the altitude corresponding to this negative peak. The theoretical and mathematical framework of these gradient-based methods is present below.

First Order Gradient Method (GM)

In GM, the first order derivative of the RCS profile is taken with respect to the altitude, and the PBLH is defined as the altitude point where the strongest negative gradient appears in the first order derivative of the RCS profile (Hayden et al., 1997). The mathematical expression of GM is given in Eq. (3.1).

$$H_{\mathrm{GM}} = H_{min}\left(\frac{d(\mathrm{RCS})}{dz}\right) \quad (3.1)$$

Second Order Gradient Method (IPM)

In Second order gradient method, also known as the inflection point method (IPM), the second order derivative of RCS profile is taken with respect to the altitude, and the PBLH is defined as the altitude point where the absolute minimum occurs in the second order derivative of the RCS profile (Menut et al., 1999 ; Dang et al., 2019). The mathematical expression of IPM is given in Eq. (3.2).

$$H_{\mathrm{IPM}} = H_{min}\left(\frac{\mathrm{d}^2(\mathrm{RCS})}{\mathrm{d}z^2}\right) \quad (3.2)$$

Logarithmic Gradient Method (LGM)

LGM involves calculating the derivative of the natural logarithm of the RCS profile with respect to altitude. This transformation helps to lower the influence of noise and fluctuation in the RCS profile. The PBLH is then identified as the altitude point at which the absolute minimum occurs in the derivative of logarithm transformed RCS profile (Martucci et al., 2007). The mathematical expression of LGM is given in Eq. (3.3).

$$H_{\mathrm{LGM}} = H_{min}\left(\frac{\mathrm{d}\ln(\mathrm{RCS})}{\mathrm{d}z}\right) \tag{3.3}$$

Cubic Root Gradient Method (CRGM)

In CRGM, the cubic root of the RCS profile is computed before taking the derivative with respect to altitude. This transformation accounts for the influence of the gravity waves on the vertical aerosol distribution. The PBLH is defined as the altitude point corresponding to the minimum of the cubic root gradient of RCS profile (Ji et al., 2019). The mathematical expression of LGM is given in Eq. (3.4).

$$H_{\mathrm{CRGM}} = H_{min}\left(\frac{\mathrm{d}(\mathrm{RCS})^{1/3}}{\mathrm{d}z}\right) \tag{3.4}$$

3.2.2 Wavelet covariance transform method (WCT)

WCT method is also a gradient based algorithm used for the retrieval of PBLH by identifying the sharp variations in the RCS, typically corresponding to aerosol concentration discontinuities. This method was first introduced by (Mallat & Hwang, 2002) for the general signal analysis and later adapted for the PBLH studies using lidar observations (Dang et al., 2019). The technique retrieves the PBLH by quantifying the similarity between the measured backscattered profile and the wavelet function, expressed through a covariance transform. In practical applications to aerosol lidar data for PBL studies, the Haar wavelet function is most commonly used because the shape of this function is quite similar to the step like transition that is often observed in the RCS across the boundary layer top.

Mathematically, the Haar wavelet function and the covariance transform are defined in Eq. (3.5) and Eq. (3.6).

$$h\left(\frac{z-b}{a}\right) = \begin{cases} +1: & b-\frac{a}{2} \leq z \leq b \\ -1: & b \leq z \leq z+\frac{a}{2} \\ 0: & elsewhere \end{cases} \tag{3.5}$$

$$w_f(a,b) = \frac{1}{a}\int_{z_t}^{z_b} X(z)\ h\left(\frac{z-b}{a}\right) dz \tag{3.6}$$

Where h is the Haar wavelet function, z is the altitude, b and a are the translation and dilation of the wavelet function that adjust its shape and location, whereas w_f represent the covariance transform, $X(z)$ is the range corrected signal, z_b and z_t denote the bottom and top altitudes in the RCS profile (Dang et al., 2019).

The maximum value of $w_f(a,b)$ corresponds to the height of the most abrupt change in the lidar signal, i.e., where the RCS profile and the Haar function show greatest similarity, thus identifying the PBLH. Before applying the WCT method to the RCS profile, the initial conditions a(dilation) and b(translation) must be defined. The dilation parameter a sets the vertical range over which the algorithm searches for abrupt changes in the RCS profile, while the translation parameter b defines the wavelet centre in height. By scanning b across the altitude range, the Haar function is shifted vertically through the RCS profile and the altitude maximizing the covariance between them, is identified as PBLH. The selection of a and b parameters is crucial for the reliable detection of the PBLH, as these parameters determine the position and scale of the wavelet function applied to RCS profile. Therefore, they have a significant influence on how effectively the WCT algorithm identifies the main discontinuity associated with the PBL top.

3.3 Methodologies for Ceilometer Lidar Data

As discussed in the second chapter, the Ceilometer is a compact, single wavelength elastic lidar designed mainly for the continuous and unattenuated operations, making them suitable for long term monitoring of aerosol distribution and boundary layer dynamics. Various retrieval approaches, including gradient method, wavelet covariance transform method, error function fit method, are commonly used for deriving the PBLH from the backscattered profile measured by the ceilometer lidar. In this study, the backscattered profile is analysed using error function fit (ERF-fit) method proposed by (Steyn et al, 1999), to estimate the PBLH.

3.3.1 ERF fit method

The ERF approach is based on the fitting an idealised backscattered profile, denoted by B(z), to the backscatter profile retrieved by the lidar measurements, b(z). The mathematical representation of the idealised profile B(z) is given in Eq. (3.7).

$$B(z) = \frac{(B_m + B_u)}{2} - \frac{(B_m - B_u)}{2} \operatorname{erf}\left(\frac{z - z_m}{s}\right) \tag{3.7}$$

In this equation, B_u represent the mean backscatter coefficient above the entrainment layer, B_m is the mean backscatter coefficient within the mixed layer, z_m is the mixed layer depth that is also reported as PBLH, and s is the parameter related to the entertainment zone thickness, describing the sharpness of the transition between the mixed layer and the overlying air. Larger value of s indicates a more gradual transition, while a smaller value of s represents a sharper transition. These four parameters of the idealized backscatter profile are estimated by minimizing the root mean square deviation (RMSD) between the observed backscatter b(z) and the idealized backscatter B(z). This method is considered more robust because it utilises the whole backscatter profile, rather than focusing only on the part of the profile surrounding the top of the mixed layer, to retrieve the mixed-layer depth. This mixed-layer depth is commonly used as a proxy for the PBL height in aerosol backscatter-based retrievals, since in these approaches the PBL top is often identified as the height where aerosol particles are well mixed below and a marked decrease in backscatter occurs above (Dang et al., 2019).

3.4 Methodologies for Wind Doppler lidar Data

As discussed in the Chapter 2, the wind doppler lidar provides high resolution wind information by measuring the doppler shift in the frequency of the backscattered light caused by the motion of aerosol and air particles along the line of sight. The doppler lidar system thus provides the radial velocity components that are subsequently analysed for the PBLH retrieval.

In this study the data from the wind doppler lidar (HALO photonics 120) were used. This system provides high-frequency data with spatial resolution of 30 m and a temporal resolution of a few seconds. Two different scanning strategies were employed in this analysis, that includes the vertical stare mode and the Doppler Beam Swinging (DBS) mode, that were discussed in detail in Chapter 2. To estimate PBLH, two different methods, vertical velocity variance approach, and wind shear method were applied based on the scan type.

3.4.1 Vertical Velocity Variance method:

The velocity variance method is based on the turbulent character of the atmospheric boundary layer. Within the well mixed layer, strong convective and mechanical turbulence generates large fluctuations in the vertical velocity, in contrast turbulence rapidly decreases above the boundary layer in the stable free troposphere. The transition between these two regions is, therefore, identifiable through the profile of vertical velocity variance (σ_w^2) **(Barlow et al., 2011)**.

In this method, the vertical wind velocity data from the vertical staring mode are first temporally averaged and then σ_w^2 is calculated at each altitude level by using the variance expression shown in Eq. (3.8).

$$\sigma_w^2 = \frac{1}{N-1}\sum_{i=1}^{N}(w_i - \overline{w})^2 \tag{3.8}$$

where w_i is the instantaneous vertical velocity measured by the Doppler lidar at each altitude level and $\overline{w}$ is the mean vertical velocity at that altitude. In this method, the PBL top is defined as the altitude at which vertical variance (σ_w^2) fell below a certain threshold value, that identify the upper boundary of turbulent mixing. Normally, the σ_w^2 profiles show maximum values close to the surface because thermal convection and mechanical turbulence dominate and decreases steadily with height as turbulence weakens. The altitude level at which this variance sharply decreases below a particular threshold value is identifies as the top of the PBL **(Huang et al., 2017)**.

3.4.2 Wind shear method

The wind shear method based on the increase of horizontal wind speed above the mixed layer. In the PBL, turbulent mixing ensures a largely uniform wind profile, however above the mixed layer wind speed generally increases rapidly with height, due to decreased frictional effect.

Therefore, the upper limit of the boundary layer is defined as the altitude of maximum wind shear in the horizontal wind speed (Ortiz-Amezcua et al., 2022).

For this purpose, the derived horizontal wind components from the DBS scan data are used to compute the total horizontal wind speed and to locate the height where the vertical shear of horizontal wind reaches a maximum. For a layer of thickness Δz, the vertical wind shear $\Delta V/\Delta z$ is calculated by using the Eq. (3.9).

$$\frac{\Delta V}{\Delta z} = \frac{\sqrt{(u_t - u_b)^2 + (v_t - v_b)^2}}{(z_t - z_b)} \tag{3.9}$$

This method is specifically useful during the periods of strong convective development or when vertical stare data are not available. The estimate of PBLH based on the wind shear method provides an independent confirmation of the boundary layer height retrieved from the vertical velocity variance method, as both methods identify the transition between the turbulent boundary layer and the more stable free troposphere from different dynamical prospectives.

3.4.3 Wind Speed and direction

The estimation of wind speed and direction from doppler lidar measurements is based on the analysis of horizontal components of wind velocity (Ortiz-Amezcua et al., 2022). As in the DBS scanning configuration, the lidar records the radial velocity at several azimuth angles, so the radial velocity data obtained from this scan are combined to derive the horizontal wind components (u and v) and to compute the magnitude of wind speed and wind direction by using Eq. (3.10) and Eq. (3.11).

$$V = \sqrt{u^2 + v^2} \tag{3.10}$$

$$\gamma = atan2^{-1}\,\frac{u}{v} \tag{3.11}$$

Wind speed and wind direction provide meaningful insights into the structure and dynamics of atmospheric flow. Variations in wind speed with altitude signify the intensity of the shear layer, while gradual or sudden shifts in the wind direction reflect alterations in the air mass or the prevailing flow regime. Such changes are frequently associated with the extensive weather systems or localized circulations that affect the evolution of boundary layer.

In this study, the wind speed and direction profiles derived from the DBS scan data are used to complement the PBLH estimates obtained from the wind shear method. The temporal changes in these wind characteristics helps to evaluate the boundary layer during the day, particularly under the strong surface heating conditions. The agreement between the wind profiles and the PBLH derived from other approaches make sure a consistent and physically reliable interpretation of the boundary layer dynamics.

3.5 Implementation of Algorithms

The retrieval algorithms described in the previous sections were implemented to process the datasets acquired from the aerosol lidar, the ceilometer, and the wind doppler lidar. Each algorithm was designed to identify the PBLH from its corresponding signal type by following a sequence of data selection and boundary detection steps. The implementation of these algorithms was carried out individually for each dataset, according to each instrument's measurement configuration and signal characteristics. The resulting PBLH estimates obtained from these algorithms are further analysed in the following sections to evaluate their diurnal evolution and seasonal behaviour.

3.5.1 Algorithm for Aerosol Lidar Data

As previously discussed, the aerosol-lidar dataset was processed using the gradient-based methods (GM, IPM, LGM, CRGM) and the WCT. For the ACTRIS Potenza station, Lidar signal profiles were downloaded from the EARLINET database. These signal profiles are provided at 60-m vertical resolution and various temporal aggregations (30 min, 1 h, 2 h, …).

Days were selected based on continuous lidar coverage across a large fraction of the diurnal cycle in order to get better knowledge about boundary-layer evolution. To reduce the impact of Saharan dust and cloud cover on the backscatter profiles, dust-affected days were identified using the DREAM8 and multi-model forecasts **(WMO Barcelona Dust Regional Centre, n.d.)**, while cloudy days were identified using cloud-cover information from the European Organisation for the Exploitation of Meteorological Satellites (EUMETSAT) **(EUMETSAT, n.d.)**. After this screening, only the remaining days were used for the retrieval and for constructing the daily PBLH evolution.

The implementation steps, summarized in the flowchart in Figure 3.4 are as follows. RCS profiles for each time of selected days are prepared in an Excel format to facilitate analysis.

For each profile, the gradient methods are applied directly to the RCS: GM uses the first derivative of this signal while IPM uses the second derivative, the LGM applies the derivative to $\ln(\mathrm{RCS})$, and CRGM applies the derivative to $(\mathrm{RCS})^{1/3}$. In each case, the PBLH is defined as the altitude at which the corresponding derivative reaches its minimum value. In parallel, the WCT is applied by correlating the RCS with the Haar wavelet function the altitude of the maximum covariance is identified as the PBLH for that profile. Repeating this procedure across all profiles in the day yields a time series of PBLH values, which is then used to construct the daily PBLH evolution for each station and date.

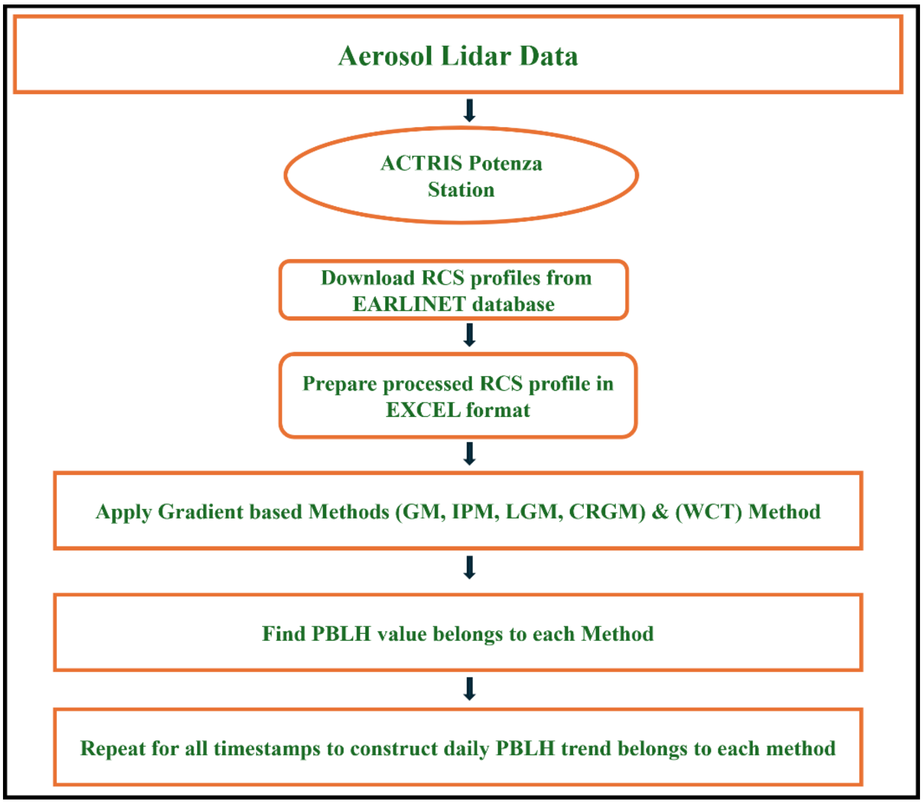

Figure 3.4. Flowchart illustrating the processing steps of aerosol lidar data using gradient based and wavelet covariance transform methods.

3.5.2 Algorithm for Ceilometer Lidar Data

For the analysis of the ceilometer lidar dataset, the error function fit (ERF-Fit) method was employed, as discussed in the previous section. The ceilometer data were obtained from the Cloudnet data portal corresponding to the ACTRIS Potenza station, where the Vaisala (CL51) ceilometer is operated. For the ACTRIS Lampedusa station, a Lufft (CHM 15k) ceilometer is operated, and the implementation of the algorithm and the corresponding analysis are presented in Chapter 4. The selection of the days was made in the same way as described in the previous section for the aerosol lidar, to minimise the influence of Saharan dust and cloud cover on the backscatter profiles.

The product retrieved from the Cloudnet portal provides hourly averaged backscatter profiles with a vertical resolution of 10 m, covering an altitude range from the surface up to 15.000 m. This hourly averaged dataset is merged into a single 24-hour NetCDF file, allowing continuous and reliable monitoring of the boundary-layer evolution throughout the day.

The complete sequence of steps adopted for the implementation of the ERF-Fit algorithm on the ceilometer backscatter profile is summarized in the flowchart Figure 3.5. The data processing starts with the conversion of NetCDF files into Excel file to facilitate data handling. After that, the full 24-hour backscatter signal profile belongs to each day is divided into individual hourly segments, that are further analysed separately. For each hourly backscatter profile, an initial guess of the mixed layer height (z_m) is made by locating the sharp decrease in the backscattered signal intensity that typically marks the transition from the well mixed layer to the free troposphere. After identifying this transition region, the mean backscatter values within and above the mixed layer denoted as (B_m) and (B_u), respectively, are estimated along with an initial value for the transition width (s). These initial parameters are used as inputs to perform a robust least square fit of the error function model to the observed backscatter profile. The optimized parameter obtained from the fit includes (z_m, B_m, B_u, and s), where the fitted z_m represents the PBLH for that specific hour.

This procedure is repeated for all hourly profiles throughout the 24-hour period, and hourly PBLH values derived from the ERF-fit algorithm are then put together to construct a continuous daily trend of the PBL height evolution.

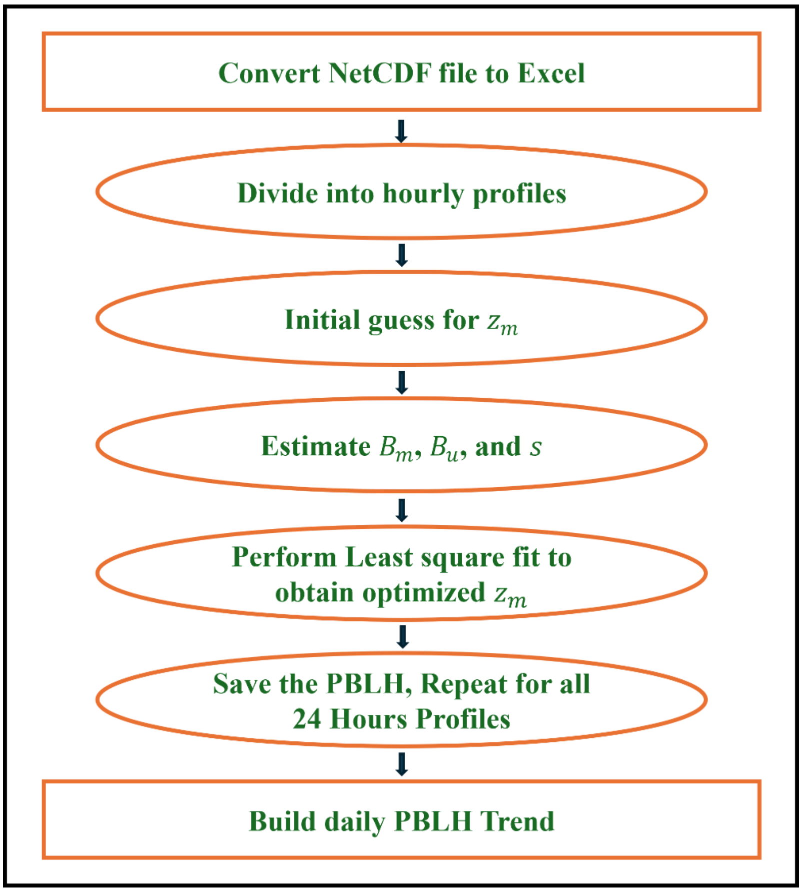

Figure 3.5. Flowchart showing the ERF-fit algorithm applied to ceilometer backscatter data for hourly and daily PBLH retrieval.

3.5.3 Algorithm for Wind Doppler Lidar Data

For the wind doppler lidar dataset, as outlined in the previous sections, two retrievals methods were applied depending on the scan type, the vertical velocity variance method for vertical stare mode and the wind shear method for the DBS mode. The data were provided by the ACTRIS Potenza facility, acquired by HALO Photonics Streamline 120 wind Doppler lidar. Due to limited data availability, one representative day was selected for this analysis, corresponding to 01-03-2021. The selected day corresponds to dust-free and cloud free conditions, to reduce the influence on the Doppler signal and to obtain a reliable PBLH evolution.

For the staring mode, the instrument records the vertical Doppler velocity w with spatial range resolution of 30 m, and the data files were available in HPL format in which the measurements were aggregated to 1-minute values within each hour. The processing workflow, summarized in the flowchart Figure 3.6, begins by converting the HPL files to excel for each hour. For every height level, the mean vertical velocity and the variance are computed over the 1-minute time series within the hour.

The variance profile σ_w^2 is then plotted against height. A threshold is defined by fraction method that relies on the maximum value of variance. The PBL top for the given hour is identified as the lowest altitude where σ_w^2 falls below this threshold, indicating the transition from turbulent mixed layer to free troposphere. Applying this procedure for all hours yields the daily PBLH trend from the variance method.

For the DBS scans, the instrument acquires doppler velocity data over every 5 minutes. The resulting 5-minute doppler-velocity profiles were provided in HPL format. Each 5-minute profile is processed with a standard VAD solution to retrieve the wind components u, v, and w. The hourly profiles of all wind components are obtained by averaging the all 5-minute profiles within each hour. The total horizontal wind speed (V) and direction (γ) are then computed.

For the wind-shear method, the hourly profile of total horizontal wind speed (V) is divided into adjacent altitude layers (consistent with the 30 m range resolution), and the wind shear ($\Delta V/\Delta z$) is calculated for each altitude layer. The PBL top is defined as the altitude (or altitude layer) at which wind shear attains its maximum value during convective hours, representing the sharp increase of horizontal wind across the capping inversion. To support wind shear interpretation, the hourly wind-direction data are also grouped by altitude layers and summarized as wind-rose plots to verify directional shifts during the specific hours. The complete steps involved in the DBS scan data processing is also shown in the Figure 3.6.

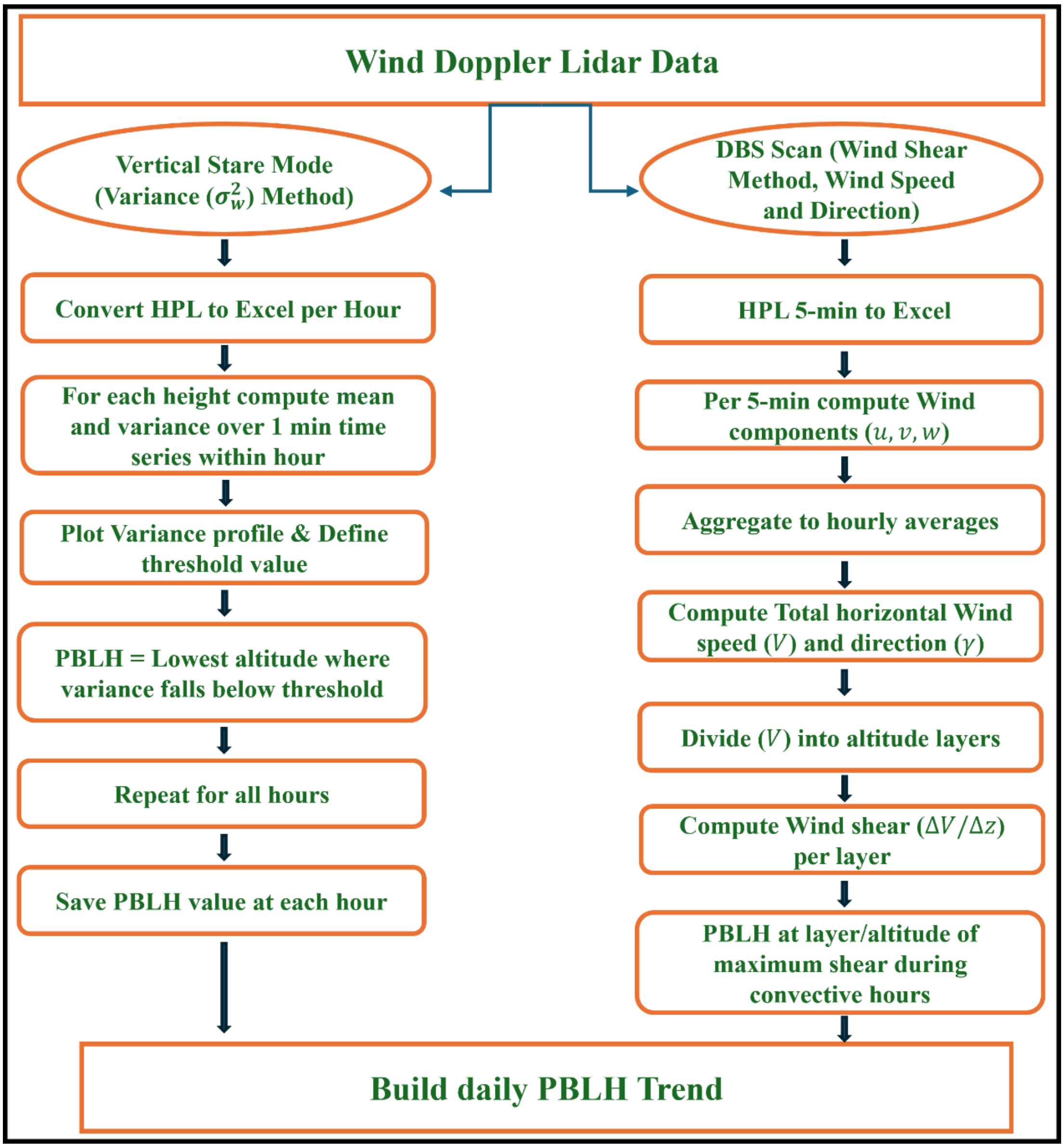

Figure 3.6. Flowchart outlining the wind doppler lidar data processing using the variance and wind shear methods for the PBLH estimation.

3.6 Results and discussion

In this section, the results obtained after implementing the retrieval algorithms on the datasets from the three lidar systems are presented. The analysis is concentrated on the dataset available from the ACTRIS Potenza station. The Potenza dataset includes simultaneous measurements from all three instruments: aerosol lidar, ceilometer, and wind Doppler lidar. All PBLH values reported in this section are expressed as height above ground level (a.g.l.), i.e., relative to the Potenza station altitude. In particular, the extensive datasets from the aerosol and ceilometer lidars have enabled an assessment of the seasonal behaviour of the PBL at this location. The following subsections present and discuss in detail the results obtained from each instrument type.

3.6.1 Results from Aerosol Lidar data

To investigate the seasonal behaviour of PBLH and to compare the performance of different retrieval methods, fifteen representative days from each season between 2020 and 2024 were selected. The multi-wavelength aerosol lidar data at 1064, 532, and 355 nm were retrieved from the EARLINET database for the ACTRIS Potenza station. The PBLH was determined by applying five retrieval algorithms, four gradient-based methods (GM, IPM, LGM, and CRGM) and the WCT. Figure 3.7 illustrates a representative example of a single hour RCS profile together with the application of the GM, IPM, LGM, CRGM, and WCT methods used to determine the PBLH for that specific time. Each panel shows the corresponding transformation or covariance profile, where the identified altitude of the absolute minimum (for the gradient method) or maximum covariance (for WCT) marks the retrieved PBLH. In this example, the retrieved PBLH values range from 1230 m (IPM) to 1470 m (LGM), while GM, CRGM and WCT provide the same estimate of 1410 m. Here IPM gives lower PBLH estimates because it uses the second-derivative (inflection-point) minimum, which typically occurs below the strongest first-derivative gradient, whereas LGM provides slightly higher PBLH because its signal transformation filters information near the ground **(Wang et al., 2021)**. In the same way, this procedure was repeated for every time step throughout the day to obtain the PBLH values for each profile, which were then combined to construct the full daily evolution of the boundary layer height.

The resulting seasonal averages of the daily PBLH variations are presented in Figure 3.8, which illustrates the seasonal comparison across all methods and wavelengths. Similarly, Figure 3.9 shows the averaged diurnal PBLH trends grouped by season, allowing a direct comparison of the different retrieval methods. The detailed interpretation of the seasonal and method-based comparisons is presented in the following discussion.

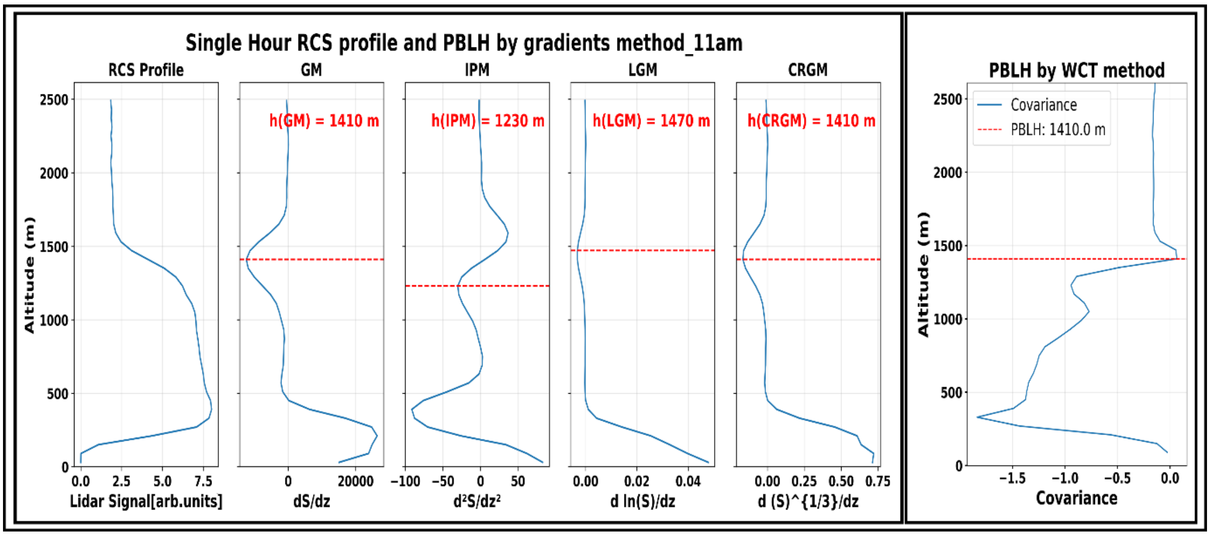

Figure 3.7. Representative single hour RCS profile showing PBLH retrievals obtained with five methods (GM, IPM, LGM, CRGM, and WCT).

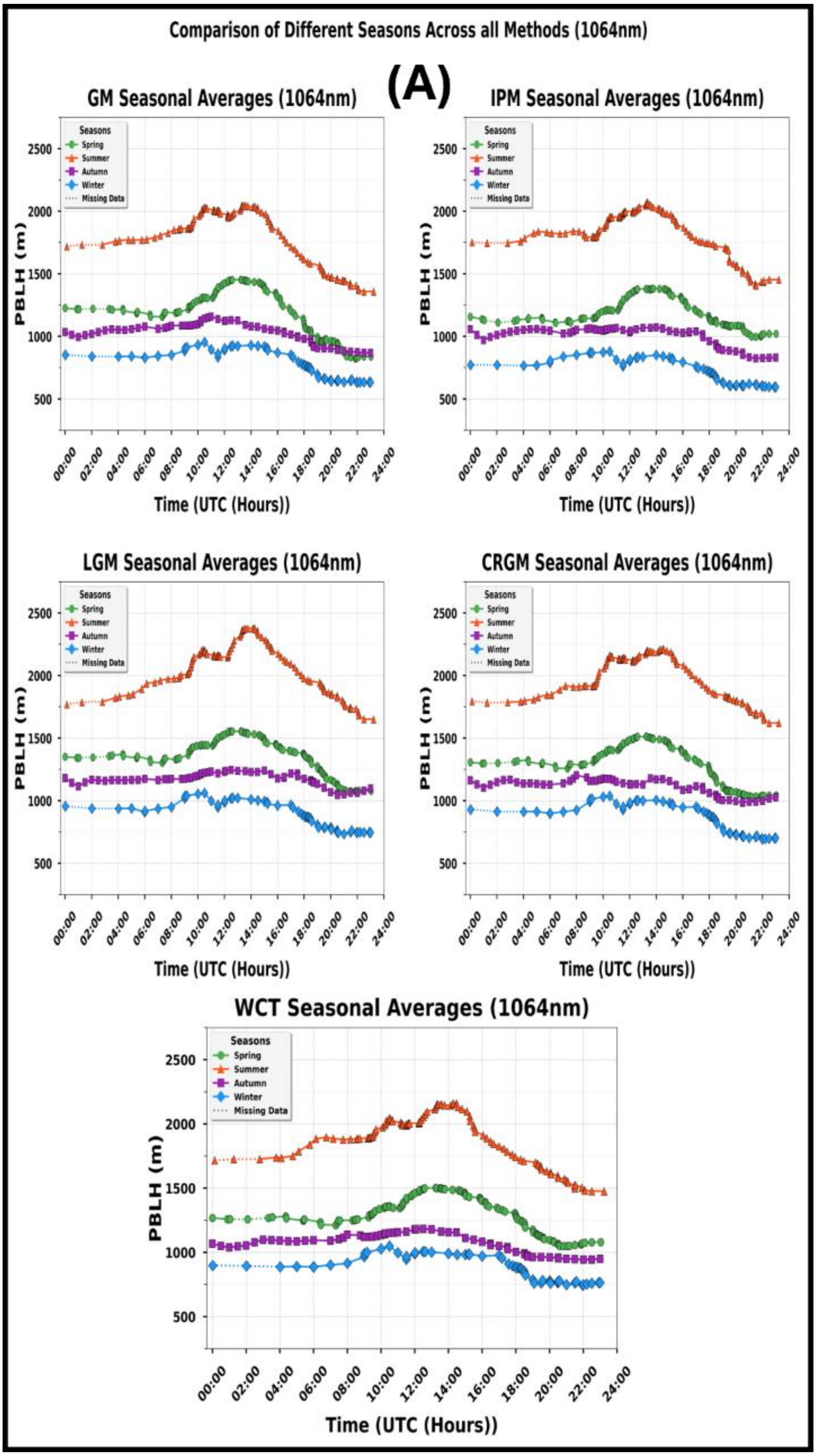
Comparison of Different Seasons Across all Methods (1064nm)
(A)
GM Seasonal Averages (1064nm)
IPM Seasonal Averages (1064nm)
LGM Seasonal Averages (1064nm)
CRGM Seasonal Averages (1064nm)
WCT Seasonal Averages (1064nm)
Seasons
Spring
Summer
Autumn
Winter
Missing Data
PBLH (m)
Time (UTC (Hours))
2500
2000
1500
1000
500
00:00
02:00
04:00
06:00
08:00
10:00
12:00
14:00
16:00
18:00
20:00
22:00
24:00

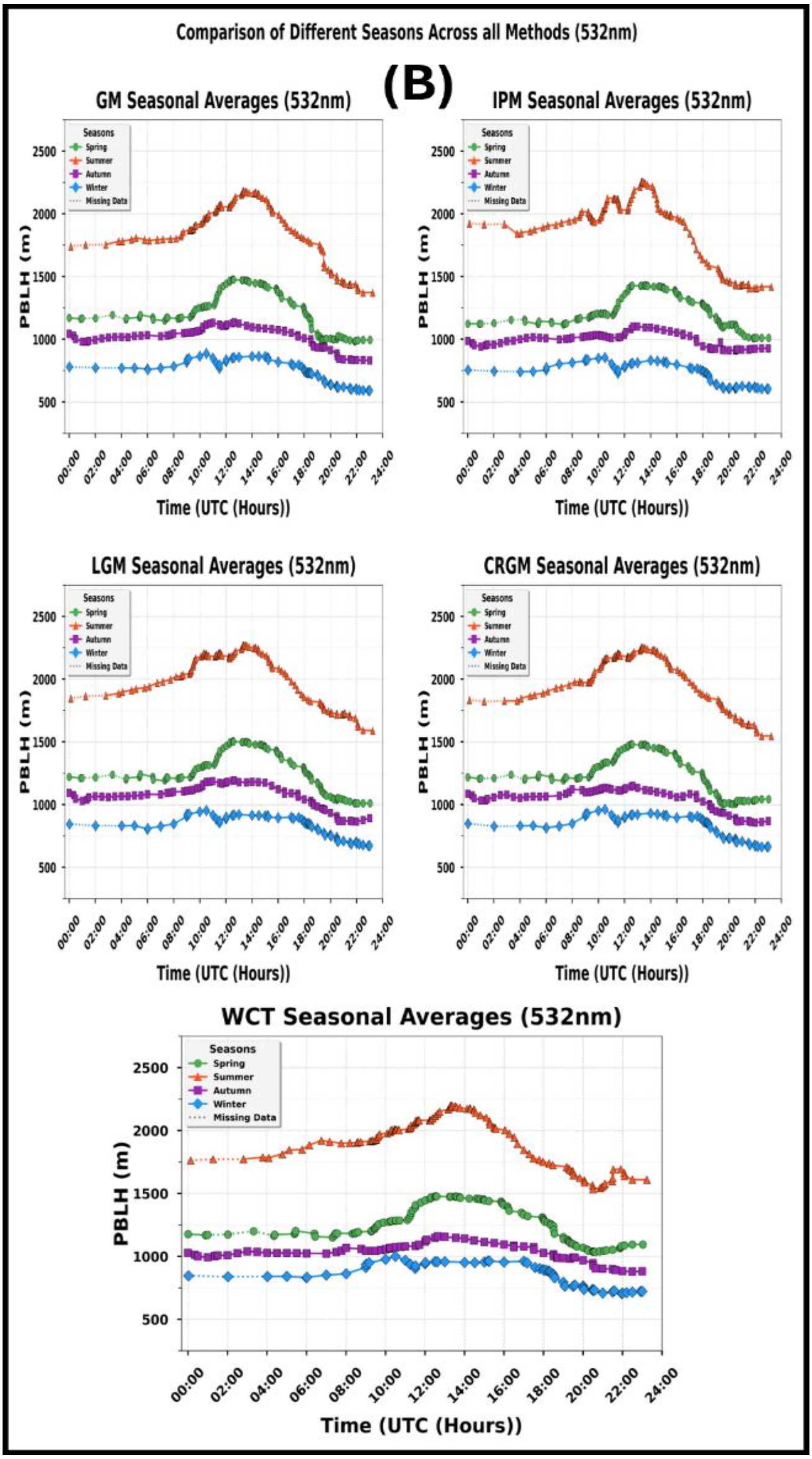

Comparison of Different Seasons Across all Methods (532nm)
(B)
GM Seasonal Averages (532nm)
IPM Seasonal Averages (532nm)
LGM Seasonal Averages (532nm)
CRGM Seasonal Averages (532nm)
WCT Seasonal Averages (532nm)
Seasons
Spring
Summer
Autumn
Winter
Missing Data
PBLH (m)
Time (UTC (Hours))

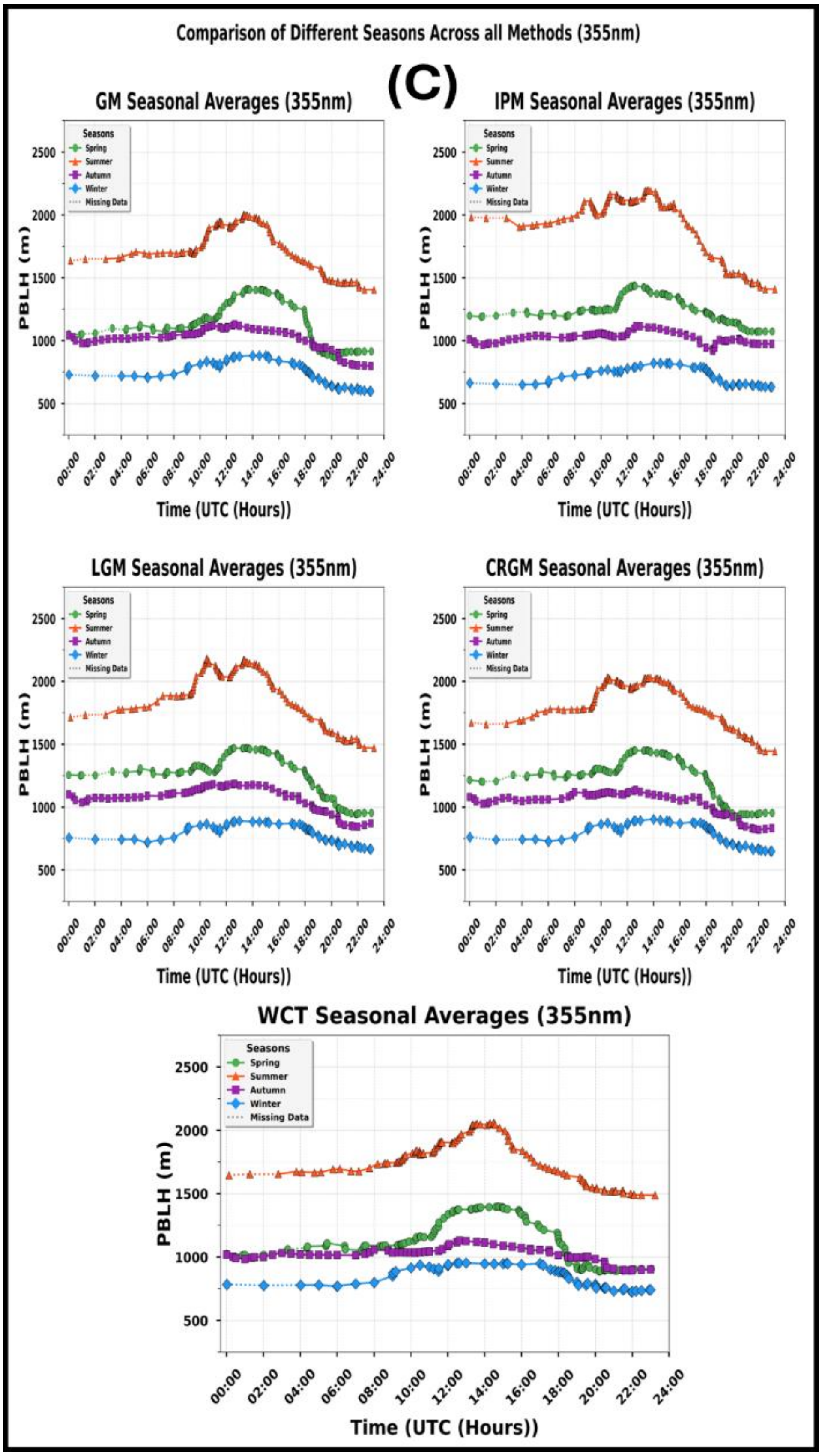

Figure 3.8. Seasonal comparison of the average diurnal variation of the PBLH retrieved using five algorithms (GM, IPM, LGM, CRGM, and WCT) over Potenza. Panels show results at (A) 1064 nm, (B) 532 nm, and (C) 355 nm.

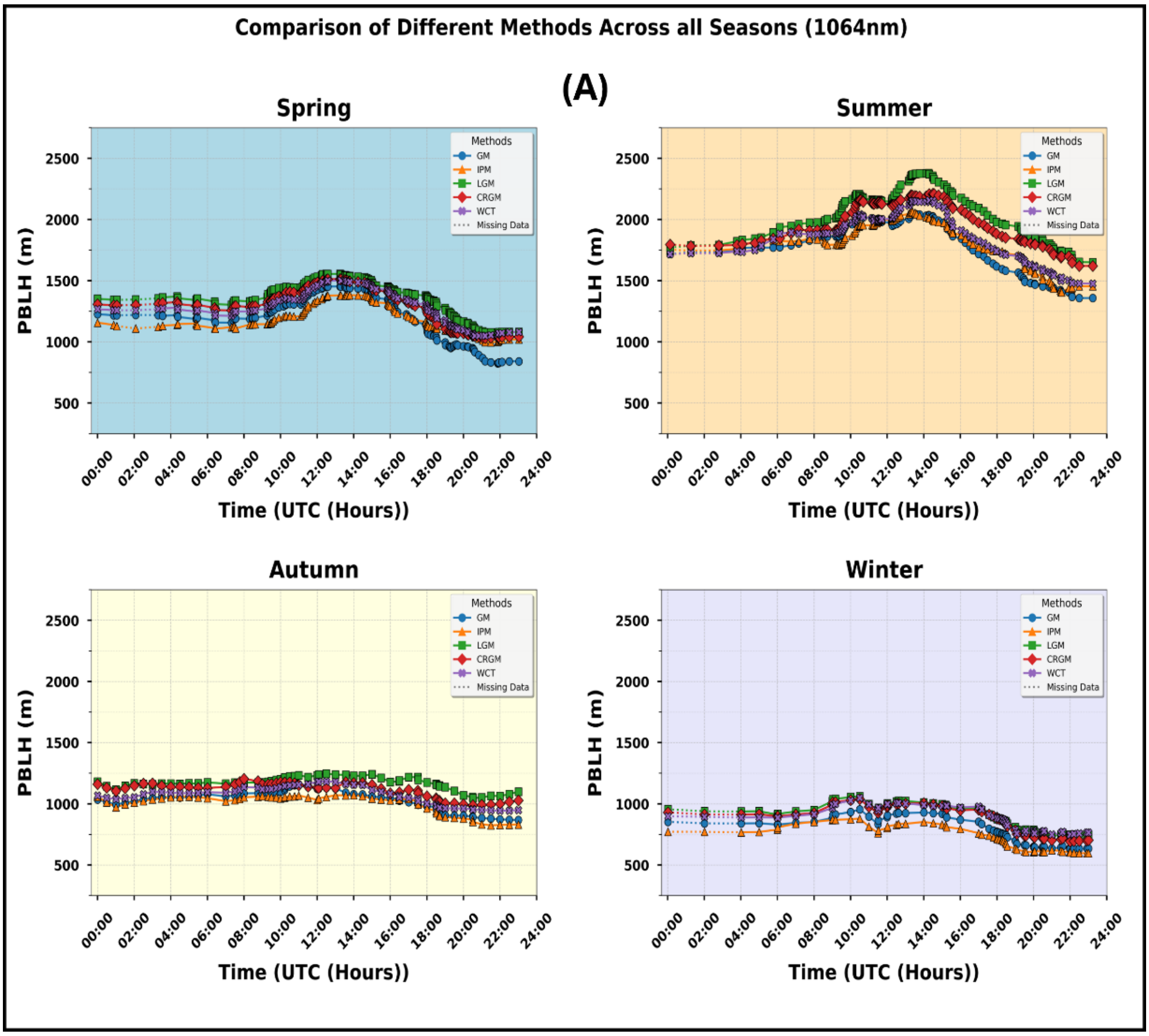
Comparison of Different Methods Across all Seasons (1064nm)
(A)
Spring
Summer
Autumn
Winter
PBLH (m)
Time (UTC (Hours))
Methods
GM
IPM
LGM
CRGM
WCT
Missing Data

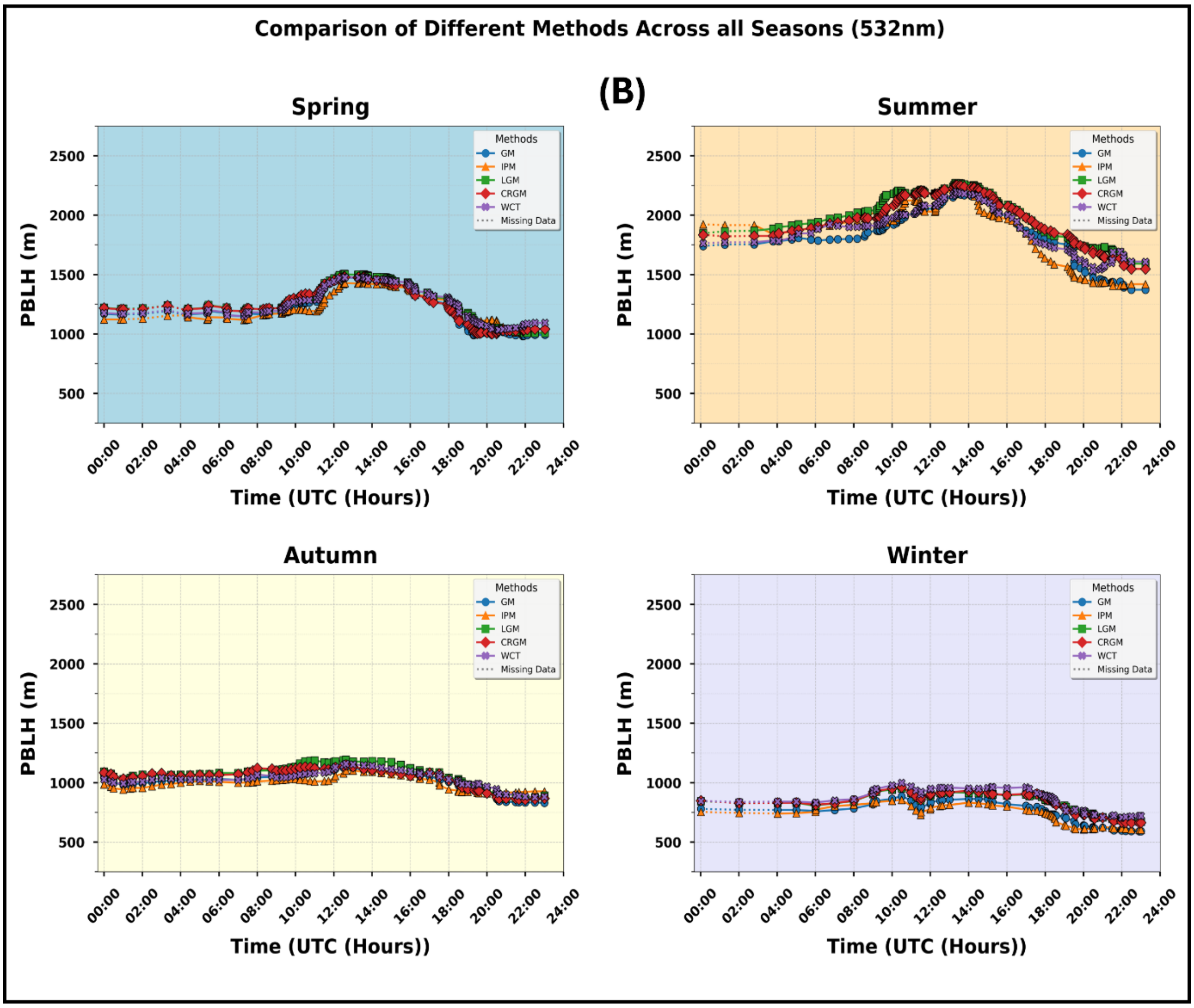

Comparison of Different Methods Across all Seasons (532nm)
(B)
Spring
Summer
Autumn
Winter
Methods
GM
IPM
LGM
CRGM
WCT
Missing Data
PBLH (m)
Time (UTC (Hours))

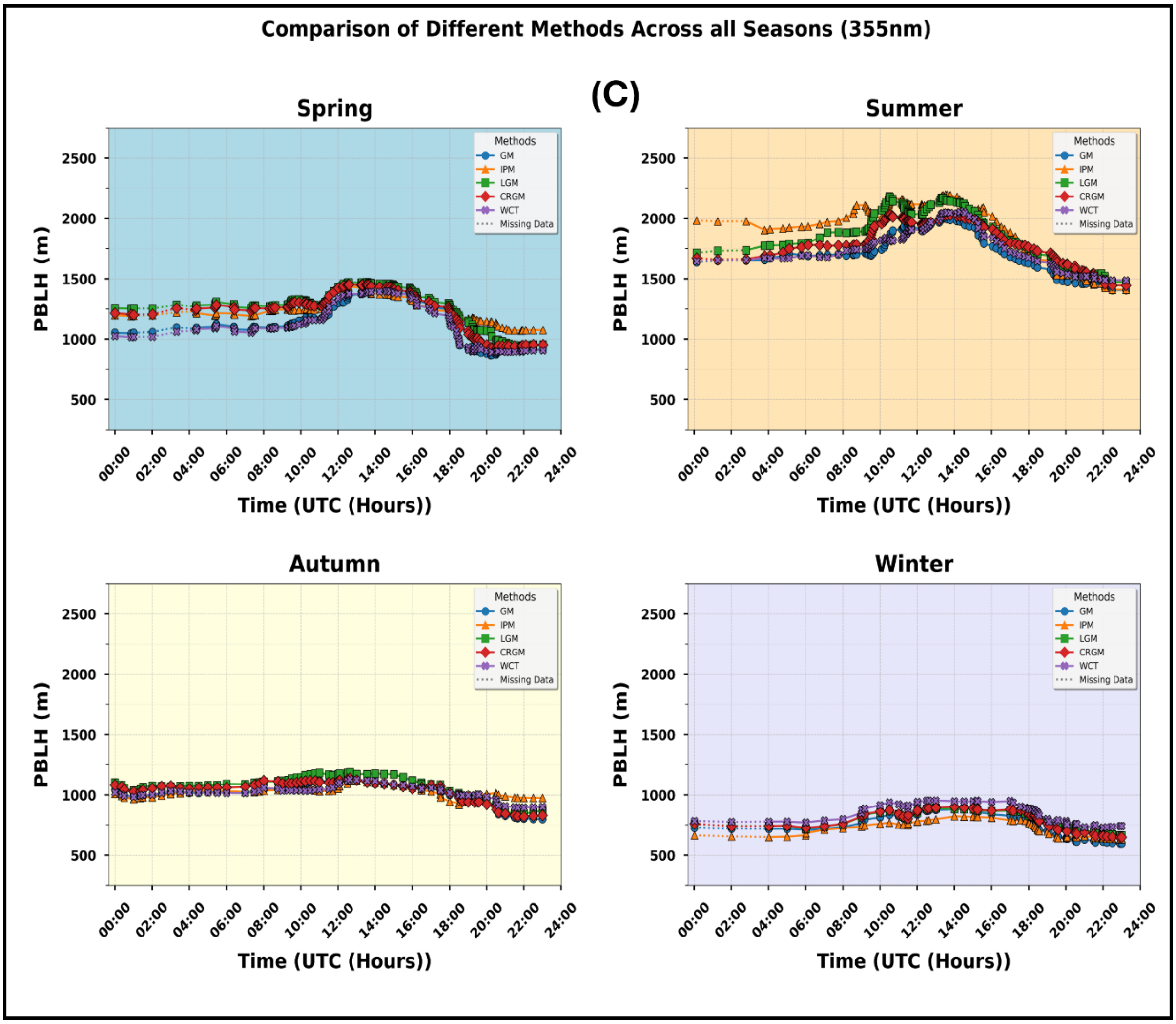

Figure 3.9. Comparison of the PBLH retrieved using five algorithms (GM, IPM, LGM, CRGM, and WCT) for each season over Potenza. Panels show results at (A) 1064 nm, (B) 532 nm, and (C) 355 nm.

Spring Season:

Across all methods and wavelengths during the spring season (green curves in Fig. 3.8A-C), PBLH shows a definite daytime rise and nocturnal recession. Overnight (00:00-04:00 UTC), average PBLH is about ~1000-1350 m. It then starts increasing during the morning period (06:00-10:00 UTC) and reaches ~1100-1400 m. In the midday to early afternoon period (12:00-16:00 UTC), average PBLH is usually at its maximum in the range ~1350-1550 m, before declining slowly again towards the night-time period (20:00-24:00 UTC) during which average PBLH ranges between ~800 and 1100 m. This daytime cycle applies to all methods (GM, IPM, LGM, CRGM, WCT) and across all wavelengths (1064, 532, and 355 nm). This is the indication of start of increased solar heating during the spring season.

The higher PBLH during spring relative to winter is consistent with the seasonal increase in daylength and sun angle, which enhances daytime surface heating after sunrise and promotes a deeper convective mixed layer **(Stull, 1988, pp. 1-28)**, as also reported in the literature **(Pal & Haeffelin, 2015)**. In the Basilicata region, where the Potenza station is located, mean spring precipitation is on the order of 195.15 mm, which indicates that spring remains a relatively wet transition season compared with summer **(Piccarreta et al., 2004)**. Overall, spring PBLH values are intermediate in height: they are higher than winter PBLH values but much lower than summer PBLH values, which reflects the balance of moderate insolation.

Method comparison (Spring Season):

For the spring season **(Fig. 3.9A-C)**, it is observed that LGM and CRGM generally produce the maximum PBLH (~1500-1600 m in the afternoon), IPM gives the minimum (~1300-1400 m), and GM and WCT (~1400-1500 m) are found to be intermediate between LGM/CRGM and IPM. In spring, LGM and CRGM tend to return slightly higher PBLH than GM/IPM because their signal transformations can shift the altitude of the strongest detected gradient, while IPM (as an inflection-based criterion) can select a lower feature within the finite-thickness transition zone near the mixed-layer top. GM and WCT often fall between these estimates, consistent with their different sensitivity to profile structure and to which feature is selected.

These results are consistent at all wavelengths (355, 532, and 1064 nm), and the overall shape of the afternoon PBLH evolution is similar, with small amplitude differences, generally one to two range bins (60-120 m), that may be related to wavelength-dependent scattering. Across wavelengths, the 355 nm retrievals can appear slightly lower than those at 532 and 1064 nm, because the shorter wavelength has a stronger molecular (Rayleigh) contribution, which reduces the particle-to-molecular contrast and can weaken the PBL-related gradient used by the detection methods **(Wandinger, 2005)**. In terms of method-to-method variability, the inter-method spread is more pronounced at 1064 nm than at 532 and 355 nm, which is consistent with the stronger particle-to-molecular contrast at longer wavelengths and the resulting higher sensitivity to aerosol-layer structure, thereby increasing the chance that different methods select slightly different features.

In the morning period, GM and WCT, compared with IPM, tend to retrieve higher PBLH at 1064 and 532 nm than at 355 nm, while by afternoon the convective mixing produces a clearer gradient near the CBL top and the different methods tend to agree more closely. At night-time, the presence of weak layers (e.g., a surface layer and an overlying residual layer) can increase variability between methods and wavelengths, because under stratified conditions different algorithms may select different features within the same profile (Wang et al., 2021).

Summer Season:

For the summer season (orange curves in Fig. 3.8A-C) all methods return higher midday average PBLH values compared with other seasons. Overnight (00:00-04:00 UTC) average PBLH is already fairly high ~1600-1900 m. In the morning (06:00-10:00 UTC), average PBLH keeps expanding around ~1700-2200 m, and during early afternoon (12:00-16:00 UTC), peaks reach at ~1900-2400 m. This extreme daytime mixing is much greater than during any other season. Moving towards the evening, average PBLH starts declining slowly. In the night-time period (20:00-24:00 UTC) for this season average PBLH range is (~1350-1800 m).

At Potenza, summer is typically hot and generally dry, as the site is strongly influenced by Mediterranean atmospheric circulation (Madonna et al., 2011), and summer precipitation in the Basilicata region is about 94.53 mm (Piccarreta et al., 2004). These conditions support stronger surface solar input, that favours more intense daytime heating and convective boundary-layer growth, as discussed in the literature (Pal & Haeffelin, 2015). During the afternoon, the mountainous terrain around Potenza may promote upslope and valley circulations that modify boundary-layer mixing and can contribute to higher PBLH values, as discussed by (Garratt, 1994). Conversely, clear sky cooling during the night-time still produces large residual heights, but this height is quite lower than the daytime peaks. Overall, the observed summer PBLH evolution relative to other seasons is characterised by a strong convective regime associated with a Mediterranean climate and increased solar forcing.

Method comparison (Summer Season):

During the summer season (Fig. 3.9A-C), all methods show the largest daytime PBLH peaks at all three wavelengths (355, 532, and 1064 nm) compared with the other seasons. For the 1064 nm retrievals, LGM and CRGM again produce the higher afternoon PBLH peaks (~2200-2400 m), while WCT typically gives intermediate peaks (~2000-2200 m). In contrast, GM and IPM tend to provide comparatively lower afternoon peaks. Across wavelengths, for 532 and 355 nm, the corresponding maxima are generally one to two range bins (60-120 m) lower than at 1064 nm, and the different methods tend to converge more closely during the afternoon. This small amplitude offset is consistent with wavelength-dependent sensitivity of the backscatter profile, where the shorter wavelength can have a stronger molecular contribution and thus a weaker particle-to-molecular contrast, which can reduce the sharpness of the PBL-related gradient (Wandinger, 2005). In terms of method-to-method variability, the inter-method spread is again more evident at 1064 nm than at 532 and 355 nm, consistent with the wavelength-dependent contrast effects discussed above.

In summer, IPM at 1064 nm again tends to select a lower inflection feature than the gradient-based criteria, whereas at 532 nm it more often converges with the other methods. At 355 nm, however, IPM can retrieve higher PBLH than the other methods. A physically plausible explanation is that this may occur under strong convective conditions when residual or elevated aerosol layers are present along with the growing mixed layer; in such cases, an inflection-based criterion can be influenced by curvature features not uniquely associated with the mixed-layer top, which can lead to higher retrieved heights. This behaviour is consistent with the general sensitivity of lidar-based approaches to multilayer structure and to the finite thickness of the transition zone (Wang et al., 2021).

Early-morning PBLH values are already relatively large at all wavelengths (~1700-1950 m), and among the methods IPM can yield the higher values, particularly at 355 nm. In this time window, the most likely reason is that remnants of the nocturnal residual layer can persist above the surface layer, so some algorithms may identify the residual-layer top rather than the developing mixed-layer top. As the day progresses into the afternoon, the convective boundary layer deepens and the transition at the mixed-layer top becomes more prominent. As a results, all methods tend to return similarly large PBLH values, while LGM and CRGM often remain slightly higher at all wavelengths because of their signal transformations. Toward evening and night, all methods show a decreasing PBLH.

Overall, summer PBLH is retrieved slightly higher at the longer wavelengths (1064 and 532 nm) than at 355 nm, which is consistent with the reduced relative influence of Rayleigh scattering at longer wavelengths (Wandinger, 2005). The small differences between methods are most plausibly linked to their different sensitivity to aerosol stratification (e.g., residual or elevated layers), because under such conditions different algorithms can select different features within the same profile (Wang et al., 2021).

Autumn Season:

The autumn season (purple curves in Fig. 3.8A-C) exhibits considerably weaker development of average PBLH trend compared to the other seasons. Overnight (00:00-04:00 UTC), average PBLH is low, ~950-1150 m. In the morning (06:00-10:00 UTC), it increases only slightly,

~1000-1200 m. During the afternoon (12:00-16:00 UTC), it reaches only an altitude of ~1050-1250 m. Following the afternoon peak, average PBLH starts decreasing. Therefore, the typical diurnal cycle of PBLH growth and decline is still present, but significantly less pronounced than in the other seasons. Moreover, during the night-time period (20:00-24:00 UTC) the average PBLH ranges between ~800 and 1100 m.

As the autumn season in Potenza moves from hot to cold periods, solar input decreases and days become shorter; in addition, autumn precipitation in the Basilicata region is about 242.96 mm **(Piccarreta et al., 2004)**. As the surface energy balance varies through the diurnal cycle, the boundary-layer regime over land changes accordingly: after sunrise, solar heating of the ground generates buoyant thermals and a convective mixed layer that deepens through the day, whereas reduced surface heating leads to weaker convective mixing and a shallower daytime boundary layer **(Stull, 1988, pp. 1-28)**. Overall, this reduced solar input compared with summer and spring may decrease PBL depth during autumn, as also reported in the literature **(Pal & Haeffelin, 2015)**.

Method comparison (Autumn Season):

During the autumn season **(Fig. 3.9A-C)**, the diurnal PBLH is lower and more stable than in summer and spring. Across all methods and wavelengths, the afternoon PBLH peaks are typically in the range ~1100-1250 m. It is observed that during the afternoon the methods converge particularly at 355 and 532 nm, and that at all wavelengths the small inter-method differences (IPM slightly lower and LGM slightly higher) are generally on the order of one range bin (60 m), i.e., within the vertical resolution of the measurements. In addition, across wavelengths, the differences in the afternoon peaks are small (also on the order of one range bin), which is consistent with the stronger molecular (Rayleigh) contribution at 355 nm and the associated reduction in particle-to-molecular signal contrast relative to 532 and 1064 nm **(Wandinger, 2005)**. In terms of method-to-method variability, the inter-method spread remains more pronounced at 1064 nm than at 532 and 355 nm, in line with the same wavelength-dependent contrast effects.

In autumn, early-morning PBLH values at all wavelengths are already around ~1000-1200 m. Across wavelengths, the 532 and 355 nm retrievals can appear one range bin lower than 1064 nm, which is consistent with the reduced particle-to-molecular contrast at shorter wavelengths. During this early-morning period, the differences between methods are small, with LGM and CRGM tending to give slightly higher values than GM, WCT, and IPM. These small differences between methods are most plausibly linked to their different sensitivity to aerosol stratification (e.g., residual or elevated layers), because under such conditions different algorithms can select different features within the same profile **(Wang et al., 2021)**.

During the afternoon, solar heating still supports convective mixing **(Stull, 1988, pp. 1-28)**, but because autumn days are shorter and the convective regime is typically more moderate than in summer, only a modest daytime growth of the mixed layer is generally observed across all methods and wavelengths. In this period, LGM remains slightly higher at all wavelengths, which is consistent with the effect of signal transformations and smoothing. At night-time, particularly at 1064 nm, larger inter-method differences can occur. A likely reason is wavelength-dependent scattering and the coexistence of a shallow surface layer and an overlying residual layer, which can introduce multiple gradients in the aerosol profile and increase the chance that different algorithms select different features **(Wang et al., 2021).**

Overall, in the autumn season the 1064 nm retrievals exhibit slightly higher PBLH peaks than 532 and 355 nm, whereas the wavelength-to-wavelength differences remain small and are consistent with wavelength-dependent scattering effects and the relative influence of molecular backscatter **(Wandinger, 2005).**

Winter Season:

The winter season (blue curves in **Fig. 3.8A-C)** has the flattest and shallowest average PBLH trend among all seasons. All methods usually report average PBLH values of ~600-1100m, with minimal daytime growth. Minimum values are reported at night (20:00-24:00 UTC) and overnight (00:00-04:00 UTC) when PBLH values are around ∼600-900 m, and even the maximum during the morning (06:00-10:00 UTC) and afternoon (12:00-16:00 UTC) rarely exceeds around ~750-1050m. Daytime growth is generally only two to three range bins above the nighttime peaks.

Winter at Potenza is the cold season **(Madonna et al., 2011)**, and winter precipitation in the Basilicata region is about 267.64 mm **(Piccarreta et al., 2004)**. Over moist surfaces, a larger fraction of the available energy is partitioned into latent heat flux and a smaller fraction into sensible heat flux, which reduces surface sensible heating available to drive buoyant convection **(Stull, 1988, pp. 251-294)**. Consequently, a shallow convective layer is expected, and diurnal warming is able to raise the PBL by at most only a few hundred meters, as also reported in the literature **(Pal & Haeffelin, 2015)**. Along with that, mountainous slopes may also allow cold air to drain at night into the valleys, enhancing the development of a strong surface inversion.

Therefore, during the winter season, no deepening of the PBL is observed and the boundary layer is founded highly stable as compared to all other seasons.

Method comparison (Winter Season):

During the winter season (Fig. 3.9A-C), the afternoon PBLH peaks are markedly lower than in the other seasons. Across all methods and wavelengths, the reported afternoon PBLH peaks are typically ~750-1050 m. Across wavelengths, the 1064 nm peaks are generally one range bin higher than those at 532 and 355 nm, which is consistent with wavelength-dependent sensitivity of the backscatter profile (Wandinger, 2005). In terms of method-to-method variability, the inter-method spread is again more pronounced at 1064 nm than at 532 and 355 nm, consistent with the wavelength-dependent contrast effects discussed above. In the afternoon, LGM and CRGM, together with WCT, tend to retrieve slightly higher PBLH than GM, whereas IPM typically gives the lower estimates. This behaviour is physically consistent with stable wintertime stratification, during which the mixed layer is typically capped by an inversion/entrainment zone that restricts further vertical growth. Under these conditions, covariance-based approaches can be influenced by the upper edge of that transition, while an inflection-based criterion may select a lower curvature feature within the same finite-thickness transition zone.

In the early-morning period, all methods report PBLH values of about ~600-900 m at all wavelengths, and again the 1064 nm retrievals are commonly one to two range bins higher than 532 and 355 nm. LGM, CRGM, and WCT often lie close to each other, whereas GM remains slightly lower and IPM tends to provide the minimum estimates. In winter, weaker surface heating and enhanced stability limit convective development, so the daytime boundary layer deepens only modestly, and the mixed layer remains shallow. Under these conditions, the mixed layer is typically capped by an inversion/entrainment zone that restricts further vertical growth (Stull, 1988, pp. 1-28). As a result, methods can diverge: LGM and CRGM (and often WCT) may return slightly higher PBLH, whereas IPM can identify a lower inflection feature. Under stable stratification, the backscatter transition zone can also be relatively deep or ill-defined, and a maximum-only WCT detection can be biased toward the upper edge of that transition (Brooks, 2003).

During winter nights, the reported PBLH values are typically ~600-800 m, and the inter-method differences are generally small at all wavelengths. A likely explanation is that the nocturnal structure is relatively stable and weakly mixed. Overall, winter is characterized by higher stability and shallower PBLH, with 1064 nm retrievals remaining slightly higher than those at 532 and 355 nm, consistent with wavelength-dependent scattering effects (Wandinger, 2005).

Conclusion:

In conclusion, across the four seasons, the three wavelengths provide a consistent picture of the diurnal cycle at Potenza, with the deepest daytime development in summer, intermediate growth in spring, a clearly reduced amplitude in autumn, and the shallowest and most stable conditions in winter. Across wavelengths, a small but consistent wavelength effect is observed, with 1064 nm generally giving slightly higher PBLH peaks than 532 and 355 nm, while the 355 nm estimates tend to be slightly lower, consistent with wavelength-dependent scattering and the stronger molecular contribution at shorter wavelengths. In the warm seasons (Spring, Summer), all methods capture a pronounced daytime rise and afternoon maximum, whereas in the cold seasons (Autumn, Winter) the daytime increase is modest and the PBL remains relatively shallow. Across methods, LGM and CRGM most often yield the highest PBLH, IPM tends to give the lowest values, and GM and WCT are generally intermediate. When the atmosphere is more stratified, particularly in the evening/night-time period or under stable conditions, small inter-method differences can arise because different algorithms can select different features within the same profile.

3.6.2 Results from Ceilometer Lidar Data

Within this analysis, one representative day from each season was selected to investigate the seasonal behaviour of the (PBLH) using the ERF-fit algorithm applied to ceilometer lidar data. For each selected day, the ERF-fit algorithm was implemented on the hourly backscatter profiles to retrieve the PBLH for every hour, from which the corresponding daily trend was constructed. The results include both the single-hour implementation of the ERF-fit algorithm and the full daily trend obtained by combining all hourly PBLH estimates. These are illustrated and discussed in the following figures. Furthermore, the comparison of daily PBLH trends retrieved for the representative days of each season is presented in the form of colour maps, showing the temporal and vertical evolution of the backscatter intensity together with the retrieved PBLH.

Estimation of PBLH using the Error Function Fit Method:

Figure 3.10A shows the hourly vertical profile of aerosol backscatter β(z) from the ceilometer (solid blue) together with the idealized profile (orange dashed) obtained by fitting the four-parameter ERF method. The fitted S shaped curve represents a well-mixed boundary layer capped by a transition to the free troposphere. The PBLH is defined as the midpoint of this transition, and in this case, it is $z_m \approx 1165$ m. The light-blue shaded band marks the entrainment zone (EZ), that is defined as a finite-thickness layer around the PBL top where mixed-layer air mixes with free-tropospheric air. The EZ width quantifies how gradual the capping transition is and broadening of this zone is mainly due to turbulent entrainment, and vertical layering. A thin EZ indicates a sharp, well-defined cap, whereas a thick EZ indicates a more gradual or layered transition. The close agreement between the fitted curve and measured profile through the transition suggests that, during this hour, a single dominant mixed layer characterizes the profile.

After applying the ERF fit method to the 24-hour vertical profiles of aerosol backscatter β(z), we obtained the PBLH values for each hour, and in this way, the complete daily trend of the PBLH is derived. Figure 3.10B therefore provides the hourly trend of the retrieved PBLH for this day, while a more detailed interpretation of this trend is given in the next section using the backscatter colour map in Figure 3.11 and the comparison with the other selected days.

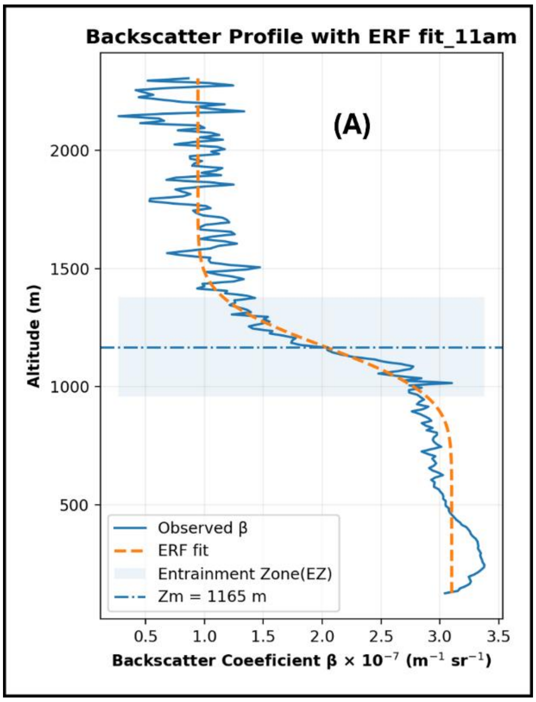

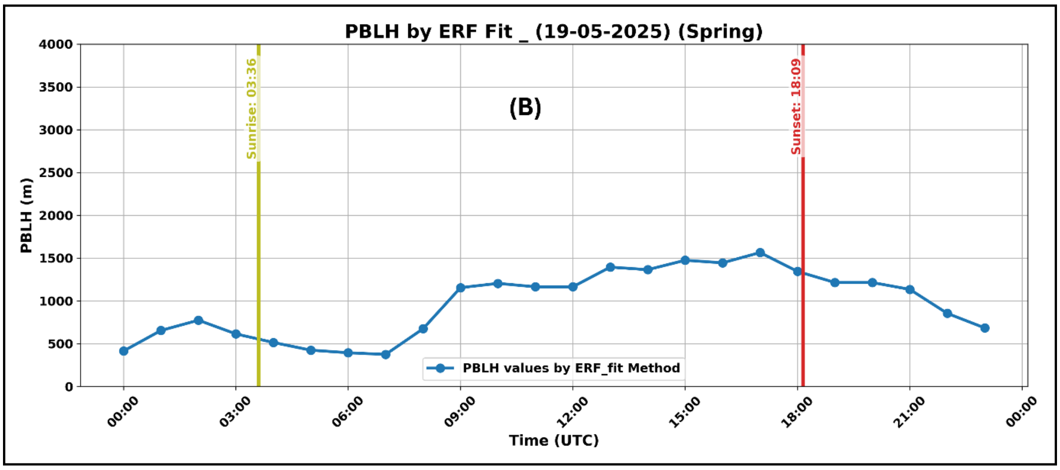

Figure 3.10. (A) Hourly backscatter profile and error function fit for PBLH estimation, (B) Daily evolution of the PBLH retrieved by the ERF fit method.

Comparison of daily PBLH trends retrieved by ERF-Fit Method (All Seasons):

ERF fit method was implemented on the four different days, and each day belongs to different season of the year (Spring, Summer, Autumn, Winter). Each colour map represents the temporal and vertical variation of aerosol backscatter intensity. Warm colours denote higher backscatter due to aerosol-rich air, and cool colours denote lower backscatter. The black stars mark the hourly PBL height z_m derived from the ERF fit method to 60-min averaged profiles. Vertical solid and dashed lines indicate sunrise and sunset time as labelled in each plot of Figure 3.11. In these four days, the star positions align with the visual boundary between the high-backscatter mixed layer below and the lower-backscatter free troposphere above, confirming that the ERF-based z_m follows the observed transition in the backscatter profile.

The day 19-05-2025 belongs to spring season therefore PBLH decreases after midnight and reaches a morning minimum value near 07:00 UTC (375 m), then it starts rising quickly after sunrise and reaches its maximum value of (1565 m) at 17:00 UTC; successively, it again drops to (685 m) at 23:00 UTC. The day 12-08-2024 belongs to summer season, and the daytime boundary layer is deepest among all other days belonging to different seasons; after a pre-dawn minimum around 06:00 UTC (435 m), PBLH rise to (2825 m) at 15:00 UTC, which is the largest PBLH values among these four days. After that the PBL trend decays after sunset and reaches (1365 m) at 23:00 UTC. In autumn day 30-09-2024, after sunrise PBLH increases from (535m) at 07:00 UTC to (1685m) at 14:00 UTC, then decreases to (375m) at 21:00 UTC. Furthermore, in winter day (2024-02-15), the development is shallowest, and PBLH grows from (365m) in the morning at 06:00 UTC to (1095m) at 13:00 UTC, and then steadily declines to (185m) at 23:00 UTC.

For the four representative days, the daytime maximum PBL height follows the expected seasonal ordering, with summer exhibiting the highest peaks (around 2825 m), winter the shallowest peaks (around 1095 m), and spring and autumn intermediate values (around 1565 m and 1685 m, respectively), as reported for a multi-year lidar climatology at another site **(Pal & Haeffelin, 2015)**. The daily maximum occurs consistently in the afternoon period and decrease after sunset. This behaviour of the daily PBL trend is in accordance with seasonal variations in the annual cycle of solar irradiation and solar surface heating, which determine the duration and intensity of convective growth, as also reported in the literature **(Pal & Haeffelin, 2015)**. Overall, these findings are consistent with the predicted response of the boundary layer to variation in surface heating and inversion strength, as also reported in the literature **(Pal & Haeffelin, 2015)**.

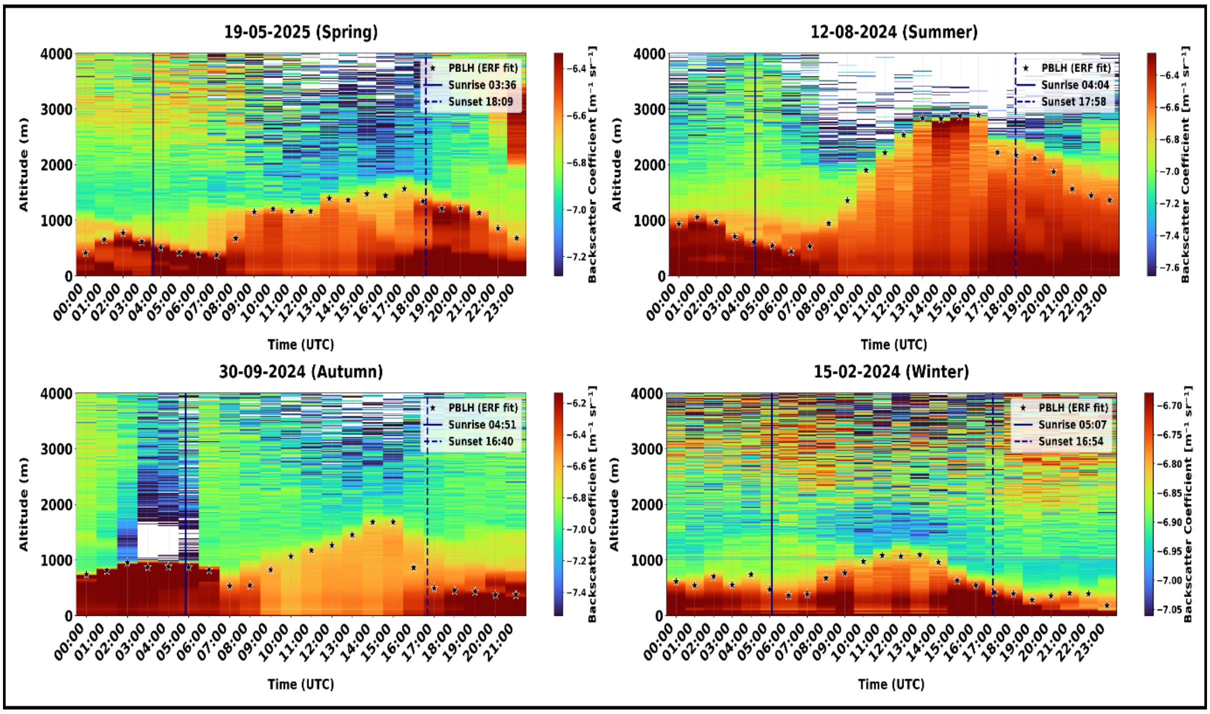

Figure 3.11. Seasonal comparison of daily PBLH retrieved by the ERF fit method.

3.6.3 Results from Wind Doppler lidar Data

For the investigation of PBLH based on wind measurements, this analysis focuses on a single representative day (01-03-2021), due to the limited availability of Doppler wind lidar data. The selected dataset corresponds to the early spring season and includes measurements acquired in both vertical-stare and Doppler Beam Swinging (DBS) scan modes. The PBLH was retrieved using two independent approaches: the vertical velocity variance method and the wind-shear method, while wind-speed and wind-direction analyses were performed to support and validate the results obtained from the wind-shear approach.

For the vertical-stare mode, the retrieved hourly PBLH values are presented to show the daily evolution derived from the variance method, including their representation in the form of colour-map plots. For the DBS mode, the wind-shear method was applied during four selected convective hours (10:00, 12:00, 14:00, and 16:00 UTC), and the corresponding hourly profiles are shown. Wind-speed and wind-direction information for a representative hour at 12:00 UTC is also presented as wind-rose plots to support the interpretation of the wind-shear results. The results are shown and discussed in the following figures.

PBLH estimation by Vertical velocity Variance Method:

Figure 3.12 shows the profile of vertical velocity variance (σ_w^2) against height obtained after processing the data of the vertical stare mode. The blue curve represents the variance, while the red dashed line marks the threshold and the green line indicates the detected PBL top. From this plot it is clear that variance is higher near the surface and in the lower part of the mixed layer, with a maximum value around 400 m. This maximum reflects the strong turbulence in the lower boundary layer that are produced both by surface heating during the day and by mechanical wind forcing close to the ground. Along with that the presence of higher concentration of aerosol in this well mixed region helps wind lidar to capture fluctuations in a more effective way. Above this well mixed region as the signal approaches the free troposphere, the vertical variance drops steadily. This decrease in the vertical variance is due to, weaker turbulence in the free troposphere, that produces more stable air and damps its vertical motion. The PBLH is defined as the point where the vertical variance drops below a particular threshold value and in this case, it was 1065 meter. After applying the vertical variance method to the 24-hour vertical wind velocity profiles, we obtained the PBLH values for each hour. These PBLH values are plotted against their corresponding time in Figure 3.13.

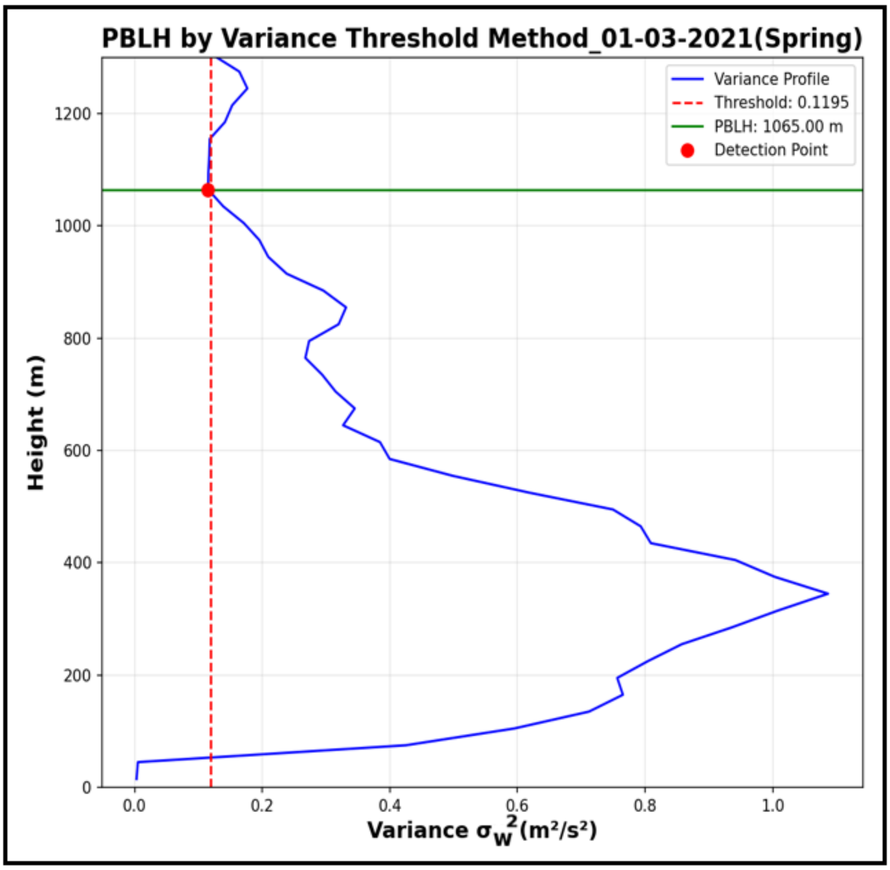

Figure 3.12. Vertical velocity variance (σ_w^2) profile from the vertical stare mode on 01-03-2021.

Daily trend of PBLH by Variance Method (01-03-2021) (Spring):

After applying the vertical variance method to the complete 24 hours dataset for this day, which belongs to the early spring season, the diurnal trend of PBLH was obtained and shown in Figure 3.13. In this plot the vertical velocity variance is plotted as a function of time and height, with the black stars representing the PBLH values derived from 1 hour averaged profiles. It was observed that the boundary layer remains shallow before the sunrise, with PBLH values in the range of 100-400m. This indicates the presence of stable nocturnal boundary layer because of weak turbulence in the atmosphere. The boundary layer starts to raise after sunrise (around 05:30 UTC), because solar heating warms the surface and the air near the ground, that promote convection and higher turbulent mixing **(Moreira et al., 2018)**. The maximum PBLH value that was reported is 1485 m at 13:00 UTC, which indicates the presence of strong convective mixing. As evening approaches, due to the decrease in the solar radiation's turbulence starts to weaken, and PBL gradually declines. The decline in the PBLH occurs more quickly after the sunset, at around 16:46 UTC, and the minimum PBLH value of about 270 m was reported at around 23:00 UTC.

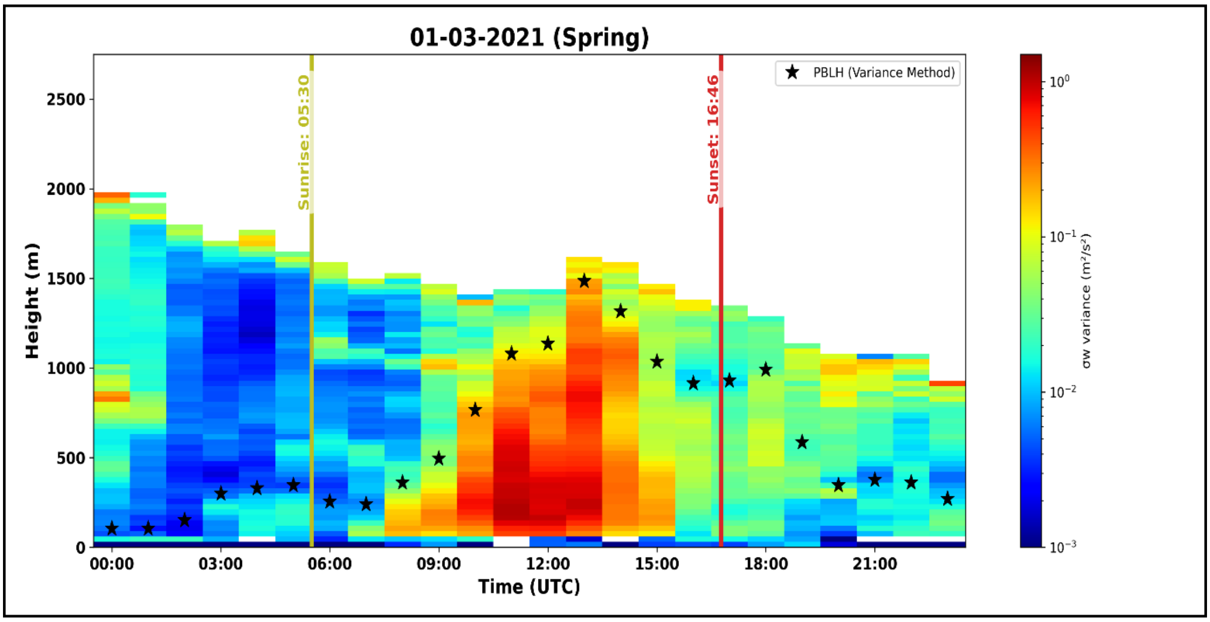

Figure 3.13. Diurnal variation of variance (σ_w^2) and retrieved PBLH on 01-03-2021, using the vertical velocity variance method.

PBLH estimation by Wind Shear Method:

To validate the PBLH obtained from the vertical variance method, the wind shear method was also applied using the DBS scan data for the representative day of the spring season. Figure 3.14 shows the vertical profiles where total horizontal wind speed is plotted along the x-axis and altitude on the y-axis. The blue line represents the variation of horizontal wind speed with height, and the layer where the vertical wind shear is strongest defines the PBL top, which is indicated by a pink band. The PBLH values obtained from the vertical variance method are shown as black stars.

To detect the maximum wind shear in the total horizontal wind speed, the profile is divided into layers of 30 meter in altitude, based on the 30-meter spatial resolution. Four different hours profiles belong to convective boundary layer were analysed for the maximum wind shear. In the first profile at 10:00 UTC, the maximum wind shear was reported in the 750-780 m layer. This number agrees with the vertical variance method PBLH value, which is around 750 m. In the second profile at 12:00 UTC, the maximum wind shear was reported in the 1110-1140 m layer, and during that hour the PBLH value obtained from the vertical variance method was 1100 m, which matches with the PBL layer reported by wind shear method. Similarly, in the 14:00 UTC profile, the maximum wind shear was reported in the 1290-1320 m layer, which again coincide with the PBLH value of 1320 m obtained from the vertical variance method. The CBL is strongly formed during these midday hours, which results in a significant wind shear near the capping inversion. For this reason, both approaches agree well during these early afternoon hours. However, in the late afternoon 16:00 UTC, the wind shear method recognized the maximum shear around 1110-1140 m layer, while the variance method reports the PBLH slightly lower, at about 930 m. This difference in both methods is due to the transition of the boundary layer in the evening hours, as during this period surface heating reduces and turbulence becomes weaker, while the wind shear above the residual layer can remain strong. So, overall, it was observed that during the peak convective period, the two methods provide consistent estimates of PBLH, whereas they diverge during the evening hours.

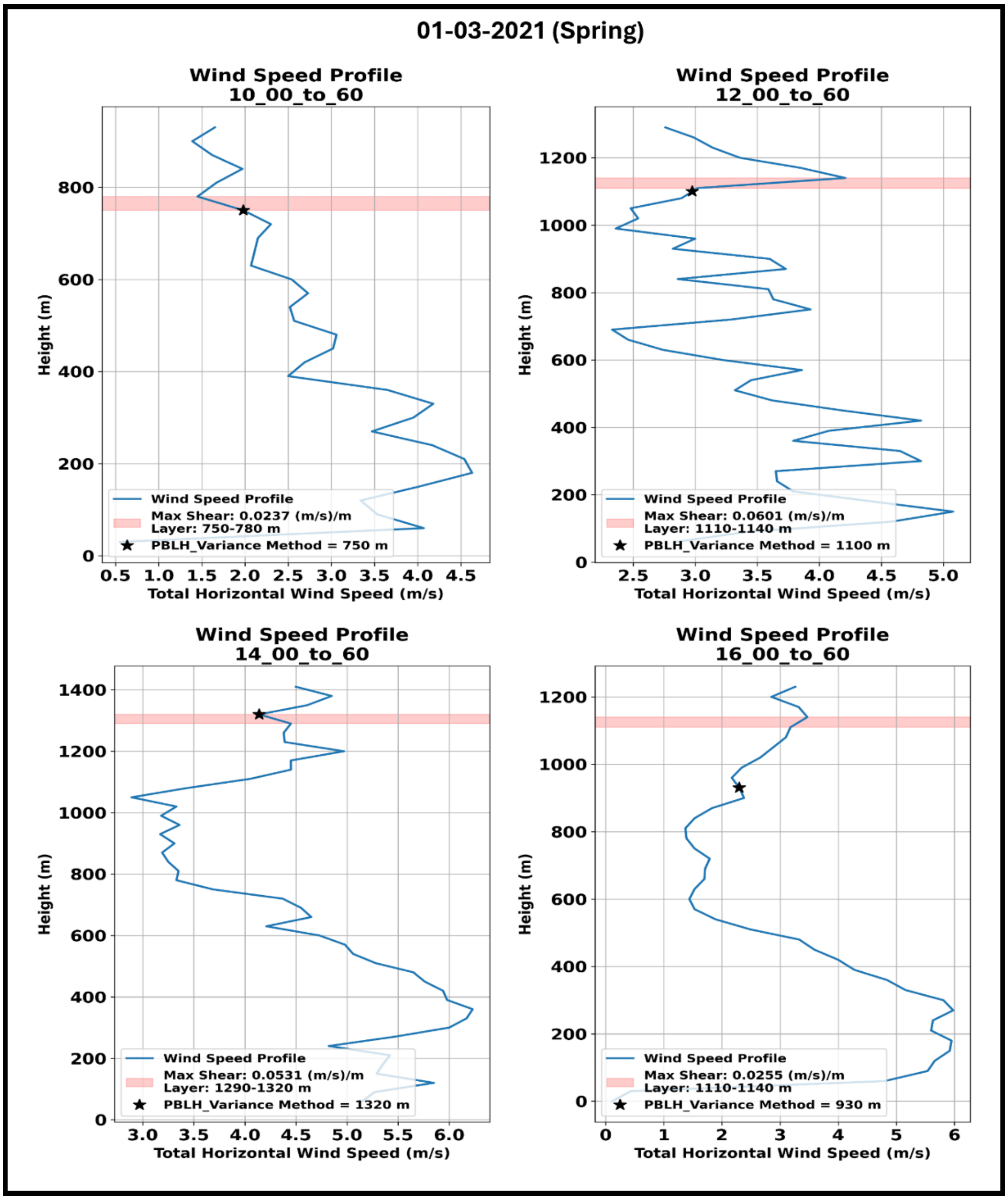

Figure 3.14. Wind shear profile for four convective hours on 01-03-2021, showing the layers of maximum shear and corresponding PBLH.

PBL Study by Wind Rose Plots:

The DBS scan data were further used to analyse wind speed and wind direction at six different altitude layers ranging from 420 to 1470 m, and the results are shown in the Figure 3.15 as six wind rose plots. The wind speed at the lower levels (420-930 m) is quite less and lies in a range of 3 to 5 ms^{-1}, and winds mostly originated from the south to west direction. The lower wind speed near the surface is due to the impact of surface friction (drag), which reduces wind speed close to the ground (Stull, 1988, pp. 347-404). Furthermore, the reported wind speeds in the middle layer (960-1290 m) were moderate around ~ 5 m s^{-1}, with dominant west and northwest components. A considerable variation in the wind speed was observed for the highest layer (1320-1470 m), where the wind speed increased significantly to above 17 ms^{-1}. In this layer the maximum wind originated from the west and northwest direction.

This sudden increase in wind speed is compatible with the transition into the free troposphere, which is characterised by a limited impact of surface friction and a much lower aerosol concentration compared to the boundary layer. This rapid increase in the wind speed in the upper layer also supports the wind shear method observations, in which the maximum shear was reported in the upper altitude layers.

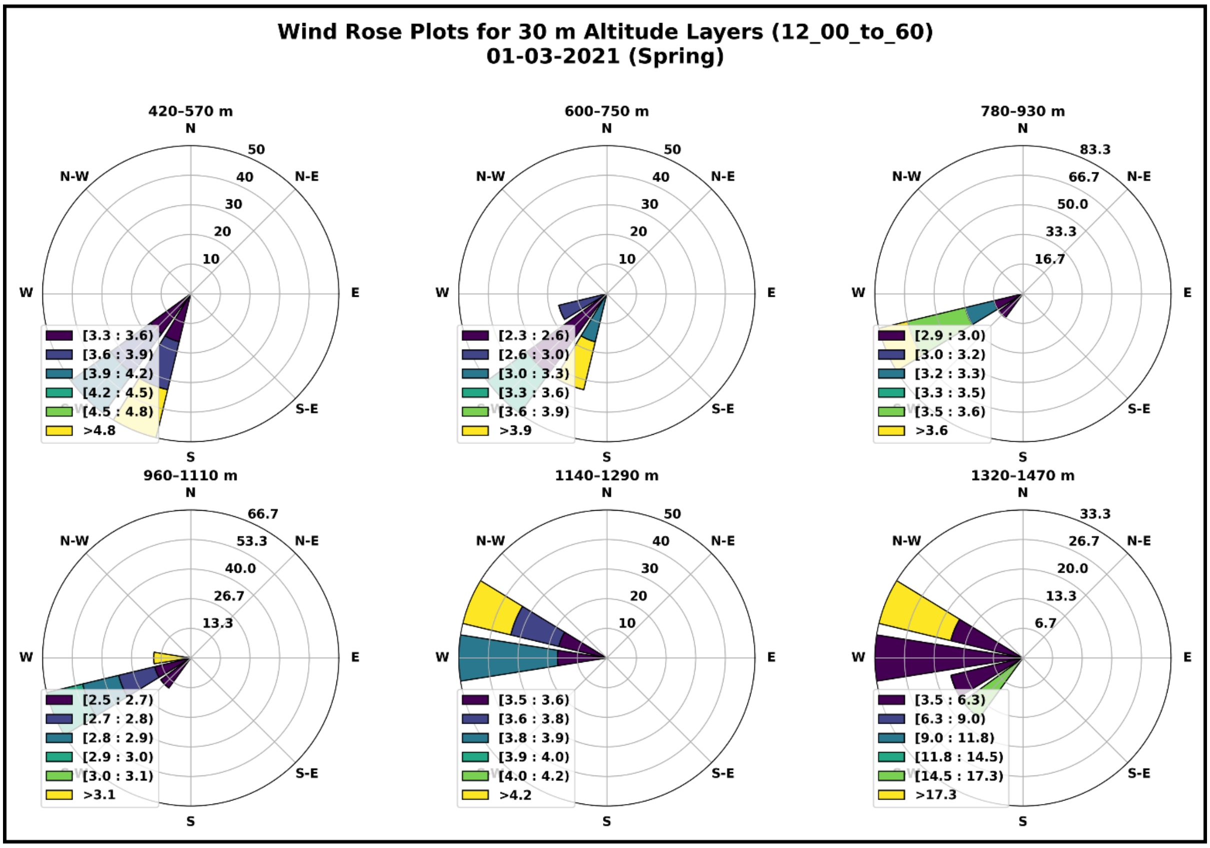

Figure 3.15. Wind rose plots for six altitude layers on 01-03-2021, illustrating wind speed and wind direction distribution.

Summary

In conclusion, the three retrieval frameworks applied in this chapter: the multi-wavelength aerosol-lidar gradient/WCT methods, ceilometer ERF-fit retrievals, and Doppler wind-lidar variance/shear approaches. Together, they provide an overall picture of the boundary-layer evolution at Potenza, while highlighting that the retrieved PBLH depends on which physical transition is being targeted. The aerosol-lidar methods retrieve PBLH from aerosol-structure gradients, and therefore their spread mainly reflects how each algorithm responds to multi-layer backscatter structure and to the finite thickness of the entrainment zone (with LGM/CRGM tending higher and IPM tending lower, while GM/WCT are typically intermediate). The ceilometer ERF-fit method retrieves PBLH as the midpoint of an idealised S-shaped transition in the backscatter profile. For the selected days, the hourly PBLH values follow the visible boundary between the mixed layer and the free troposphere, providing a complementary and comparatively stable estimate based on the profile shape. The Doppler wind-lidar methods diagnose the boundary layer from wind related features: the variance method tracks the height at which turbulence rapidly weakens, while the wind-shear method identifies the strongest shear layer near the capping region; these two wind-based indicators agree well during well-developed convection but can diverge during the evening transition when turbulence decays faster than shear above a residual layer. Overall, the different datasets show a similar daily cycle and similar seasonal changes, which supports the consistency of the main interpretation.

As continuous ceilometer measurements are available through the Cloudnet data portal, the ceilometer dataset was selected as the common observational basis for the inter-site comparison presented in Chapter 4. Specifically, Potenza is considered as a continental (land) site, while ACTRIS Lampedusa is used as a marine site. Since ceilometer observations are available for both stations in a consistent format, the next chapter focuses on a comparative analysis of the PBLH evolution over land and sea based on these datasets.

Chapter.4

PBLH Climatology and Land-Sea Comparison

In this chapter, the analysis focuses on ceilometer lidar observations from two ACTRIS stations, located in Potenza and in Lampedusa, to investigate the behaviour of the PBL over the continental and marine environments of the Mediterranean region. The objective is to compare the boundary layer structure over land and sea, with particular attention to how seasonal meteorology, Saharan dust intrusions, and cloud coverage influence the retrieved PBLH. The selected sites provide complementary conditions: Potenza represents a continental, inland environment affected by complex topography, while Lampedusa provide a marine setting characterised by strong air-sea interaction and frequent long-range transport of North African dust. By analysing full-year (2024) ceilometer data from both locations using the same retrieval methodology, this chapter aims at highlighting the main similarities and differences in PBL evolution at the two stations. A short description of the two ACTRIS sites is provided in the following section.

For the analysis of the PBLH over land, the ACTRIS Potenza station was selected. This site, already described in detail in Chapter 3, is the historical CNR hotspot for atmospheric studies. It is located in southern Italy, (40.60° N, 15.72° E) at an altitude of approximately 760 m above sea level (asl). The ceilometer lidar CL51 operated at this station, along with its technical specifications, has also been presented in Chapter 3.

4.1 Description of the ACTRIS Lampedusa Station

For the analysis of the PBLH in a marine environment, the ACTRIS Lampedusa station was selected. This facility is located on a coastal plateau on the small island of Lampedusa in the central Mediterranean Sea (around 35.5° N, 12.6° E), approximately 100 km from the Tunisian coast roughly at 45 m above sea level. The Station for Climate Observations is operated by ENEA (the Italian National Agency for New Technologies, Energy and Sustainable Economic Development). The site is characterized by very low local aerosol sources and is therefore well suited for monitoring marine background aerosol and Saharan dust transport over the central Mediterranean **(Marconi et al., 2014)**.

The station is equipped with a Lufft CHM 15k lidar ceilometer, a single-wavelength elastic backscatter system based on an eye-safe laser operating at 1064 nm. This instrument provides backscatter profiles from near the surface up to about 15 km, with a typical vertical resolution of 15 m and a temporal resolution of about 15 s, allowing continuous detection of cloud base height, aerosol layers, and boundary layer structure. The CHM 15k at Lampedusa is particularly suitable for long-term monitoring of the marine boundary layer height and for assessing the impact of Saharan dust intrusions and clouds on PBLH over this marine ACTRIS site. The map of Lampedusa and a photo of the ceilometer lidar are shown in Figure 4.1.

Figure 4.1. Map of Lampedusa Island (left) and image of the CHM 15k lidar ceilometer installed at the ENEA Station for climate observation (right) **(ENEA, n.d.)**.

4.2 PBLH Retrieval Strategy for Potenza and Lampedusa

For the analysis of the ceilometer lidar dataset, the ERF-fit method was applied, as described in detail in Chapter 3. The ceilometer measurements for the full year 2024 were obtained from the Cloudnet data portal for the ACTRIS Potenza and ACTRIS Lampedusa stations, respectively. The Cloudnet product used in this study provides hourly averaged attenuated backscatter profiles, which were processed following the implementation steps of the ERF-fit algorithm already outlined in Chapter 3. In this work, the retrieval was performed at a fixed time (12:00 UTC) for each day in order to analyse the midday evolution of the PBLH and to ensure consistency between the two stations. All PBLH values reported in this chapter are expressed as height above sea level (a.s.l.).

The analysis was carried out in two stages. In the first stage, the ERF-fit method was applied to the 12:00 UTC profile for every day of each month in 2024, allowing the monthly behaviour of the PBLH to be assessed for both the continental (Potenza) and marine (Lampedusa) environments. In the second stage, two representative months (January and August) were selected to investigate more specifically the influence of cloud cover and Saharan dust intrusions on the retrieved PBLH values. January was chosen because it is typically characterised by frequent cloud occurrence over both sites, while August is among the month's most affected by dust transport from North Africa. For each of these months, days affected by clouds were identified using cloud-cover information from EUMETSAT **(EUMETSAT, n.d.)**, and days affected by dust were identified using the DREAM8 and multi-model forecasts **(WMO Barcelona Dust Regional Centre, n.d.)**. After identifying cloudy and dusty days, these days were removed and the monthly average PBLH values were recalculated to evaluate the differences between the full dataset and the filtered dataset (clear-sky and dust-free conditions). The results for the Potenza and Lampedusa stations, together with the corresponding figures, are presented in the following sections.

4.3 Analysis of Potenza Station Data

For the ACTRIS Potenza station, a total of 356 days of ceilometer measurements were available for the year 2024 from the Cloudnet data portal. For each day, the ERF-fit algorithm was applied to the hourly attenuated backscatter profile corresponding to 12:00 UTC to retrieve the midday PBLH. The monthly PBLH evolution was derived by combining daily PBLH values for each month; this process was repeated for all months of the year (January-December). From the resulting monthly datasets, the mean and standard deviation were calculated to obtain a representative average PBLH for each month. These monthly averages were then used to construct the annual PBLH trend and its associated uncertainty. Consequently, the results presented in this section include the full annual distribution of average PBLH values for Potenza, along with the corresponding monthly uncertainties.

Furthermore, to investigate more specifically the influence of clouds and Saharan dust intrusions on the retrieved PBLH, two months (January and August) were selected for detailed analysis. The following sections present the results for Potenza, including the day-to-day variation of PBLH for all days in these two months, as well as the PBLH variation for clear-sky days after removing cloudy and dust-affected days.

4.3.1 Annual PBLH Cycle at Potenza

Figure 4.2 illustrates the monthly average PBLH values during the complete year 2024. All the average PBLH values, along with their respective standard deviations, are plotted against the corresponding months shown on the x-axis. It is observed that the PBLH values are lower during the winter months and increase progressively in the following months, reaching their maximum during summer. After the summer period, the PBLH starts to decrease again, returning to lower values toward December.

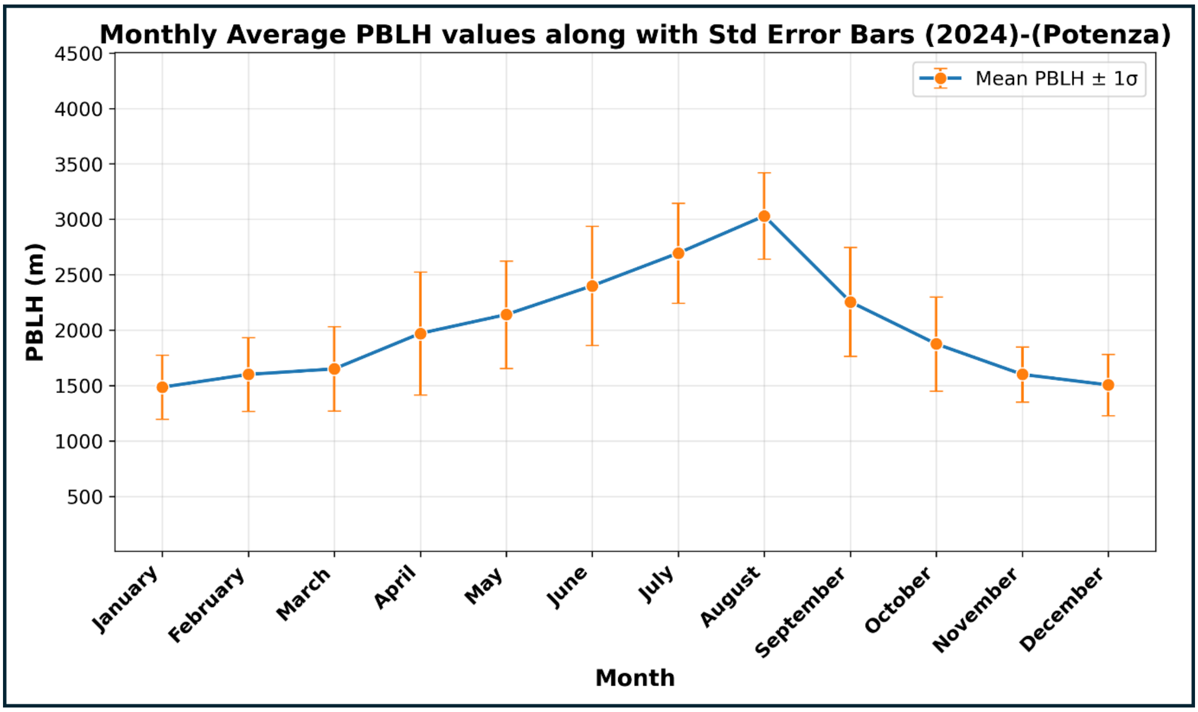

Figure 4.2. Monthly average PBLH for the ACTRIS Potenza station in 2024.

From the plot, it is evident that the Potenza station exhibits a distinct seasonal change in PBLH. During the winter months (December, January and February), the PBLH remains consistently low because solar insolation in winter is weak (shorter days and lower sun elevation), that limits the surface energy input and leads toward weaker surface heating and more stable stratification. The buoyant turbulence under these conditions is limited and the boundary layer remains shallow **(Stull, 1988, pp. 1-28)**. This seasonal behaviour is also reported in the literature **(Pal & Haeffelin, 2015)**.

During spring (March-May), the PBLH begins its seasonal increase. This is driven by stronger solar insolation, longer daylight time and more effective surface warming that promote more active buoyant mixing and a deeper convective mixed layer compared with winter, so the PBLH become higher, as also reported in the literature **(Pal & Haeffelin, 2015)**. The trend culminates in summer months (June to August), when these effects become even stronger. The highest PBLH of the year appears in August. The main reason is the strong solar radiation during summer, which heats the surface and supports stronger convective development, leading to the deepest boundary layer of the year, as also reported in the literature **(Pal & Haeffelin, 2015)**

After summer, in the autumn months (September, October and November), the PBLH begins to decrease again because surface heating weakens and the convective growth of the mixed layer becomes less pronounced. Consequently, the growth of the boundary layer becomes shallower towards late autumn and early winter. Overall, the monthly trend of PBLH over the complete year 2024 follows the expected seasonal behaviour, and the variation observed in the PBLH values is consistent with these seasonal changes.

4.3.2 Influence of Clouds and Saharan Dust on PBLH (Potenza)

After analysing the complete monthly PBLH values for Potenza, which include both clear days and the days affected by clouds in January and desert dust in August, an additional comparison was carried out to see how these conditions influence the PBLH during the selected months (January and August). The comparison helps to better understand the effect of clouds and dust intrusion on the PBLH at the Potenza station.

Figure 4.3 shows the daily PBLH values at 12:00 UTC for both months. In plot (A), the daily PBLH values for all days in January are shown by the blue line, and the monthly average value with its standard deviation, i.e. (1485 ± 285) m, is marked by the red point and error bar. Plot (B) presents only the clear-sky days of January, shown as blue points, together with their average PBLH value and standard deviation, i.e. (1630 ± 245) m, again marked by the red point.

In a similar way, plot (C) shows all days in August, including the dusty days, where the blue line connects the daily PBLH values. The monthly average PBLH value and standard deviation for all days in August, i.e. (3035 ± 395) m, are shown by the red point and error bar. Plot (D) represents only the clear-sky days of August, shown as blue points, together with their average PBLH value and standard deviation, i.e. (3235 ± 260) m, shown by the red marker.

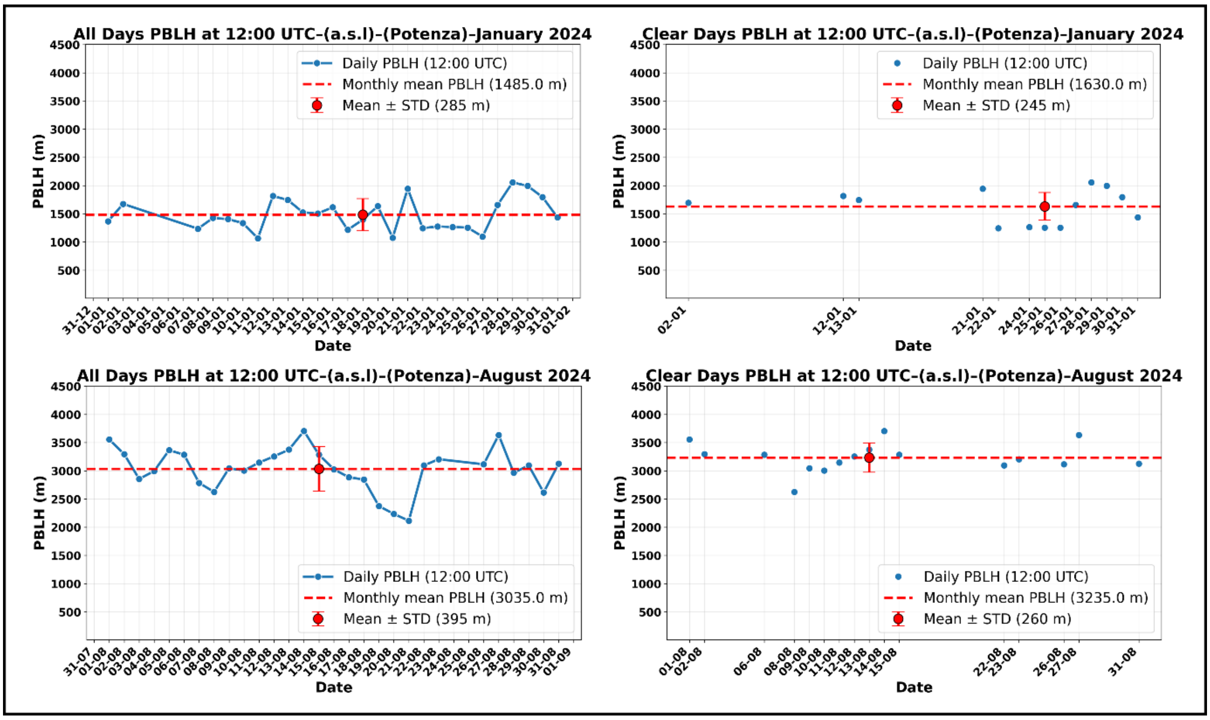

Figure 4.3. Daily PBLH at 12:00 UTC for Potenza during January and August 2024, Showing all days and clear-sky days.

To summarise these differences more clearly, Figure 4.4 provides an overall comparison. In plot (A), the monthly average PBLH values for all days of 2024 are shown together with the averages obtained after removing cloudy and dusty days. Plot (B) and (C) show a direct comparison between clear-sky and non-clear-sky conditions for January and August individually. In these plots, the orange markers represent the clear-sky days, while the black markers show the cloudy or dusty days. Even if the data seems to be consistent within errors, which is expected, the comparisons clearly illustrate how the cloud cover in January and dust intrusion in August can influence the PBLH relative to clear-sky conditions.

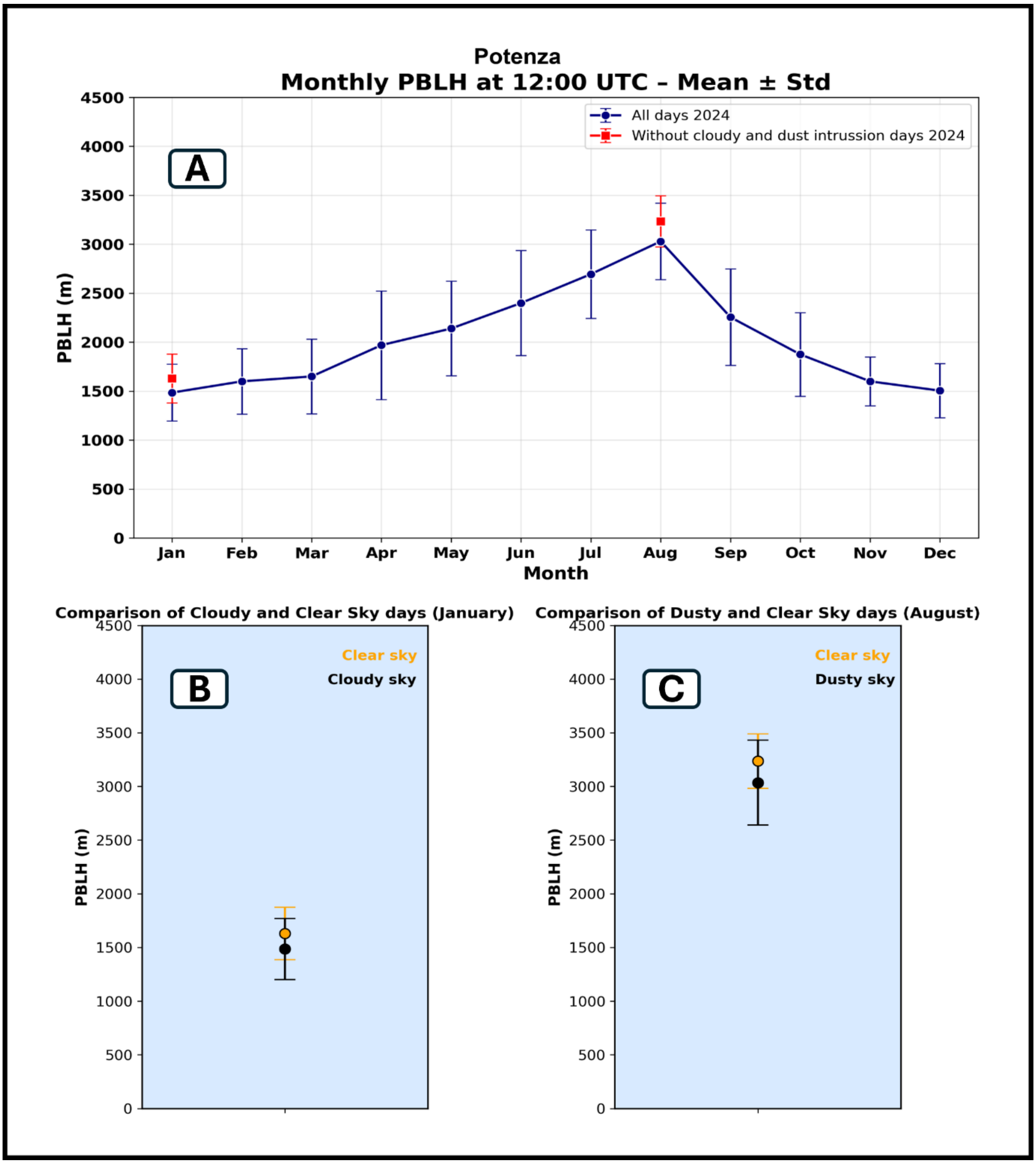

Figure 4.4. Comparison of clear-sky and cloudy/dusty PBLH conditions at Potenza for January and August 2024.

Overall, these plots clearly represent that the average PBLH is higher during clear-sky conditions as compared to the cloudy or desert dust sky conditions. This difference occurs possibly due to the atmospheric conditions that were present during these days. When clouds are present in January, the incoming solar insolation is reduced. Less sunlight reaches the surface because part of the radiation is absorbed or reflected by the clouds. As a result, the surface does not warm enough to generate strong convection, and the growth of the PBL is limited. This effect is consistent with previous work showing that cloud shadow reduces the solar (short-wave) input at the surface and therefore weakens the surface heat flux and buoyancy that drive convective mixing **(Schumann et al., 2002)**. This is why the PBLH values during cloudy days in January are lower. On the clear days of January, even though the solar insolation is not very strong during winter, the absence of clouds allows more sunlight to reach the surface, which helps in producing more convective mixing than on cloudy days.

During August, when Saharan dust intrusions are expected to frequently affect the Potenza area, a similar effect is observed. The presence of dust in the atmosphere can suppress the daytime PBL development. This is possibly because dust particles reduce the amount of solar radiation reaching the surface and also warm the air above, while the surface cools slightly. These conditions are favourable in reducing the vertical temperature gradient and suppress turbulent mixing, which limits the growth of the PBL. This mechanism is consistent with results reported for the Potenza site, where Saharan dust episodes were associated with a reduction of solar radiation reaching the surface (dimming) together with absorption within the dust layer (heating aloft) **(De Rosa et al., 2025)**, which can modify stability and limit vertical mixing. Conversely, during clear-sky days in August, more solar radiation reaches the surface, that leads to stronger surface heating and more active turbulent mixing. This allows the PBL to grow deeper, that explains why the PBLH values for clear-sky days are higher compared to dusty days.

4.4 Analysis of Lampedusa Station Data

In this section, the same analysis performed for the Potenza station is applied to the ACTRIS Lampedusa site. A total of 355 days of ceilometer data were available for the year 2024, and the daily PBLH values at 12:00 UTC were used to examine the monthly and annual behaviour of the boundary layer over Mediterranean marine location. As before, the months of January and August were examined separately to check how cloudy days and Saharan dust intrusions affect the PBLH at Lampedusa. The results presented here include the daily variations, the monthly averages, and the comparison between all-day conditions and clear-sky days for these two months.

4.4.1 Annual PBLH Cycle at Lampedusa

Figure 4.5 shows how the monthly average PBLH changes during the year 2024 at the Lampedusa station. On the x-axis the months are shown, and for each month the average PBLH with its standard deviation is plotted. In the first months of the year, the average PBLH over Lampedusa shows a clear decrease. From January to May, the boundary layer becomes gradually shallower, reaching its lowest levels in late spring. From June, the trend changes and the average PBLH starts to increase, reaching its maximum in mid-summer (around July). After the summer peak, the PBLH decreases again toward the end of summer and early autumn. Furthermore, from October to December, the PBLH increases again, showing higher values by the end of the year. So, over the whole year, the Lampedusa station shows periods where the average PBLH goes down and then up again, following the changes in the local seasonal conditions above the sea.

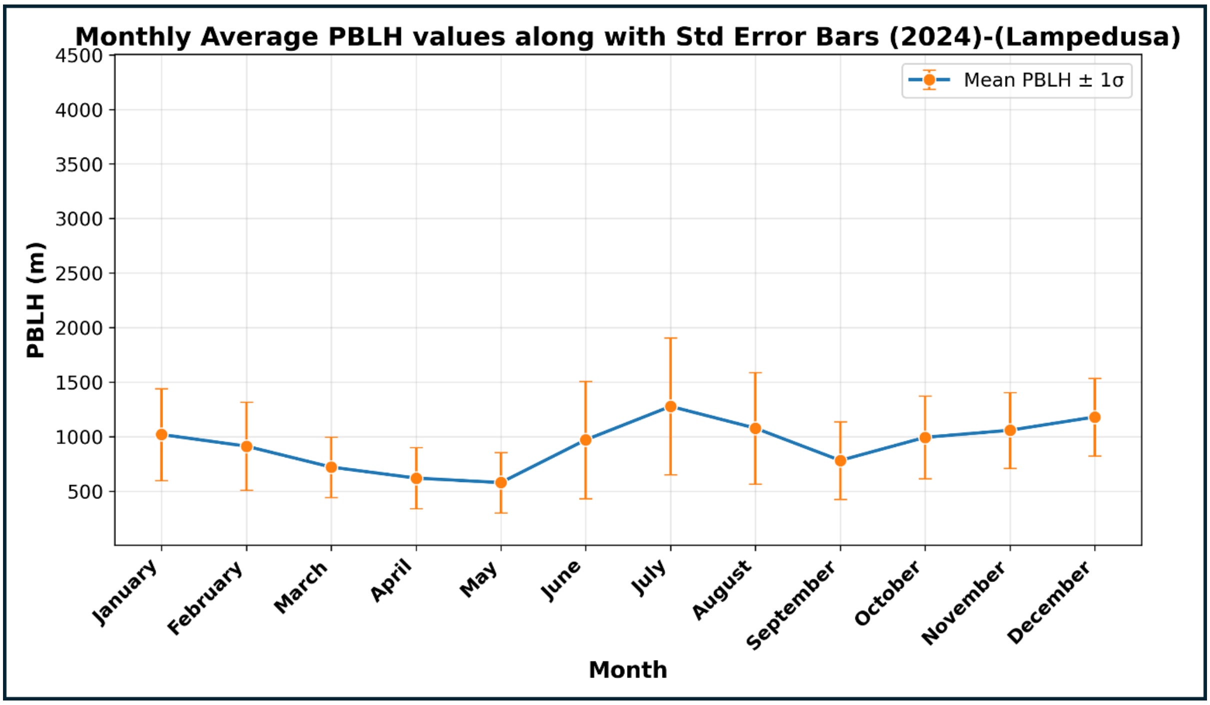

Figure 4.5. Monthly average PBLH for the ACTRIS Lampedusa station in 2024.

These results clearly evidence that PBLH values in Lampedusa are higher in the winter months (December, January and February) compared to the spring (March, April, May) and autumn (September, October, November). The PBLH during summer (June, July, August) is comparable to, or slightly higher than, the winter values. The possible reason behind this annual behaviour of the PBL at Lampedusa is that, over the sea the turbulence and depth of PBLH are governed by exchanges of momentum (surface drag), heat and moisture (evaporation) across the air-sea interface (Stull, 1988, pp. 251-294). Because sea-surface temperature typically varies weakly on the diurnal cycle, the near-surface thermal forcing over ocean often changes slowly, and variations in boundary-layer depth are frequently linked to air-mass advection and large-scale vertical motion rather than strong daytime heating as over land (Stull, 1988, pp. 1-28).

In the winter season, the growth of the PBL is possibly related to the dominant winter weather regimes over the Mediterranean. At Lampedusa, winter months show a much lower cloud-free frequency, indicating a stronger influence of cloudiness in winter (Trisolino et al., 2018). In addition, under cold-air outbreak conditions over the sea, stronger winds can enhance mechanical turbulence. In these situations, wind-driven mixing together with surface heat loss from the relatively warm sea can generate a deep, well-mixed marine boundary layer, as described in previous marine observations (Brilouet et al., 2017).

During the months of spring, (March-May), the monthly PBLH progressively decreases, with minimum values of around 578 m reached in May. The possible reason behind this behaviour is that during this transition season the sea surface begins to warm slowly compared to the winter period, while synoptic advection of continental air masses can increase the temperature of the overlying air, thereby reducing the temperature difference between the surface and the air above (Stull, 1988, pp. 587-618). With a smaller temperature gradient, warm air near the surface rises less strongly, resulting in weaker upward mixing, which limits the growth of the mixed layer and helps keep the marine boundary layer relatively shallow when surface forcing is weak (Stull, 1988, pp. 441-498).

In summer (June-August), the PBLH increases again and becomes comparable to, or slightly higher than, the winter values, with a maximum of about 1282 m in July. Stronger solar radiation enhances daytime heating of the surface and, even over the sea, supports the development of a convective mixed layer during the central hours of the day.

In autumn, the PBLH shows a decreasing trend in September, followed by increasing values in October and November. September still behaves as an extension of late summer, with sunlight-driven turbulence but with lower intensity, leading to modest PBLH values around 800 m. As the season progresses towards winter, enhanced wind speeds and sea-surface heat loss favour deeper mixing, as described in previous marine observations (Brilouet et al., 2017), resulting in PBLH values of about 1190 m in December.

4.4.2 Influence of Clouds and Saharan Dust on PBLH (Lampedusa)

After looking at the monthly PBLH behaviour at Lampedusa, the next step was to check more carefully how clouds and Saharan dust can change the PBLH during two selected months, January and August. For this purpose, the daily PBLH values at 12:00 UTC were separated into “all days” (including cloudy or dusty days) and “clear-sky days”, and the averages for each group were compared.

Figure 4.6 shows the daily PBLH values for these two months. In plot (A), the blue line connects the daily PBLH values for all days in January, and the red point with the error bar gives the monthly mean and standard deviation for all days, which is (1026 ± 422) m. Plot (B) shows only the clear-sky days of January as blue points. For these days, the red marker and error bar give an average PBLH of (760 ± 233) m.

In a similar way, plot (C) shows all days in August, including the dusty days, where the blue line connects the daily PBLH values. The monthly average and standard deviation for all days in August are (1077 ± 512) m, shown by the red point and error bar. Plot (D) presents only the clear-sky days of August as blue points, together with their average PBLH value and standard deviation, (1115 ± 495) m, again marked by the red symbol.

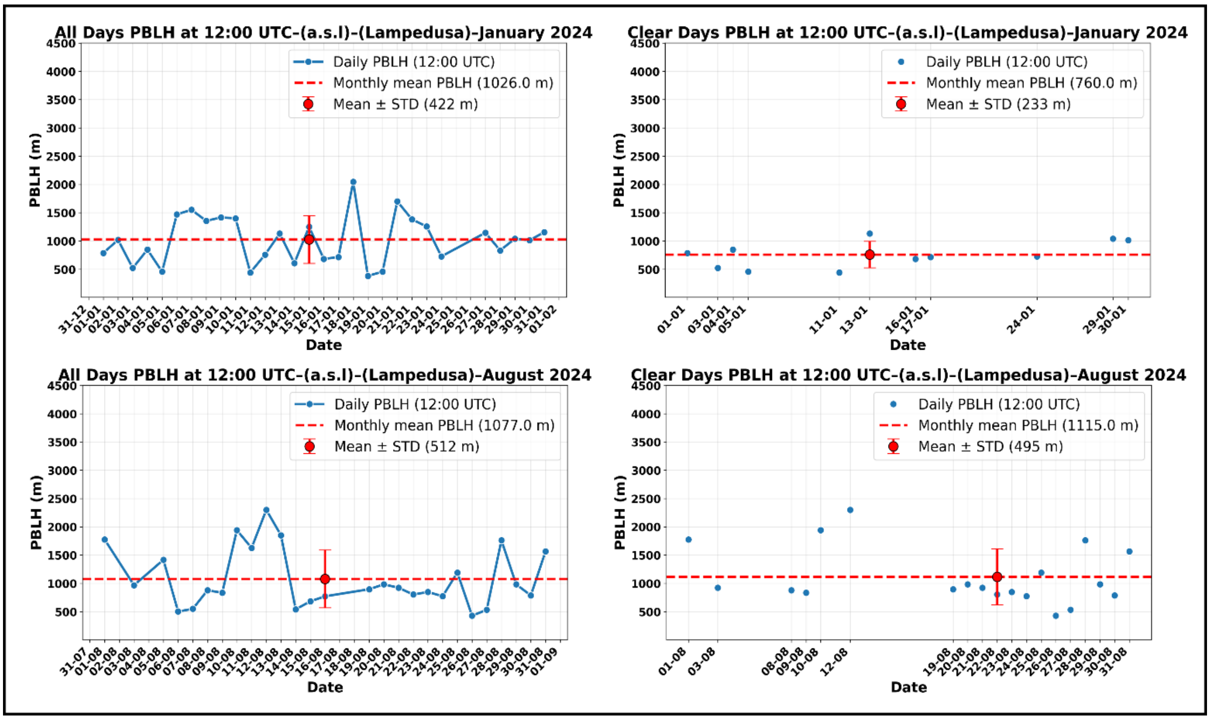

Figure 4.6. Daily PBLH at 12:00 UTC for Lampedusa during January and August 2024, Showing all days and clear-sky days.

Figure 4.7 summarises these results. In plot (A), the blue curve shows the monthly average PBLH for all days of 2024, while the red markers indicate the averages obtained after removing cloudy and dusty days. Plots (B) and (C) focus only on January and August. In these two panels, the orange symbols represent the mean PBLH for clear-sky days, and the black symbols represent the mean PBLH for cloudy (January) or desert dust (August) conditions. In this way, Figure 4.7 provides a simple visual comparison between all-day and clear-sky PBLH values for the two selected months at Lampedusa.

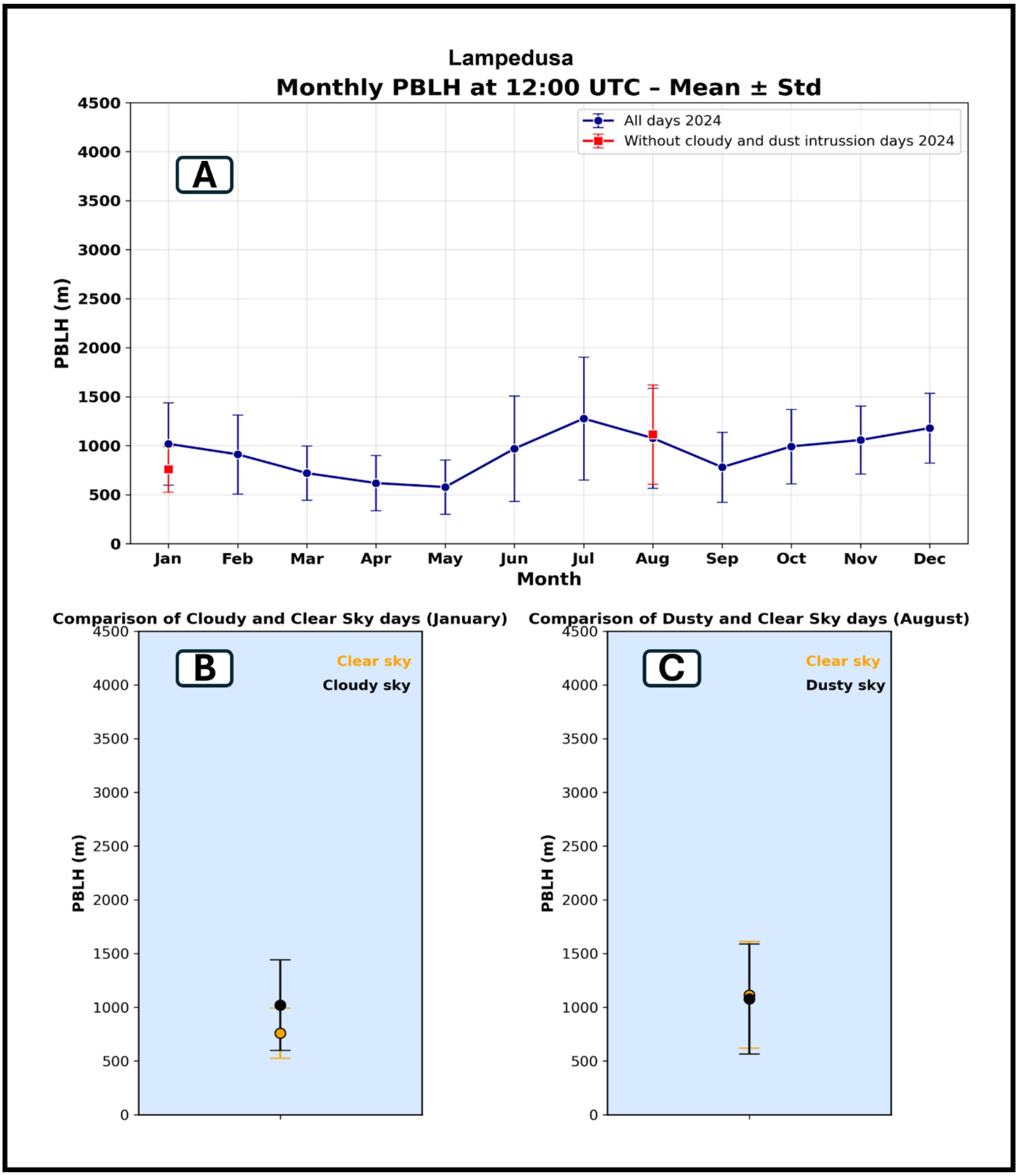

Figure 4.7. Comparison of clear-sky and cloudy/dusty PBLH conditions at Lampedusa for January and August 2024.

The comparison between "all days" and "clear-sky days" in January shows that cloudy situations are associated, on average, with a deeper boundary layer. For the full January data set, the mean PBLH is about 1026 m, whereas on clear-sky days it is reduced to roughly 760 m. This behaviour is possibly due to the dominant winter weather regimes over the Mediterranean. As discussed earlier, at Lampedusa, winter months have a much lower cloud-free frequency, indicating a stronger influence of cloudiness in winter **(Trisolino et al., 2018)**. Under cold-air outbreak conditions over the sea, stronger winds can enhance mechanical turbulence. In these situations, wind-driven mixing together with surface heat loss from the relatively warm sea can generate a deep, well-mixed marine boundary layer, as described in previous marine observations **(Brilouet et al., 2017),** which can reach heights near or above 1000 m.

In contrast, clear-sky winter days are typically associated with weaker winds. Under these calm and more stable situations, the limited solar heating at midday is possibly not sufficient to increase the boundary layer height effectively, and the boundary layer remains shallower.

For August, the situation is different. The mean PBLH for all days (1077 m) is very close to the mean for clear-sky days only (1115 m), which indicates that, at least around 12:00 UTC, the presence of Saharan dust does not significantly deepen or suppress the mixed layer at Lampedusa. This is possibly because Lampedusa is located very close to sea level, and in summer Saharan dust is often transported in elevated layers that can pass above the marine boundary layer without being efficiently mixed down to the surface. In these cases, the dust mainly remains decoupled from the near-surface marine layer **(Marconi et al., 2014)**, so the local boundary-layer structure retrieved from the ceilometer can remain similar on dusty and dust-free days.

4.5 Comparison of Continental and Marine Boundary Layer Characteristics

Figure 4.8 illustrates a sea-level comparison between the monthly average PBLH values for the Potenza station (blue line), which belongs to a continental (land) boundary layer, and the Lampedusa station (red line), which belongs to the marine boundary layer.

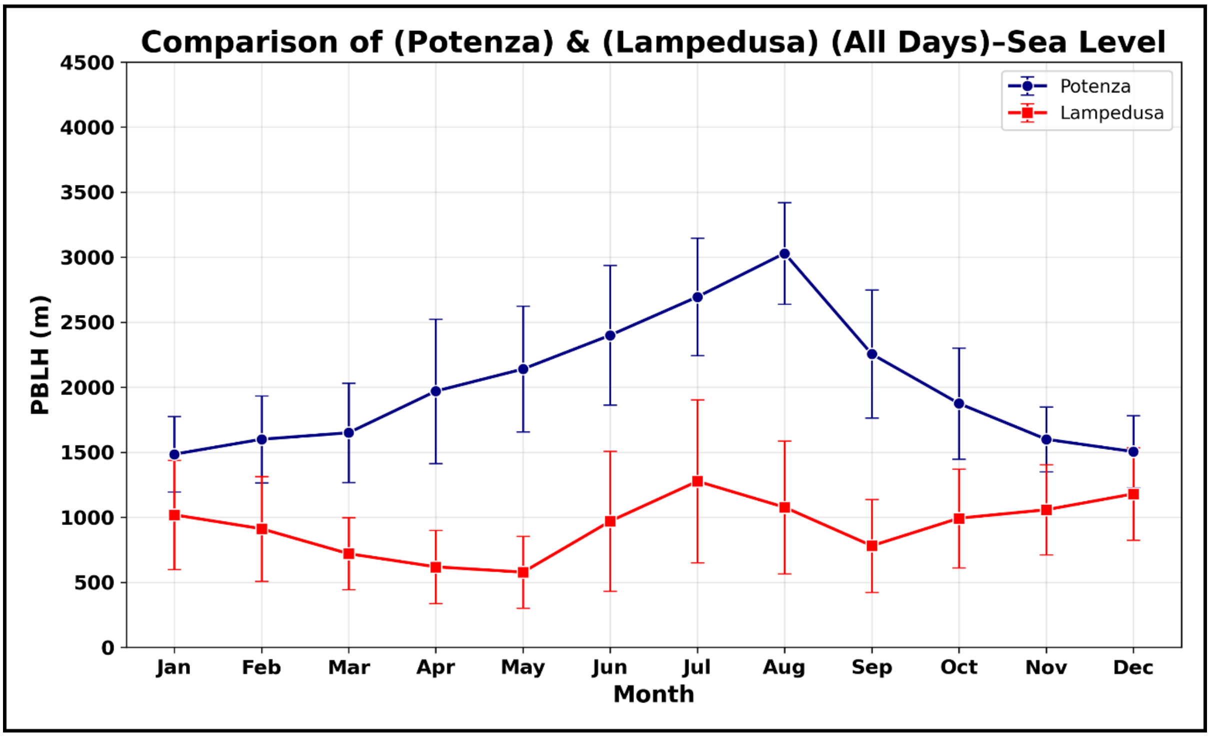

Figure 4.8. Monthly average PBLH at 12:00 UTC for the ACTRIS Potenza (continental land site) and Lampedusa (marine site) stations for the year 2024.

It is observed that the minimum value of PBLH at the Lampedusa station occurs in spring, with values of about (578 m a.s.l), whereas the maximum PBLH at Lampedusa is found in summer, reaching about (1282 m a.s.l). Similarly, at the Potenza station the minimum PBLH is reported in winter, around (1485 m a.s.l), while the maximum value is observed in summer, reaching about (3035 m a.s.l).

From the comparison, it is clear that in Potenza there is a marked seasonal variation in boundary-layer height, with lower PBLH during the cold seasons and higher PBLH during the warm seasons. In contrast, Lampedusa does not show such a pronounced seasonal cycle in PBLH as Potenza. This behaviour is consistent with the different response of land and sea surfaces to surface energy input. Over land, the surface temperature can rise quickly during the day, which increases the sensible heat flux and supports stronger near-surface heating of the atmosphere. Over the sea, a larger fraction of the available energy is often used for evaporation (latent heat flux), and the sea-surface temperature changes much more slowly because of the large effective heat capacity (thermal inertia). This leads to a more buffered and gradually varying surface forcing over the marine environment (Stull, 1988, pp. 251-294).

Other factors that can contribute to the different boundary-layer behaviour over land and sea are related to local air circulations and surface characteristics. The Potenza site is located on a plain surrounded by low mountains, whereas Lampedusa is a small, flat island in the central Mediterranean Sea and is characterized by a marine environment. Therefore, the differences observed between the boundary layer over Potenza and Lampedusa are likely linked to land-sea contrasts. Over land, boundary-layer turbulence is strongly influenced by the diurnal cycle and by spatial variability in surface properties such as roughness and vegetation, while in complex terrain slope and valley flows can further modify boundary-layer structure and mixing. In contrast, over the open ocean the boundary layer can, under certain conditions, remain relatively shallow, often only a few hundred metres deep **(Garratt, 1994)**.

Furthermore, from the analysis of the effect of cloud shading during winter (January), when comparing the two sites it is observed that clouds tend to suppress boundary-layer development over land at Potenza, whereas at Lampedusa cloudy situations are often associated with a deeper marine boundary layer. The possible reason for this difference is that, at Potenza, the presence of clouds reduces the incoming solar radiation at the surface, so the ground warms less and buoyancy-driven convection is weaker, as discussed in the literature **(Schumann et al., 2002)**. As a result, the growth of the boundary layer is limited and the PBLH remains lower. However, at Lampedusa the January statistics indicate that the mean PBLH is higher when cloudy days are included than when only clear-sky days are considered, which is consistent with the stronger influence of cloudiness in winter at this site **(Trisolino et al., 2018)**. In these cases, cloudiness can coincide with winter marine regimes such as cold-air outbreaks, where stronger winds enhance mechanical turbulence and, together with surface heat loss from the relatively warm sea, favour a deeper and well-mixed marine boundary layer, as described in previous marine observations **(Brilouet et al., 2017)**.

Finally, from the analysis of the effect of Saharan dust intrusions during summer (August), it is observed that dust has a weaker impact on the boundary-layer height at Lampedusa than at Potenza. At Lampedusa, the mean PBLH for all days is very close to the mean for clear-sky days, which suggests that, around 12:00 UTC, dust does not markedly deepen or suppress the mixed layer. A reasonable explanation is that in summer Saharan dust is often transported in elevated layers that pass above the marine boundary layer, so the dust can remain largely decoupled from the near-surface marine air mass **(Marconi et al., 2014)**, and the retrieved boundary-layer structure remains similar on dusty and dust-free days. In contrast, over Potenza the August analysis indicates a clearer suppression of daytime PBL development during dusty conditions. This behaviour is consistent with the radiative effect of dust, which can reduce the solar radiation reaching the surface while absorbing radiation within the dust layer and warming the air aloft (De Rosa et al., 2025); together, these effects can modify stability, weaken turbulent mixing, and limit boundary-layer growth.

Summary

In conclusion, this chapter uses the full year (2024) of ceilometer retrievals at 12:00 UTC to describe the annual evolution of the PBLH at the continental Potenza site and the marine Lampedusa site, and to assess how clouds and Saharan dust can modify the retrieved PBLH under selected conditions. At Potenza, the monthly means show a clear seasonal cycle, with the lowest PBLH in winter, a progressive increase through spring, and maximum values in summer, followed by a decline in autumn, consistent with the expected strengthening and weakening of surface-driven convection through the year. The focused analysis of January and August further indicates that non-clear-sky conditions tend to reduce the midday PBLH relative to clear-sky days. At Lampedusa, the annual cycle is different and does not follow the same winter-to-summer increase as Potenza, reflecting the different surface forcing over the sea; in particular, winter months can exhibit relatively deep mixing under winter marine weather regimes, while late-spring conditions show the shallowest monthly means. The January-August comparisons also highlight a site-dependent response: at Lampedusa, cloudy winter situations are associated, on average, with a deeper marine boundary layer than clear-sky days, whereas Saharan dust in August produces only small differences between all-day and clear-sky days. Overall, the direct comparison between the two stations confirms a stronger seasonal modulation over land than over sea and shows that clouds and dust can affect midday PBLH in different ways at the two sites.

Conclusion

PBL dynamics strongly control the vertical mixing of heat, moisture, aerosols, and pollutants, and the PBLH is therefore a key parameter for interpreting both local atmospheric processes and air-quality conditions. However, the retrieval of PBLH from backscatter-based remote sensing remains challenging, particularly when the transition to the free troposphere is weak, when residual or elevated layers are present, or when clouds and dust modify the aerosol and turbulence structure that is used as a tracer in many methods.

In this thesis, the seasonal and diurnal variability of PBLH was investigated using active remote sensing observations within the ACTRIS framework, with the main multi-instrument analysis carried out at the Potenza station where aerosol lidar, ceilometer, and wind Doppler lidar measurements are available. A complementary land-sea comparison was then performed using ceilometer observations at Potenza and Lampedusa to examine how boundary-layer development differs between continental and marine environments under different seasonal conditions.

The multi-wavelength aerosol-lidar analysis at Potenza provided a consistent seasonal picture across 355, 532, and 1064 nm. The diurnal cycle shows the deepest daytime development in summer, intermediate growth in spring, a reduced amplitude in autumn, and the shallowest and most stable conditions in winter. Since PBLH is an atmospheric property, variations across wavelengths or algorithms mainly reflect how clearly the mixed-layer top is expressed in the lidar signal. A small wavelength dependence is observed because the particle-to-molecular contrast varies with wavelength: the 1064 nm channel can yield slightly higher retrieved PBLH than 532 and 355 nm, whereas 355 nm can produce slightly lower retrieved PBLH, consistent with the stronger molecular contribution at shorter wavelengths and the resulting reduction in particle-to-molecular contrast. For routine monitoring, 532 nm represents a balanced choice because it usually provides a clear mixed-layer-top gradient while being less affected by molecular background than 355 nm. The 1064 nm channel is preferable when sharp aerosol gradients are present, but it may also be more sensitive to aerosol-layer structure, increasing the spread when residual or elevated layers are present. The 355 nm channel remains useful as a complementary cross-check when short-wavelength aerosol sensitivity is desired. When comparing retrieval techniques, LGM and CRGM most often produce the highest PBLH estimates, IPM tends to give the lowest values, and GM and WCT are typically intermediate; under stratified conditions, the spread between methods increases because different algorithms can respond to different features within the same profile.

For the wind Doppler lidar at Potenza, a representative early spring day was analysed using two approaches: the vertical-velocity variance method from vertical-stare measurements and the wind-shear method from DBS scans. The variance-based retrieval captures the expected diurnal evolution, with a shallow boundary layer before sunrise, rapid growth after sunrise, and a daytime maximum around early afternoon, followed by a decline toward the evening hours. During the peak convective period (10:00-14:00 UTC), the windshear and variance methods provide consistent PBLH estimates, while differences become more evident in the late afternoon transition (around 16:00 UTC), when turbulence weakens but shear aloft can remain pronounced. Wind-speed and wind-direction profiles (shown through wind-rose analyses) further support this interpretation by indicating a marked increase of wind speed at higher layers, consistent with a transition from the well mixed boundary layer toward the free troposphere.

Using ceilometer observations as a common basis for inter-site comparison, the land-sea analysis highlighted a clear contrast between Potenza and Lampedusa. Potenza shows a pronounced seasonal cycle with strong daytime growth during the warm season and low winter values, consistent with the stronger control of the surface energy balance over land. In comparison, Lampedusa exhibits a weaker seasonal amplitude and a different annual pattern. This behaviour is consistent with marine boundary layers often being shallow and capped by stable inversions, with typical depths on the order of a few hundred metres.

The January and August case analyses indicate that the factors controlling the midday PBLH differ between the two environments: at Potenza, cloudy winter days and dusty summer days are associated with lower PBLH than clear-sky conditions, whereas at Lampedusa winter cloudiness can coincide with a deeper mixed layer and summer dust has a weaker impact on the PBLH estimated from the ceilometer, consistent with dust often occurring in elevated layers that remain decoupled from the marine boundary layer.

Overall, this work shows that using a consistent analysis framework across different active remote sensing datasets, based on systematic data screening (clouds and dust), analysis in a consistent temporal context (diurnal and seasonal cycles), interpretation using the same physical reasoning (mixing, stratification, and residual layers), and comparison across seasons and environments, provides a reliable description of how PBLH varies with season and between environments. At the same time, it shows that inter-method differences become more evident when the atmosphere contains multiple layers (e.g., residual or elevated aerosol/pollution layers).

The algorithms and processing steps used in this thesis work provide a clear and reproducible basis to extend the analysis to longer time periods and to additional ACTRIS sites. However, the analysis in Chapter 4 also has some limitations: the annual comparison is based on a single year (2024) and on a fixed retrieval time at 12:00 UTC, so it reflects midday PBLH and not the complete diurnal cycle. In addition, the analysis of the effects of clouds and Saharan dust is restricted to January and August, rather than covering the full seasonal statistics, and the screening process can affect the separation between clear-sky and dusty/cloudy-sky days, which can influence the comparison between them. The interpretation can also be strengthened by using independent information, such as radiosonde profiles, cloud products (e.g., cloud base height / cloud mask), and model output. Extending the dataset to multiple years and increasing the number of analysed days would also allow more robust statistics, and comparisons could be made by excluding dust-affected periods (and other strong aerosol events). Future work should focus on improving the screening and the selection of the relevant layer in complex cases (e.g., residual layers, elevated aerosol layers, and cloud-driven transitions), where different methods may correctly identify different features within the same evolving boundary layer.

List of References:

ACTRIS ERIC. (n.d.). Aerosol, Clouds and Trace Gases Research Infrastructure (ACTRIS). Retrieved December 25, 2025, from https://www.actris.eu

Adam, M. (2012). Notes on Rayleigh scattering in lidar signals. Appl. Opt. 51, 2135. https://doi.org/10.1364/AO.51.002135

ALICEnet. (n.d.). Automated Lidar-Ceilometer network. Retrieved December 25, 2025, from https://www.alice-net.eu

Ansmann, A., & Müller, D. (2005). Lidar and atmospheric aerosol particles. In C. Weitkamp (Ed.), Lidar: Range-resolved optical remote sensing of the atmosphere (pp. 105-138). Springer-Verlag, New York. https://doi.org/10.1007/0-387-25101-4_4

Ansmann, A., Riebesell, M., Wandinger, U., Weitkamp, C., Voss, E., Lahmann, W., and Michaelis, W. (1992b). Combined Raman elastic-backscatter lidar for vertical profiling of moisture, aerosol extinction, backscatter, and lidar ratio. Applied Physics B: Photo physics and Laser Chemistry, 55(1), 18-28. https://doi.org/10.1007/BF00348608

Barlow, J. F., Dunbar, T. M., Nemitz, E. G., Wood, C. R., Gallagher, M. W., Davies, F., ... & Harrison, R. M. (2011). Boundary layer dynamics over London, UK, as observed using Doppler lidar during REPARTEE-II. Atmospheric Chemistry and Physics, 11(5), 2111-2125. https://doi.org/10.5194/acp-11-2111-2011

Bellini, A., Diémoz, H., Di Liberto, L., Gobbi, G. P., Bracci, A., Pasqualini, F., & Barnaba, F. (2024). ALICENET - An Italian network of automated lidar ceilometers for four-dimensional aerosol monitoring: Infrastructure, data processing, and applications. Atmospheric Measurement Techniques, 17, 6119-6144. https://doi.org/10.5194/amt-17-6119-2024

Boselli, A., Armenante, M., D'Avino, L., D'Isidoro, M., Pisani, G., Spinelli, N., & Wang, X. (2009). Atmospheric aerosol characterization over Naples during 2000-2003 EARLINET project: Planetary boundary-layer evolution and layering. Boundary-Layer Meteorology, 132(1), 151-165. https://doi.org/10.1007/s10546-009-9382-6

Boucher, O. (2015). Atmospheric aerosols: Properties and climate impacts. Springer. https://doi.org/10.1007/978-94-017-9649-1

Brilouet, P.-E., Durand, P., & Canut, G. (2017). The marine atmospheric boundary layer under strong wind conditions: Organized turbulence structure and flux estimates by airborne measurements. Journal of Geophysical Research: Atmospheres, 122(4), 2115-2130. https://doi.org/10.1002/2016JD025960

Brooks, I. M. (2003). Finding boundary layer top: Application of a wavelet covariance transform to lidar backscatter profiles. Journal of Atmospheric and Oceanic Technology, 20(8), 1092-1105. https://doi.org/10.1175/1520-0426(2003)020%3C1092:FBLTAO%3E2.0.CO;2

Campbell, J. R., Hlavka, D. L., Welton, E. J., Flynn, C. J., Turner, D. D., Spinhirne, J. D., ... & Hwang, I. H. (2002). Full-time, eye-safe cloud and aerosol lidar observation at atmospheric radiation measurement program sites: Instruments and data processing. Journal of Atmospheric and Oceanic Technology, 19(4), 431-442. https://doi.org/10.1175/1520-0426(2002)019<0431:FTESCA>2.0.CO;2

Cherukuru, N. W., Calhoun, R., Krishnamurthy, R., Benny, S., Reuder, J., & Flügge, M. (2017). 2D VAR single Doppler lidar vector retrieval and its application in offshore wind energy. Energy Procedia, 137, 497-504. https://doi.org/10.1016/j.egypro.2017.10.378

Chowdhury, S., et al. (2019). Tracking ambient $PM_{2.5}$ build-up in Delhi National Capital Region during the dry season over 15 years using a high-resolution (1 km) satellite aerosol dataset. Atmospheric Environment, 204, 142-150. https://doi.org/10.1016/j.atmosenv.2019.02.029

CIAO - CNR-IMAA Atmospheric Observatory. (2024). Atmospheric observatory instruments. National Research Council of Italy - Institute of Methodologies for Environmental Analysis (CNR-IMAA). Retrieved from https://ciao.imaa.cnr.it/

Cimorelli, A. J., Perry, S. G., Venkatram, A., Weil, J. C., Paine, R. J., Wilson, R. B., Lee, R. F., Peters, W. D., & Brode, R. W. (2005). AERMOD: A dispersion model for industrial source applications. Part I: General model formulation and boundary layer characterization. Journal of Applied Meteorology, 44(5), 682-693. https://doi.org/10.1175/JAM2227.1

Clifton, A., Boquet, M., Burin Des Roziers, E., Westerhellweg, A., Hofsass, M., Klaas, T., ... & Aitken, M. (2015). Remote sensing of complex flows by Doppler wind lidar: Issues and preliminary recommendations (No. NREL/TP-5000-64634). National Renewable Energy Lab. (NREL), Golden, CO (United States). https://doi.org/10.2172/1351595

Cloudnet. (n.d.). Cloudnet - European cloud profiling network. Retrieved December 25, 2025, from https://cloudnet.fmi.fi

Cuesta, J., Marsham, J. H., Parker, D. J., & Flamant, C. (2009). Dynamical mechanisms controlling the vertical redistribution of dust and the thermodynamic structure of the west Saharan atmospheric boundary layer during summer. Atmospheric Science Letters, 10(1), 34-42. https://doi.org/10.1002/asl.207

Dai, C., Wang, Q., Kalogiros, J. A., Lenschow, D. H., Gao, Z., & Zhou, M. (2014). Determining boundary-layer height from aircraft measurements. Boundary-Layer Meteorology, 152(2), 277-302. https://doi.org/10.1007/s10546-014-9929-z

Dang, R., Yang, Y., Hu, X. M., Wang, Z., & Zhang, S. (2019). A review of techniques for diagnosing the atmospheric boundary layer height (ABLH) using aerosol lidar data. Remote Sensing, 11(13), 1590. https://doi.org/10.3390/rs11131590

De Rosa, B., Mytilinaios, M., Amodeo, A., Colangelo, C., D'Amico, G., Dema, C., … & Mona, L. (2025). Observations of Saharan dust intrusions over Potenza, Southern Italy, during 13 years of lidar measurements: Seasonal variability of optical properties and radiative impact. Remote Sensing, 17(3), 453. https://doi.org/10.3390/rs17030453

D'Amico, G., Amodeo, A., Baars, H., Binietoglou, I., Freudenthaler, V., Mattis, I., Wandinger, U., & Pappalardo, G. (2015). EARLINET Single Calculus Chain - overview on methodology and strategy. Atmospheric Measurement Techniques, 8, 4891-4916. https://doi.org/10.5194/amt-8-4891-2015

D'Amico, G., Amodeo, A., Baars, H., Freudenthaler, V., Mattis, I., Mona, L., Pappalardo, G., Rocadenbosch, F., Sicard, M., Wiegner, M., & Zehner, C. (2016). EARLINET Single Calculus Chain-technical-Part 1: Pre-processing of raw lidar data. Atmospheric Measurement Techniques, 9, 491-507. https://doi.org/10.5194/amt-9-491-2016

de Arruda Moreira, G., Guerrero-Rascado, J. L., Bravo-Aranda, J. A., Benavent-Oltra, J. A., Ortiz-Amezcua, P., Róman, R., & Alados-Arboledas, L. (2018). Study of the planetary boundary layer by microwave radiometer, elastic lidar and Doppler lidar estimations in Southern Iberian Peninsula. Atmospheric Research, 213, 185-195. https://doi.org/10.1016/j.atmosres.2018.06.007

EARLINET. (n.d.). European Aerosol Research Lidar Network. Retrieved December 25, 2025, from https://www.earlinet.org

ENEA. (2025). ENEA Lampedusa Climate Observatory. ACTRIS Italia. https://actris.it

ENEA. Lampedusa: ENEA Station for Climate Observations. Italian National Agency for New Technologies, Energy and Sustainable Economic Development. https://www.lampedusa.enea.it

European Organisation for the Exploitation of Meteorological Satellites. (n.d.). EUMETView product viewer. Retrieved December 18, 2025, from https://view.eumetsat.int/productviewer

Fernald, F. G. (1984). Analysis of atmospheric lidar observations: some comments. Applied optics, 23(5), 652-653. https://doi.org/10.1364/AO.23.000652

Gao, J., Droegemeier, K. K., Gong, J., & Xu, Q. (2004). A method for retrieving mean horizontal wind profiles from single-Doppler radar observations contaminated by aliasing. Monthly Weather Review, 132(6), 1399-1409. https://journals.ametsoc.org/view/journals/mwre/132/6/1520-0493-132.6.1399.xml?utm

Garratt, J. R. (1994). Review: The atmospheric boundary layer. Earth-Science Reviews, 37(1-2), 89-134. https://doi.org/10.1016/0012-8252(94)90026-4

Hayden, K. L., Anlauf, K. G., Hoff, R. M., Strapp, J. W., Bottenheim, J. W., Wiebe, H. A., ... & McKendry, I. G. (1997). The vertical chemical and meteorological structure of the boundary layer in the Lower Fraser Valley during Pacific'93. Atmospheric Environment, 31(14), 2089-2105. https://doi.org/10.1016/S1352-2310(96)00300-7

Hooper, W. P., & Eloranta, E. W. (1986). Lidar measurements of wind in the planetary boundary layer: the method, accuracy and results from joint measurements with radiosonde and kytoon. Journal of climate and applied meteorology, 990-1001. https://www.jstor.org/stable/26182473

Huang, M., Gao, Z., Miao, S., Chen, F., LeMone, M. A., Li, J., … Wang, L. (2017). Estimate of boundary-layer depth over Beijing, China, using Doppler lidar data during SURF-2015. Boundary-Layer Meteorology, 162(3), 503-522. https://doi.org/10.1007/s10546-016-0205-2

Häme, S., Kivekäs, N., Wagner, J., De Mazière, M., Nikolova, N., Sciare, J., Váňa, M., … Vaughan, G. (2023). ACTRIS IMP-Deliverable 1.1: Report on national ACTRIS consortia. Horizon 2020 Research and Innovation Framework Programme, Grant Agreement No. 871115. ACTRIS ERIC. Retrieved from https://www.actris.eu

ISO 2533-1975-"Standard atmosphere" (International Organisation for Standardization, Geneva, 1975).

Ji, X., Liu, C., Xie, Z., Hu, Q., Dong, Y., Fan, G., ... & Liu, J. (2019). Comparison of mixing layer height inversion algorithms using lidar and a pollution case study in Baoding, China. Journal of Environmental Sciences, 79, 81-90. https://doi.org/10.1016/j.jes.2018.11.003

Klett, J. D. (1981). Stable analytical inversion solution for processing lidar returns. Applied optics, 20(2), 211-220. https://doi.org/10.1364/AO.20.000211

Koscielny, A. J., Doviak, R. J., & Rabin, R. (1982). Statistical considerations in the estimation of divergence from single-Doppler radar and application to prestorm boundary-layer observations. Journal of Applied Meteorology, 21(2), 197-210. https://doi.org/10.1175/1520-0450(1982)021<0197:SCITEO>2.0.CO;2

Kovalev, V. A., & Eichinger, W. E. (2004). Elastic lidar: Theory, practice, and analysis methods. John Wiley & Sons. https://doi.org/10.1002/0471643173

Lapenna, E., Buono, A., Mauceri, A., Zaccardo, I., Cardellicchio, F., D'Amico, F., … Mona, L. (2025). ICOS Potenza (Italy) atmospheric station: A new spot for the observation of greenhouse gases in the Mediterranean basin. Atmosphere, 16(1), 57. https://doi.org/10.3390/atmos16010057

Lau, K. M., Kim, M. K., & Kim, K. M. (2006). Asian summer monsoon anomalies induced by aerosol direct forcing: The role of the Tibetan Plateau. Climate Dynamics, 26(7), 855-864. https://doi.org/10.1007/s00382-006-0114-z

Lenschow, D. H. (1970). Airplane measurements of planetary boundary layer structure. Journal of Applied Meteorology, 9, 874-884. https://doi.org/10.1175/1520-0450(1970)009<0874:AMOPBL>2.0.CO;2

Li, H., Liu, B., Ma, X., Jin, S., Ma, Y., Zhao, Y., & Gong, W. (2021). Evaluation of retrieval methods for planetary boundary layer height based on radiosonde data. Atmospheric Measurement Techniques, 14(9), 5977-5986. https://doi.org/10.5194/amt-14-5977-2021

Li, H., Yang, Y., Hu, X.-M., Huang, Z., Wang, G., Zhang, B., & Zhang, T. (2017). Evaluation of retrieval methods of daytime convective boundary layer height based on lidar data. Journal of Geophysical Research, 1-16. https://doi.org/10.1002/2016JD025620

Li, Z., Guo, J., Ding, A., Liao, H., Liu, J., Sun, Y., … Zhu, B. (2017). Aerosol and boundary-layer interactions and impact on air quality. National Science Review, 4(6), 810-833. https://doi.org/10.1093/nsr/nwx117

Lindelöw, P. (2008). Fiber-based coherent lidars for remote wind sensing (Doctoral dissertation, Technical University of Denmark, Department of Electrical Engineering). Technical University of Denmark. https://backend.orbit.dtu.dk/ws/portalfiles/portal/4957725/Thesis%20final%20A4.pdf

Lindelöw-Marsden, P. (2009). UpWind D1. Uncertainties in wind assessment with LIDAR (Technical Report, Risø-R-1681(EN)). Roskilde, Denmark: Technical University of Denmark. https://www.osti.gov/etdeweb/biblio/989917

Liu, Z., Barlow, J. F., Chan, P.-W., Fung, J. C. H., Li, Y., Ren, C., Mak, H. W. L., & Ng, E. (2019). A review of progress and applications of pulsed Doppler wind lidars. Remote Sensing, 11(21), 2522. https://doi.org/10.3390/rs11212522

Madonna, F., Amodeo, A., Boselli, A., Cornacchia, C., Cuomo, V., D'Amico, G., Giunta, A., Mona, L., & Pappalardo, G. (2011). CIAO: The CNR-IMAA advanced observatory for atmospheric research. Atmospheric Measurement Techniques, 4, 1191-1210. https://doi.org/10.5194/amt-4-1191-2011

Mallat, S., & Hwang, W. L. (2002). Singularity detection and processing with wavelets. IEEE transactions on information theory, 38(2), 617-643. 10.1109/18.119727

Mallet, M. D., d'Anna, B., Même, A., Bove, M. C., Cassola, F., Pace, G., … Formenti, P. (2019). Summertime surface PM_1 aerosol composition and size by source region at the Lampedusa island in the central Mediterranean Sea. Atmospheric Chemistry and Physics, 19(17), 11123-11142. https://doi.org/10.5194/acp-19-11123-2019

Marconi, M., Sferlazzo, D. M., Becagli, S., Bommarito, C., Calzolai, G., Chiari, M., di Sarra, A., Ghedini, C., Gómez-Amo, J. L., Lucarelli, F., Meloni, D., Monteleone, F., Nava, S., Pace, G., Piacentino, S., Rugi, F., Severi, M., Traversi, R., & Udisti, R. (2014). Saharan dust aerosol over the central Mediterranean Sea: PM10 chemical composition and concentration versus optical columnar measurements. Atmospheric Chemistry and Physics, 14, 2039-2054. https://doi.org/10.5194/acp-14-2039-2014

Martucci, G., Matthey, R., Mitev, V., & Richner, H. (2007). Comparison between backscatter lidar and radiosonde measurements of the diurnal and nocturnal stratification in the lower troposphere. Journal of Atmospheric and Oceanic Technology, 24(7), 1231-1244. https://doi.org/10.1175/JTECH2036.1

McCormick, M. P. (2005). Airborne and spaceborne lidar. In C. Weitkamp (Ed.), Lidar: Range-resolved optical remote sensing of the atmosphere (pp. 355-391). Springer-Verlag, New York. https://link.springer.com/chapter/10.1007/0-387-25101-4_13

Menut, L., Flamant, C., Pelon, J., & Flamant, P. H. (1999). Urban boundary-layer height determination from lidar measurements over the Paris area. Applied Optics, 38(6), 945-954. https://doi.org/10.1364/AO.38.000945

Münkel, C., Eresmaa, N., Räsänen, J., & Karppinen, A. (2007). Retrieval of mixing height and dust concentration with lidar ceilometer. Boundary-layer meteorology, 124(1), 117-128. https://doi.org/10.1007/s10546-006-9103-3

O'Connor, E. J., Illingworth, A. J., & Hogan, R. J. (2004). A technique for autocalibration of cloud lidar. Journal of Atmospheric and Oceanic Technology, 21(5), 777-786. https://doi.org/10.1175/1520-0426(2004)021<0777:ATFAOC>2.0.CO;2

Ortiz-Amezcua, P., Martínez-Herrera, A., Manninen, A. J., Pentikäinen, P. P., O'Connor, E. J., Guerrero-Rascado, J. L., & Alados-Arboledas, L. (2022). Wind and turbulence statistics in the urban boundary layer over a mountain-valley system in Granada, Spain. Remote Sensing, 14(10), 2321. https://doi.org/10.3390/rs14102321

O'Connor, E. J., Illingworth, A. J., Brooks, I. M., Westbrook, C. D., Hogan, R. J., Davies, F., & Brooks, B. J. (2010). A method for estimating the turbulent kinetic energy dissipation rate from a vertically pointing Doppler lidar, and independent evaluation from balloon-borne in situ measurements. Journal of atmospheric and oceanic technology, 27(10), 1652-1664. https://doi.org/10.1175/2010JTECHA1455.1

Pal, S., & Haeffelin, M. (2015). Forcing mechanisms governing diurnal, seasonal, and interannual variability in the boundary layer depths: Five years of continuous lidar observations over a suburban site near Paris. Journal of Geophysical Research: Atmospheres, 120(23), 11936-11956. https://doi.org/10.1002/2015JD023268

Pearson, G., Davies, F., & Collier, C. (2009). An analysis of the performance of the UFAM pulsed Doppler lidar for observing the boundary layer. Journal of Atmospheric and Oceanic Technology, 26(2), 240-250. https://doi.org/10.1175/2008JTECHA1128.1

Peris-Ferrús, C., Gómez-Amo, J. L., Marcos, C., Freile-Aranda, M. D., Utrillas, M. P., & Martínez-Lozano, J. A. (2017). Heating rate profiles and radiative forcing due to a dust storm in the Western Mediterranean using satellite observations. Atmospheric Environment, 160, 142-153. https://doi.org/10.1016/j.atmosenv.2017.04.023

Piccarreta, M., Capolongo, D., & Boenzi, F. (2004). Trend analysis of precipitation and drought in Basilicata from 1923 to 2000 within a Southern Italy context. International Journal of Climatology, 24(7), 907-922. https://doi.org/10.1002/joc.1038

Päschke, E., Leinweber, R., & Lehmann, V. (2015). An assessment of the performance of a 1.5 μm Doppler lidar for operational vertical wind profiling based on a 1-year trial. Atmospheric Measurement Techniques, 8(6), 2251-2266. https://doi.org/10.5194/amt-8-2251-2015

Sassen, K. (2005). Polarization in lidar. In C. Weitkamp (Ed.), Lidar: Range-resolved optical remote sensing of the atmosphere (pp. 19-40). Springer-Verlag, New York. https://doi.org/10.1007/0-387-25101-4_2

Seibert, P., Beyrich, F., Gryning, S.-E., Joffre, S., Rasmussen, A., & Tercier, P. (2000). Review and intercomparison of operational methods for the determination of the mixing height. Atmospheric Environment, 34(7), 1001-1027. https://doi.org/10.1016/S1352-2310(99)00349-0

Sathe, A., Mann, J., Vasiljevic, N., & Lea, G. (2015). A six-beam method to measure turbulence statistics using ground-based wind lidars. Atmospheric Measurement Techniques, 8(2), 729-740. https://doi.org/10.5194/amt-8-729-2015

Schumann, U., Dörnbrack, A., & Mayer, B. (2002). Cloud-shadow effects on the structure of the convective boundary layer. Meteorologische Zeitschrift, 11(4), 285-294. https://doi.org/10.1127/0941-2948/2002/0011-0285

Seinfeld, J. H., & Pandis, S. N. (1998). Atmospheric chemistry and physics: From air pollution to climate change. Wiley. https://books.google.it/books?hl=en&lr=&id=n_RmCgAAQBAJ&oi=fnd&pg=PR5&dq=seinfeld+and+pandis+atmospheric+physics&ots=gTLcGQrhhR&sig=MF9jAP4HVDJrxkY6nYIweIO8Vy4&redir_esc=y#v=onepage&q=seinfeld%20and%20pandis%20atmospheric%20physics&f=false

Singh, A., et al. (2023). Influence of stubble burning on air quality of Northern India: A case study of Indo-Gangetic plains of India. Environmental Monitoring and Assessment, 195(4), 487. https://doi.org/10.1007/s10661-023-11027-w

Steyn, D. G., Baldi, M., & Hoff, R. M. (1999). The detection of mixed layer depth and entrainment zone thickness from lidar backscatter profiles. Journal of Atmospheric and Oceanic Technology, 16(7), 953-959. https://doi.org/10.1175/1520-0426(1999)016<0953:TDOMLD>2.0.CO;2

Stull, R. B. (1988). An introduction to boundary layer meteorology. Kluwer Academic Publishers. https://doi.org/10.1007/978-94-009-3027-8

Thobois, L., Cariou, J. P., & Gultepe, I. (2019). Review of lidar-based applications for aviation weather. Pure and Applied Geophysics, 176, 1959-1976. https://doi.org/10.1007/s00024-018-2058-8

Trisolino, P., di Sarra, A., Anello, F., Bommarito, C., Di Iorio, T., Meloni, D., Monteleone, F., Pace, G., Piacentino, S., & Sferlazzo, D. (2018). A long-term time series of global and diffuse photosynthetically active radiation in the Mediterranean: interannual variability and cloud effects. Atmospheric Chemistry and Physics, 18, 7985-8000. https://doi.org/10.5194/acp-18-7985-2018

UCAR Center for Science Education. (n.d.). Layers of the atmosphere [Diagram]. University Corporation for Atmospheric Research. Retrieved December 23, 2025, from https://scied.ucar.edu/image/atmosphere-layers-diagram

Vivone, G., D'Amico, G., Summa, D., Lolli, S., Amodeo, A., Bortoli, D., & Pappalardo, G. (2021). Atmospheric boundary layer height estimation from aerosol lidar: A new approach based on morphological image processing techniques. Atmospheric Chemistry & Physics, 21, 4249-4265. https://doi.org/10.5194/acp-21-4249-2021

Wallace, J. M., & Hobbs, P. V. (2006). Atmospheric science: An introductory survey (2nd ed.). Elsevier Academic Press. https://doi.org/10.1016/C2009-0-00034-8

Wandinger, U. (2005). Introduction to lidar. In C. Weitkamp (Ed.), Lidar: Range-resolved optical remote sensing of the atmosphere (pp. 1-18). Springer. https://doi.org/10.1007/0-387-25101-4_1

Wandinger, U. (2005). Raman lidar. In C. Weitkamp (Ed.), Lidar: Range-resolved optical remote sensing of the atmosphere (pp. 241-267). Springer-Verlag, New York. https://doi.org/10.1007/0-387-25101-4_9

Wang, C., Xia, H., Liu, Y., Lin, S., & Dou, X. (2018). Spatial resolution enhancement of coherent Doppler wind lidar using joint time-frequency analysis. Optics Communications, 424, 48-53. https://doi.org/10.1016/j.optcom.2018.04.042

Wang, F., Yang, T., Wang, Z., Chen, X., Wang, H., & Guo, J. (2021). A comprehensive evaluation of planetary boundary layer height retrieval techniques using lidar data under different pollution scenarios. Atmospheric Research, 258, Article 105483. https://doi.org/10.1016/j.atmosres.2021.105483

Werner, C. (2005). Doppler wind lidar. In C. Weitkamp (Ed.), Lidar: Range-resolved optical remote sensing of the atmosphere (pp. 325-353). Springer-Verlag, New York. https://doi.org/10.1007/0-387-25101-4_12

Wiegner, M., Madonna, F., Binietoglou, I., Forkel, R., Gasteiger, J., Geiß, A., Pappalardo, G., Schäfer, K., & Thomas, W. (2014). What is the benefit of ceilometers for aerosol remote sensing? An answer from EARLINET. Atmospheric Measurement Techniques, 7, 1979-1997. https://doi.org/10.5194/amt-7-1979-2014

WMO Barcelona Dust Regional Center. (n.d.). Daily dust products. Retrieved December 18, 2025, from https://dust.aemet.es/products/daily-dust-products

Xu, Q., & Gong, J. (2003). Background error covariance functions for Doppler radial-wind analysis. Quarterly Journal of the Royal Meteorological Society, 129(593), 1709-1729. https://doi.org/10.1256/qj.02.129

Zangwill, A. (2012). Modern Electrodynamics [WWW Document]. Higher Education from Cambridge University Press. https://doi.org/10.1017/CBO9781139034777